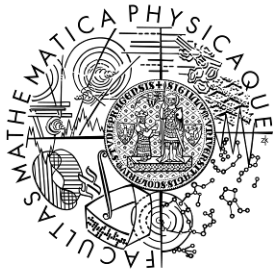

FACULTY
OF MATHEMATICS
AND PHYSICS
Charles University

DOCTORAL THESIS

RNDr. Jaroslav Valenta

Magnetism in non-centrosymmetric uranium compound: $UIrSi_3$

Department of Condensed Matter Physics

Supervisor of the doctoral thesis: RNDr. Jiří Prchal, Ph.D.

Study programme: Physics
Specialization: Physics of Condensed Matter and Materials Research

Prague 2019

I declare that I carried out this doctoral thesis independently, and only with the cited sources, literature and other professional sources.

I understand that my work relates to the rights and obligations under the Act No. 121/2000 Coll., the Copyright Act, as amended, in particular the fact that the Charles University has the right to conclude a license agreement on the use of this work as a school work pursuant to Section 60 paragraph 1 of the Copyright Act.

In Prague date 29.10.2019 RNDr. Jaroslav Valenta

This page I would like to dedicate for expression of my great thanks to all my colleagues, friends and family who supported me during my studies. First, of all I would like to thank a lot to my supervisor RNDr. Jiří Prchal, Ph.D. for his great support, spent time, answering of my frequent questions, help during unexpected situations, advices and guidance during not only Doctoral study but also whole my study at the Charles University (lat. Universitas Carolina). I would like to thank very much to prof. RNDr. Vladimír Sechovský, DrSc. who is consultant of my thesis for his research advices, discussions and guidance in study of not only uranium compounds. Here I would like to also thank to Dr. Fuminory Honda for teaching me with Bridgman type pressure cells and cooperation with investigation of uranium compounds. The theoretical part of this study was done by our theoretician doc. RNDr. Martin Diviš, CSc. and Dr. Leonid Sandratskii whom I would like to thank for supporting calculations in this thesis. I very appreciate valuable cooperation and discussions with my colleagues at Department of Condensed Matter Physics, RNDr. Michal Vališka, Ph.D., RNDr. Jan Prokleška, Ph.D., RNDr. Petr Doležal, RNDr. Marie Hrůzová Kratochvílová, Ph.D., RNDr. Klára Uhlířová, Ph.D., RNDr. Milan Klicpera, Ph.D., RNDr. Petr Čermák, Ph.D., RNDr. Silvie Černá, Ph.D., Ing. Barbora Vondráčková, RNDr. Petr Opletal, Mgr. Petr Proschek, Mgr. Kristina Vlášková, Bc. Jiří Volný and the head of the department prof. Pavel Javorský, Dr. I am very grateful for cooperation with Institute of Physics of the Czech Academy of Sciences where I would like to thank to RNDr. Jiří Kaštil, Ph.D., RNDr. Martin Míšek, Ph.D., and for very valuable discussions about high pressure techniques, I would like to thank to Ing. Jiří Kamarád, Csc. I would also like to express my gratitude for valuable discussions and critical comments with corrections of reading this thesis to Dr. Frank Roelof de Boer.

Since the study is like long journey where you found new things but also lost a lot of others. It is similar to life where during my study I lost my grandmother, granduncle, friend of my family Anna Šonová and others who supported me anytime.

Last but not least, I would like to thank very much my parents and sister who encouraged me and supported during my studies and without their support I can not imagine successful finalization of my study. Thank you!

Title: Magnetism in the non-centrosymmetric uranium compound: $UIrSi_3$

Author: RNDr. Jaroslav Valenta

Department: Department of Condensed Matter Physics

Supervisor of the doctoral thesis: RNDr. Jiří Prchal, Ph.D., DCMP

Abstract: The study presented in this thesis is focused on $UIrSi_3$ which is one of two known uranium compounds that crystallize in a non-centrosymmetric structure. This first study of $UIrSi_3$ in single-crystalline form confirms antiferromagnetic order below $T_N = 41.7$ K and reveals strong uniaxial anisotropy. The antiferromagnetic order is suppressed by application of a magnetic field along the *c* axis ($\mu_0 H_C = 7.3$ T at 2 K). In contrast, application of a magnetic field up to 14 T along the *a* axis gives paramagnetic response. The high T_N, contrasting with the low $\mu_0 H_C$, together with the opposite signs of the paramagnetic Curie temperatures of the *a*-axis and *c*-axis paramagnetic susceptibility indicate a competition between antiferromagnetic and ferromagnetic interactions. The first-order metamagnetic transition at H_C shows asymmetric hysteresis which reflects a complex antiferromagnetic ground state. With increasing temperature, the hysteresis becomes gradually smaller and vanishes at 28 K where the first-order transition changes to second-order transition which remains up to T_N. The point where the order of the transition changes is considered to be the tricritical point ($T_{tcp} = 28$ K, $\mu_0 H_{tcp} = 5.8$ T). As possible scenario to explain this change, it has been suggested that the first-order transition is a manifestation of antiferromagnetic ↔ paramagnetic state with polarized magnetic moments probably accompanied by a magnetic-field-induced Lifshitz transition. The second-order transition is a transition between the antiferromagnetic and the paramagnetic state. A pressure study reveals an opposite pressure evolution of T_N and H_C. The increasing of T_N and the decrease of H_C with increasing pressure suggests possible pressure-induced ferromagnetic order at high pressures. The compressibility along the *a* axis is found to be more than three times larger than along the *c* axis which, together with the opposite pressure evolution of T_N and H_C indicates that the magnetic properties are driven by magnetoelastic coupling. Neutron-diffraction experiments reveal a propagation vector (0.1, 0.1, 0) which changes upon application of a magnetic field and, above $\mu_0 H_C$, disappearance of the antiferromagnetic order is observed.

Keywords: non-centrosymmetric structure, anisotropy, tricritical point, pressure, antiferromagnetism

Contents

1. Introduction

Materials adopting a non-centrosymmetric crystal structure are in the field of interest mainly because the absence of a center of inversion symmetry gives rise to several interesting properties. For instance the absence of a center of inversion in the crystal structure implies the creation of a Rashba-type antisymmetric spin-orbit coupling [1, 2]. This spin-orbit coupling is considered as a condition for possible appearance of unconventional superconductivity [3] and also causes spin splitting of the Fermi surface which affects the magnetism [4]. The literature provides examples of compounds crystallizing in the non-centrosymmetric $BaNiSn_3$-type of structure, like several RTX_3 compounds (where R is a rare-earth element, T a transition metal and X a *p*-electron element). The RTX_3 compounds with Ce exhibit highly interesting phenomena like pressure-induced superconductivity near a quantum critical point, high-field superconductivity, vibron states, coexistence of antiferromagnetism and superconductivity, etc [5-11]. The magnetism of rare-earth compounds is based on localized magnetic moments of the 4f-electrons.

The 5f-electrons of the actinides, of which U and its compounds are most frequently studied, give rise to a different type of magnetism. The magnetic moment of U is not well localized as for rare-earth atoms and depends on the U-U spacing. U-based compounds usually possess huge magnetocrystalline anisotropy which originates from the position in the crystal structure of nearest-neighbor U atoms carrying a 5f-electron moment. The surrounding of the U atom determines the magnetic coupling like direct exchange interaction in case of direct overlap of 5f-wave functions of U atoms or indirect exchange interaction in case of an involved ligand atom positioned between nearest U atoms. The unique properties of U compounds include phenomena like tricriticality, coexistence of superconductivity and ferromagnetism, high-field superconductivity, quantum criticality, etc… [12-16].

Only two U compounds are reported to crystallize in the non-centrosymmetric $BaNiSn_3$-type of crystal structure, namely $UIrSi_3$ and $UNiGa_3$. Studies of $UIrSi_3$ and $UNiGa_3$ in polycrystalline form showed these compounds to be antiferromagnetic with similar ordering temperatures of 42 K and 39 K, respectively [17, 18].

The absence of reported results on single crystals of these compounds has been the motivation of our study. A single crystal of $UIrSi_3$ has been selected as a subject for the thesis. The thesis reports results of a profound characterization of the single crystal with particular emphasis on the strong uniaxial anisotropy of this antiferromagnet. A proper insight in the physics of $UIrSi_3$ was obtained by studying the electric resistivity, magnetization, Hall resistivity, heat capacity, Seebeck effect and dilatometry, as a function of temperature and magnetic field. Furthermore, pressure measurements under hydrostatic and uniaxial pressure were performed. Finally, in order to get information on the magnetic structure, neutron-diffraction experiments have been carried out.

The thesis is divided into five parts. The first part provides a brief introduction and reveals the main motivation of the study. The second part concerns the basic theory of magnetism of 4f- and 5f-electron systems. The third part describes the experimental techniques used in the study. The main part of the thesis is concentrated in the fourth part in which the experimental results are presented and discussed. The conclusions are presented in the fifth part.

2. General theory

2.1. Magnetism and magnetic interactions

The physical unit describing the magnetism on microscopic scale is magnetic moment $\boldsymbol{\mu}$ which can be in classical case defined as current I passing around closed oriented loop of area $|\mathbf{d}\boldsymbol{S}|$ [19, 20]:

$$\mathbf{d}\boldsymbol{\mu} = I \cdot \mathbf{d}\boldsymbol{S}. \tag{2.1}$$

This is also valid for atoms where the magnetic moment is created by an electron moving within an orbital. There should additionally be considered the electron as a particle possessing a nonzero mass. The orbital motion of this mass is then connected with atomic angular momentum characterized by the quantum number $\boldsymbol{m_l}$. The total orbital momentum for the whole system of electrons in the orbital is given by $\boldsymbol{L} = \sum \boldsymbol{m_l}$. Therefore, a magnetic moment created by electron movement inside the atomic orbital can be written:

$$\boldsymbol{\mu} = \gamma \boldsymbol{L}, \tag{2.2}$$

where γ is a gyromagnetic ratio. Magnetic moments created at free atoms (ions) are localized and model describing its properties is called localized model of magnetism.

2.2.1. Localized model of magnetism

Electrons have also its own magnetic moment, called spin $\boldsymbol{m_s}$ which has to be taken into account. The resulting magnetic moment of a free atom (ion) is then associated with total angular momentum $\boldsymbol{J}$. The total momentum is dependent on the total spin $\boldsymbol{S} = \sum \boldsymbol{m_s}$ and orbital momentum $\boldsymbol{L} = \sum \boldsymbol{m_l}$, i.e. $\boldsymbol{J} = f(\boldsymbol{S},\boldsymbol{L})$. The occupation of orbitals by electrons is governed by Hund's rules which originate in the principle of reaching minimum energy for the whole system. This includes the Pauli Exclusion Principle (there cannot exist two electrons carrying all four quantum numbers - n,l,m_l,m_s - the same) which is simultaneously obeyed.

Hund's rules [19]:

1 - Maximize total spin angular momentum $\boldsymbol{S} = \sum \boldsymbol{m_s}$. This rule is inclusion of the Pauli Exclusion Principle and originates in the minimization of the Coulomb energy. Electrons with the same positive spin sign ($m_s = +1/2$) occupy the given orbital first.

2 - Maximize orbital angular momentum $\boldsymbol{L}$. This rule reduces the Coulomb repulsion in the sense of the same direction of rotation of electrons in the given orbit.

3 - The value of $\boldsymbol{J}$ is equal to $|\boldsymbol{L} - \boldsymbol{S}|$ if the shell is less than half full and $|\boldsymbol{L} + \boldsymbol{S}|$ for the shell which is more than half full. This rule express minimization of spin-orbit interaction energy.

Magnetic moment of the free ion is analogously defined as $\boldsymbol{\mu} = \gamma \boldsymbol{J}$.

Influence of external magnetic field $\boldsymbol{B}$ on the free atom could be described by additional terms in Hamiltonian:

$$\widehat{\boldsymbol{H}} = \widehat{\boldsymbol{H}}_0 + \mu_\mathrm{B}(\boldsymbol{L} + 2\boldsymbol{S})\boldsymbol{B} + \frac{e^2}{8m_e}\sum_i(\boldsymbol{B} \times \boldsymbol{r}_i)\,, \tag{2.3}$$

where $\widehat{\boldsymbol{H}}_0$ is Hamiltonian of free atom with absence of magnetic field, μ_B is Bohr magneton [19], and m_e is the mass of the electron. The second term on the right side is called paramagnetic term and it describes the magnetic moment of the atom. Third term is called diamagnetic term which expresses response of electrons on the applied magnetic field $\boldsymbol{B}$.

Diamagnetic term reflects tendency of electrons to compensate inner part of an atom from external magnetic field. This causes change of orbital angular momentum and induces magnetic moment in opposite direction to external magnetic field (Lenz's law). Nevertheless, the diamagnetism has to be treated as a quantum mechanical problem. Deeper view into diamagnetism can be reached by the formula showing temperature-independent evolution of magnetic susceptibility in Ref. [19].

Paramagnetic term describes atoms which have magnetic moment originating in unpaired electrons and resulting $\boldsymbol{J}$ is thus non-zero. When magnetic field is applied, the magnetic moment is forced to align parallel to the external magnetic field. The gradual alignment of magnetic moments leads to increase of magnetization. Nevertheless, increasing of temperature causes opposite effect on magnetic moment and randomizes it with increasing of temperature. Therefore is expected that magnetization should be proportional to B/T ratio. Derivation of magnetization with using quantum-mechanical and statistical-physics treatment leads to external magnetic field and temperature dependence of magnetization which follows so called Brillouin function:

$$B_J(y) = \frac{2J+1}{2J}\coth\left(\frac{2J+1}{2J}y\right) - \frac{1}{2J}\coth\left(\frac{y}{2J}\right), \tag{2.4}$$

where $= \frac{g_J \mu_\mathrm{B} J \mu_0 H}{k_\mathrm{B} T}$, g_J is the Landé g-factor and k_B is the Boltzmann constant. Final magnetization is expressed as:

$$M = n g_J \mu_\mathrm{B} J B_J(y)\,, \tag{2.5}$$

where n marks number of atoms per unit volume and μ_B is Bohr magneton. In the case of high magnetic field and very low temperatures or $J \to \infty$ the argument of Brillouin function approach to very high values and Brillouin function limit is 1. Magnetic susceptibility and magnetization is temperature independent in this case. The most interesting and close to real conditions is for $y \ll 1$. The Brillouin function can be approximated and the derived magnetic susceptibility is inversely proportional to temperature, which is called Curie's law:

$$\chi = \frac{M}{H} \approx \frac{n\mu_0\mu_\mathrm{eff}^2}{3k_\mathrm{B}T} = \frac{C}{T}\,, \tag{2.6}$$

where C is Currie constant, μ_eff is effective magnetic moment defined as:

$$\mu_\mathrm{eff} = g_J \mu_\mathrm{B}\sqrt{J(J+1)}\,. \tag{2.7}$$

Atoms situated in the crystal lattice of a metal release conduction electrons which also contribute into magnetic susceptibility and it wasn't taken into account in the previous idea. Conduction electrons in a metal are polarized with spin up and down which are compensated without magnetic field. Application of magnetic field affects this balance and energy of spins with respect to the direction of magnetic field is increasing. This effect is known as Pauli paramagnetism leading to non-zero magnetization and paramagnetic susceptibility. The magnetization is considered as difference between electrons with spin-up $n_\uparrow$ and spin-down $n_\downarrow$:

$$M = \mu_B(n_\uparrow - n_\downarrow) = g(E_F)\mu_B^2 B \ , \tag{2.8}$$

resulting in temperature-independent magnetic susceptibility:

$$\chi_P = \frac{M}{H} = \mu_0 \mu_B^2 \ g(E_F). \tag{2.9}$$

Here, $g(E_F)$ represents the density of states on Fermi level E_F.

2.2.2. Magnetic interactions

Driving force of long- or short-range alignment of magnetic moments are magnetic interactions. Magnetic moments in a solid matter communicate through magnetic interactions which can be divided into two types: magnetic dipolar interaction and exchange interactions.

Magnetic dipolar interaction
This interaction between two magnetic moments have quite low energy. The weakness of this interaction points to playing important role in very low temperatures below Kelvin range where they can be responsible for magnetic ordering in the material.

Exchange interactions
In most cases, the long-range formation of magnetic moments is governed by exchange interaction origins from electrostatic interaction. Exchange interaction arises from solving problem of two electrons in quantum mechanics. This problem was extend for many-body system and recognized effect between all neighboring atoms. The basic equation describing exchange interactions is called Heisenberg Hamiltonian:

$$\widehat{H} = -\sum_{ij} J_{ij} \boldsymbol{S}_i \cdot \boldsymbol{S}_j, \tag{2.10}$$

where J_{ij} is the exchange constant acting between the i^{th} and j^{th} spin [19, 20].

The exchange interactions can be divided into several categories:

- **Direct exchange -** Electrons interact directly via an exchange and correlation interaction and no mediation is needed. A sufficient overlap of neighboring magnetic orbitals is the necessary condition. Materials composed from atoms with 3d, 4d, 5d of 5f orbitals usually provide sufficient overlap of orbitals. The energy of direct exchange interaction is high and allow magnetic ordering even above room temperature for instance Fe in body centered cubic crystal

structure (BCC), Co crystalize in hexagonal structure, Ni in face centered cubic crystal structure (FCC), UFe_2 etc…

- **Indirect exchange: superexchange -** The reason why this exchange is called 'super' is due to longer-ranged interaction. Existence of superexchange interaction is possible owing to non-magnetic mediator. The mediator is non-magnetic ion placed between magnetic ions for instance oxygen. The exchange is governed by the polarization of the outer shells of the mediator.

- **RKKY interaction** – Indirect exchange interaction in metals is called RKKY according names of people who wrote theoretical description (Ruderman, Kittel, Kasuya and Yosida) [19]. The interaction is mediated by conduction electrons which are polarized by one magnetic moment and influence other magnetic moment through this polarization. Following the oscillating character of the electron wave-function the interaction – and especially the sign of the exchange constant J_{RKKY} – is dependent on distance between magnetic moments:

$$J_{\mathrm{RKKY}} \propto \frac{\cos(2k_{\mathrm{F}}r)}{r^3}. \tag{2.11}$$

  This interaction is frequently present in compounds with 4*f* electron magnetic moments and their compounds (e.g. $GdAl_2$, $GdCu_2$) due to localization of 4f magnetic moments.

2.2.3. Itinerant model of magnetism

The theory of magnetism where magnetic moments originate from electrons at atoms has limits and can't explain non-integral value of magnetic moments (for example 2.2 μ_{B} per atom in BCC-Fe crystal) [19]. The non-integral values of magnetic moments are explained by using band structure in metals where the bands can be split and create non-integral value of magnetic moment which can be described by Itinerant magnetism. Electrons released by atoms in metals create chemical bonding and occupy band structure according to Pauli Exclusion Principle. Under certain conditions, electrons with spin-up can be moved into band with electrons with spin-down and its spin switched (or conversely). The energy spent for this change is equal to kinetic energy:

$$\Delta E_{\mathrm{K}} = \frac{1}{2}\mathrm{g}(E_{\mathrm{F}})\delta E^2, \tag{2.12}$$

where $\mathrm{g}(E_{\mathrm{F}})$ is density of states at Fermi level. The change of occupation spins-up and spins-down induce magnetization which interacts with molecular field leading to reduction of this energy. The molecular field energy (or potential energy):

$$\Delta E_{\mathrm{P.E}} = -\frac{1}{2}U(\mathrm{g}(E_{\mathrm{F}})\delta E)^2, \tag{2.13}$$

where *U* is Coulomb energy. Final change of energy:

$$\Delta E = \frac{1}{2}\mathrm{g}(E_\mathrm{F})\delta E^2\big(1 - U\mathrm{g}(E_\mathrm{F})\big). \tag{2.14}$$

The final energy equation clearly says that the spontaneous splitting of bands is favorable for condition $U\mathrm{g}(E_\mathrm{F}) \geq 1$ which is called Stoner criterion and leads to spontaneous ferromagnetism. Depending on the value of $U\mathrm{g}(E_\mathrm{F})$ one can distinguish several cases:

- $U\mathrm{g}(E_\mathrm{F}) < 1$ - Pauli paramagnetism
- $U\mathrm{g}(E_\mathrm{F}) \simeq 1^-$ - Collective metamagnetism
- $U\mathrm{g}(E_\mathrm{F}) \simeq 1^+$ - Weak itinerant ferromagnetism
- $U\mathrm{g}(E_\mathrm{F}) > 1$ - Weak ferromagnetism (due to two not filled subbands with opposite spins, e.gg BCC-Fe)
  - Strong ferromagnetism (subband with lower energy is full, e.g. FCC-Ni)

2.2. Magnetic ordering

Previous chapter deals with origin of magnetic moment and interactions which influence a magnetic moment. This chapter is discussing collective behavior of magnetic moment in materials and describes basic types of magnetic ordering. The magnetic ordering with periodically arranged magnetic moments origins in exchange interactions between magnetic moments.

Ferromagnetic ordering

Ferromagnetic material has spontaneous magnetization which characterizes ferromagnetism and points to parallel alignment of magnetic moments in the simplest case. For ferromagnetic case, the exchange constant J_{ij} (Eq. 2.10) is positive. The fundamental problems of ferromagnetism are solved by using Weiss molecular field definition approximation which replaces the exchange interaction. The Weiss molecular field is a product of surrounding magnetic moments and can be written as:

$$\boldsymbol{B}_\mathrm{mf} = \lambda \boldsymbol{M}, \tag{2.15}$$

where λ is a constant which determines the strength of the system and $\boldsymbol{M}$ is magnetization. The system in external magnetic field is affected by this field $\boldsymbol{B}$ and Weiss molecular field $\boldsymbol{B}_\mathrm{mf}$. The magnetic susceptibility can be written with using Equation (2.6) as:

$$\chi = \frac{\mu_0 M}{(B+B_\mathrm{mf})} = \frac{C}{T}, \tag{2.16}$$

from the expression of external field B one can derive paramagnetic susceptibility:

$$\chi_\mathrm{P} = \frac{C}{T - C\lambda} = \frac{C}{T - \theta_\mathrm{P}}. \tag{2.17}$$

This expression of magnetic susceptibility response in the paramagnetic material is called Curie-Weiss law and θ_P is paramagnetic Curie temperature [19, 20]. The Weiss molecular field is also reflected in the Brillouin function (Eq. 2.4) and magnetization (Eq. 2.5) in small magnetic field leads to $\theta_P = T_C$. T_C is the ordering temperature for ferromagnets called Curie temperature. Schematic temperature dependence of magnetic susceptibility and spontaneous magnetization for ferromagnets in ideal case are plotted in Figure 2.1.

Antiferromagnetic ordering

In the case of negative exchange constant, the exchange is antiparallel and the magnetic moment aligns antiparallel to the next magnetic moment. Characterization of antiferromagnetic material is non-spontaneous magnetization due to compensation by antiparallel alignment of magnetic moments. Frequently, there is used the theory of sublattices. The antiferromagnetic lattice can be considered as two interpenetrating sublattices [19, 20]. Both sublattices are ferromagnetic but inter-sublattice exchange is antiparallel and sublattices are antiferromagnetically oriented with each other Magnetization of sublattices has the same value but opposite orientation resulting non-spontaneous magnetization. Providing these conditions similar derivation as for ferromagnets gives Curie-Weiss law (Eq. 2.17) but for antiferromagnets is $\theta_P = -T_N$ (Néel temperature – ordering temperature for antiferromagnets). Temperature dependence of antiferromagnetic material in ideal case is plotted in Figure 2.1.

Curie-Weiss law is very useful tool for characterization of magnetic interactions in the studied material. Measurement of magnetic susceptibility and fit of the data with the Curie-Weiss law provides us an information about leading ferromagnetic ($\theta_P > 0$) or antiferromagnetic ($\theta_P < 0$) interaction in paramagnetic state with predicts possibility of magnetic ordering type at lower temperature.

Ferrimagnetic ordering

If the ferromagnetic sublattices do not carry the same magnitude of the magnetic moments, the magnetization of these two ferromagnetic sublattices oriented antiparallel are not fully compensated, resulting in non-zero spontaneous magnetization. This case is called ferrimagnetism. Ordering temperature is called Curie temperature but magnetic susceptibility do not follow the Curie-Weiss law [19, 20].

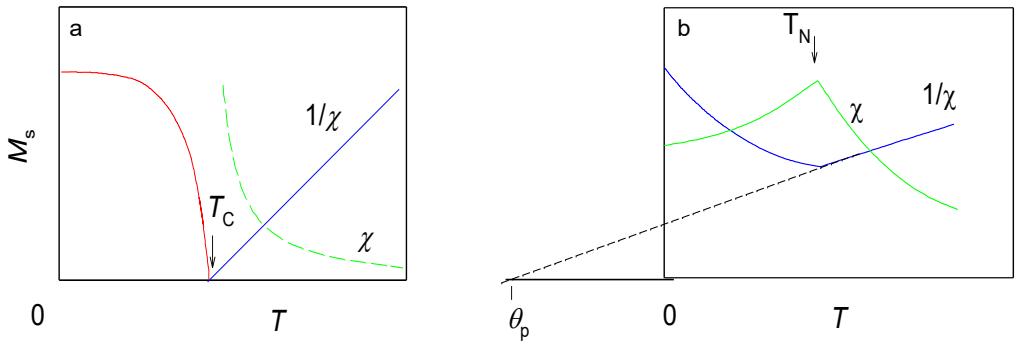

Fig. 2.1: Temperature dependence of paramagnetic susceptibility for (a) ferromagnetic material and (b) antiferromagnetic material [19].

2.3. Magnetism of Uranium materials

Leading parameter for magnetism of uranium materials are 5f-electronic states. The light actinides (Uranium etc.) have 5f-electronic states spatially extended in contrast to 4f-electronic states in lanthanides. Well localized 4f-electronic states in lanthanides give rise to magnetic properties in good agreement with above mentioned properties of free atom. On the other hand, if the U atom is located in the lattice, the magnetic moment is usually delocalized and the 5f-eletronic states bring diversity of behavior according to the degree of delocalization and hybridization of 5f-electronic states. The second parameter which influences magnetic properties is strong spin-orbit interaction which causes strong magnetocrystalline anisotropy in uranium compounds.

As mentioned above, 5f-electron wave functions are spatially extended leading to stronger interaction with surrounding of the atom. It has a consequence in participation of 5f-electrons in bonding which is accompanied with a considerable hybridization of 5f-states with valence states of neighboring atoms. It has serious consequences in formation of a more or less narrow 5f-bands which are intersected by Fermi level E_F leading to a creation of itinerant electron magnetic moment. The magnetic moment is much smaller than that expected one for free U^{3+} and U^{4+} atoms. With satisfactory of broad band limit lead to Pauli paramagnetism and the magnetic moments can also disappear. Influence of high density of 5f-electron states at E_F is also reflected in high value of Somerfield coefficient γ at low temperatures observed in specific heat measurement. The γ coefficient points to strong electron-electron correlation and compounds with high γ coefficient are called heavy fermion compounds. The delocalization also provides direct interaction between 5f-magnetic moments leading to much stronger magnetic coupling than in case of 4f-mangetic moments via RKKY interaction. The most important parameter originating from 5f-5f hybridization is U-U spacing $d_{U\text{-}U}$. This parameter shows that uranium compounds with small $d_{U\text{-}U}$ often have non-magnetic ground state and in most cases a superconductivity is observed. On the other hand, compounds with larger $d_{U\text{-}U}$ are often magnetic if the parameter $d_{U\text{-}U}$ exceeds so called Hill limit ($d_{U\text{-}U} \approx 350$ pm) [21]. Since, the occurrence of the magnetic moment is subject to compliance the Stoner criterion the Hill limit provide satisfactory this condition. Nevertheless, uranium intermetallics have 5f-electrons between 3 (U^{3+}) and 2 (U^{4+}) which influence Coulomb interaction only a little. Therefore, the Stoner criterion is satisfied via density of states at E_F connected with the 5f-bandwidth W_{5f}.

The 5f-bandwidth is strongly sensitive to interatomic distance R as $W_{5f} \sim R^{-6}$ [22] shows high sensitivity of uranium compounds to applied pressure or chemical doping.

There can be also found uranium compounds with large $d_{U\text{-}U}$ (above Hill limit) and non-magnetic ground state. In this cases the 5f-ligand hybridization dominates [23, 24].

As mentioned above, magnetic moment in uranium materials origins from spontaneous splitting of spin-up and spin-down of sub-bands (Section 2.2.3). Itinerant model of magnetism) lead to creation of spin magnetic moment. Nevertheless, 5f-electron bands have similar energy as energy of spin-orbit coupling. This makes striking difference between 5f-itinerant magnetism and 3d-itinerant magnetism where these energies are faraway. The important result of these energy similarities is occurrence of large orbital magnetic moment coupled antiparallel with spin magnetic moment in agreement with Hund's rules [25].

Uranium materials typically report strong magnetocrystalline anisotropy which is caused mainly by two-ion (5f-5f) interaction and also spin-orbit coupling. It is in contrast with lanthanide intermetallics where a single-ion crystalline electric field (CEF) interaction is responsible for magnetocrystalline anisotropy. The system with anisotropic bonding of magnetic moments responses differently on application of magnetic field along crystallographic axes. According the magnetization response there are defined magnetic easy axis – magnetization increases rapidly with increasing magnetic field – and magnetic hard axis – magnetization increases slowly and has linear response. The value used for comparison of magnetocrystalline anisotropy of compounds is frequently used intercept field of both magnetization curves via extrapolation. Uranium materials have intercept field in order of $10^2 – 10^3$ T [26, 27, 12]. Experiments proved that the magnetic easy axis depends on direction of the shortest $d_{U\text{-}U}$. Under a condition that the shortest $d_{U\text{-}U}$ is well defined in a crystal structure, the magnetic easy axis is usually perpendicular to this direction. There can be observed two cases coming from alignment of shortest $d_{U\text{-}U}$: uranium atoms with shortest distance create plane leads to magnetic easy axis oriented perpendicular to this plane, uranium atoms with shortest distance create chain leads to magnetic easy plane.

The above mentioned large-anisotropy materials are considered as Ising-like magnets due to similarities with the Ising model of magnetism [28, 19]. Antiferromagnetic ordering in such materials points to Ising antiferromagnets. The Ising antiferromagnets assume nearest-neighbor and next-nearest-neighbor interactions and at certain conditions they possess magnetic tricritical point (TCP) (Fig. 2) [29]. The transition from the antiferromagnetic to paramagnetic state is second-order type transition from T_N down to temperature of TCP. Below temperature of TCP is first-order transition with hysteresis. The phase diagram of the Ising antiferromagnet with TCP is similar as the ^{3}He-^{4}He mixture phase diagram which possess TCP separating mixing helium fluid with λ transition (AFM-PM transition) and ^{3}He-^{4}He separation into two phases which is first order phase transition (Fig. 2) [30].

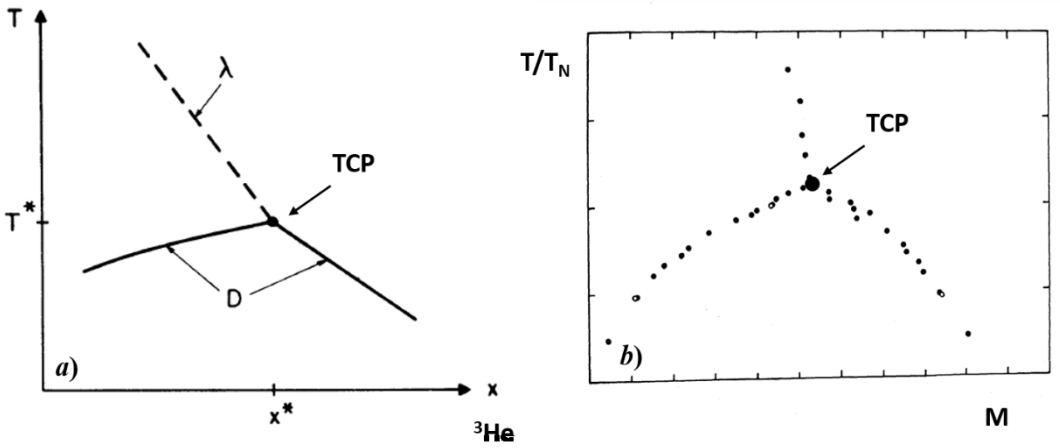

Fig. 2: The figure *a*) represents ^{3}He-^{4}He mixture phase diagram with TCP and The figure *b*) shows similar phase diagram but for Ising antiferromagnet with TCP. Figure taken from [29,30].

2.4. General theory of measured quantities

2.4.1 Heat capacity

Heat capacity of material is composed from several contributions and the most important ones comes from lattice (phonons) $C_{\mathrm{ph}}(T)$, electrons $C_{\mathrm{el}}(T)$, magnetism (magnons) $C_{\mathrm{mag}}(T)$.

The largest contribution to the heat capacity origins in vibrations of atoms of the lattice which allows to propagate collective modes called phonons. At low temperatures an assumption of continuous frequencies of phonons is taken. These phonons with quadratic distribution up to maximal limit are called Deby frequency ω_{D}. Afterwards Debye temperature $\theta_{\mathrm{D}} = \frac{\hbar\omega_{\mathrm{D}}}{k_{\mathrm{B}}}$ can be defined, where k_{B} is Boltzmann constant. Further, with the above mentioned condition the heat capacity in low temperatures [28, 20] can be expressed as:

$$C_{\mathrm{ph}}(T) = 9N_{\mathrm{A}}k_{\mathrm{B}}\left(\frac{T}{\theta_{\mathrm{D}}}\right)^3 \int_0^{\frac{\theta_{\mathrm{D}}}{T}} \frac{e^x x^4}{(e^x-1)^2}\,dx\,, \tag{2.18}$$

where N_{A} is Avogadro constant. The integral leads to $C_{\mathrm{ph}}(T) = \beta T^3$ dependence of heat capacity for low temperatures and satisfy the Dulong-Petit limit $C(T) \approx 3k_{\mathrm{B}}N_{\mathrm{A}}$ for high temperatures.

Another heat capacity contribution occurring in materials is caused by free electrons. This contribution is small in comparison with $C_{\mathrm{ph}}(T)$ but it becomes dominant at low temperatures (below ~10 K) become dominate. Small contribution is caused by limited number of electrons managing from Fermi-Dirac distribution. Only electrons within an interval of the thermal energy $k_{\mathrm{B}}T$ around Fermi energy E_{F} can contribute to heat capacity. Electron heat capacity can be written as [20, 28]:

$$C_{\mathrm{el}}(T) = \frac{\pi^2 N_{\mathrm{A}} k_{\mathrm{B}}^2}{2E_{\mathrm{F}}} T = \frac{\pi^3}{3} \mathrm{g}(E_{\mathrm{F}}) k_{\mathrm{B}}^2 T \,, \tag{2.19}$$

where $\mathrm{g}(E_{\mathrm{F}})$ represents density of states at E_{F}. The Equation 2.19 is frequently used as $C_{\mathrm{el}}(T) = \gamma T$, where γ is the Sommerfeld coefficient which relates with mass of electron $\gamma \sim \mathrm{m_e}$ via $D(E_{\mathrm{F}})$. There should be mentioned that γ reflects the effective mass of electron in the material m^* which can be influenced by many factors. The effective mass of electrons in heavy fermion materials is about two or three orders higher. Consequently, the Sommerfeld coefficient is an important physical quantity for determination the Heavy fermion system [31]. Derived temperature dependences of $C_{\mathrm{el}}(T)$ and $C_{\mathrm{ph}}(T)$ brings simple equation for heat capacity of a non-magnetic material:

$$C_{\mathrm{p}}(T) = \gamma T + \beta T^3 \,, \tag{2.20}$$

which can be used for determination of γ from the low-temperature data plotted as C_{p}/T vs. T^2.

Similar to phonons, magnons contribute into heat capacity for magnetic materials. Magnon is a quasiparticle with collective excitation of magnetic moments. The dispersion relations of magnons are different according to magnetic ordering: quadratic for ferromagnets and ferrimagnets (m = 2), and linear for antiferromagnets (m = 1). The magnetic contribution can be approximately expressed:

$$C_{\mathrm{mag}}(T) \sim T^{\frac{3}{m}} \,. \tag{2.21}$$

The magnetic anisotropy of most magnetic materials influences dispersion relation by opening energy gap Δ. It changes the above mentioned expression to:

$$C_{\mathrm{mag}}(T) \sim \exp\left(-\frac{\Delta}{T}\right) T^{\frac{3}{m}} \,. \tag{2.22}$$

2.4.2 Electric resistivity

Electric resistivity origins in scattering of conduction electrons which influences their mean free path. The scattering processes are independent thus total resistivity is written as a sum of individual scattering contributions. This principle is called Mattheiessen's rule [28, 20] and with considering of three largest contributions the total resistivity can be written as:

$$\rho_{\mathrm{tot}}(T) = \rho_0 + \rho_{\mathrm{ph}}(T) + \rho_{\mathrm{mag}}(T), \tag{2.23}$$

where ρ_0 is residual resistivity, $\rho_{\mathrm{ph}}(T)$ is scattering of electrons on thermal phonons and $\rho_{\mathrm{mag}}(T)$ is contribution from magnetic moments causing scattering of electrons. Residual resistivity is caused by imperfections (defects, vacancies, chemical impurities etc…) of the crystallographic lattice. This scattering mechanism is temperature independent and as it is seen in Equation (2.23) this is limit of the resistivity at 0 K because the other contributions lead to the zero at the limit of 0 K. In the experiments, there is frequently used residual resistivity ratio (RRR) as a comparison value for

quality of the studied sample. The RRR is ratio between resistivity at room temperature ($\rho_{300\mathrm{K}}$) and resistivity at low temperature (ρ_{LT}) which should be very close to ρ_0.

Phonon-electron scattering is proportional to collision rate of phonons and conduction electrons. This rate is proportional to a concentration of phonons which can be simply derived for temperatures above Debye temperature. At temperatures $T > \theta_{\mathrm{D}}$, the phonon concentration is directly proportional to temperature resulting in resistivity dependence as:

$$\rho_{\mathrm{ph}}(T) \sim C_{\mathrm{EP}} T, \tag{2.24}$$

where C_{EP} represents electron-phonon coupling. On the other hand, for temperatures $T < \theta_{\mathrm{D}}$ the temperature dependence of phonon contribution is:

$$\rho_{\mathrm{ph}}(T) \sim C T^5, \tag{2.25}$$

and this proportionality is known as Bloch's T^5 law [28, 20].

The third term in Equation (2.23) is present in magnetic materials and origins in magnon(spin)-electron scattering. In the paramagnetic regime, this scattering is temperature independent and is called spin-disorder resistivity which is proportional to $\sim (g-1)^2 J(J+1)$ [32-35]. Below the ordering temperature electrons are scattered on magnons. This scattered mechanism is temperature dependent and due to different dispersion relation of magnons for ferromagnets and antiferromagnets (see section 2.4.1) the temperature dependence is also different: $\rho_{\mathrm{mag}}(T) \sim T^2$ for ferromagnets and $\rho_{\mathrm{mag}}(T) \sim T^5$ for antiferromagnets [32, 33]. In the case of large magnetic anisotropy, this contribution is affected by the existence of gap in dispersion relation and magnetic contributions are expressed as:

$$\rho_{\mathrm{mag}}^{\mathrm{FM}}(T) = bT^2 \left(1 + \frac{2T}{\Delta}\right) \exp\left(-\frac{T}{\Delta}\right), \tag{2.26}$$

for ferromagnets [12, 32] and

$$\rho_{\mathrm{mag}}^{\mathrm{AFM}}(T) \approx C\Delta^5 \left\{\frac{1}{5}\left(\frac{T}{\Delta}\right)^5 + \left(\frac{T}{\Delta}\right)^4 + \frac{5}{3}\left(\frac{T}{\Delta}\right)^3\right\} \exp\left(-\frac{T}{\Delta}\right), \tag{2.27}$$

for antiferromagnets [36] where Δ is an energy gap corresponding to a gap in heat capacity (Eq. 2.22).

The major contribution to electric resistivity of Uranium-based intermetallics is the magnetic contribution. This contribution is nearly temperature independent in the paramagnetic state but the scattering of conduction electrons on the U magnetic moments is significantly enhanced due to narrow bands at the E_{F} by 5f-electrons carrying magnetic moment. The temperature dependence of magnetic contribution below ordering temperature is driven by scattering on magnons with the above mentioned features. These compounds exhibit observable electron-electron scattering at low temperatures which is manifested as $\rho_{\mathrm{el}}(T) = aT^2$ dependence and it is called Fermi-liquid behavior. The value of parameter a is enhanced in comparison with simple metals. The parameter can be approximately scaled with Sommerfeld coefficient as $a/\gamma^2 \approx 10^{-5}$ $\mu\Omega\cdot\mathrm{cm}\cdot\mathrm{K}^2\cdot\mathrm{mol}^2\cdot\mathrm{mJ}^{-2}$ for heavy fermions [37].

Application of magnetic field, the charge carriers are affected by Lorentz force. According the Figure 2.3 charge carriers are forced by Lorentz force in negative *y*-direction and create transversal field (or Hall field) E_y in order to compensate the Lorentz force. It results in creation of electric resistivity (called Hall resistivity, ρ_H) dependence on $R_{Hall} \cdot \boldsymbol{H}$, where R_{Hall} is Hall coefficient and $\boldsymbol{H}$ is magnetic field. The effect is called ordinary Hall effect. The electron movement problem in external magnetic field gives $R_{Hall} = -1/ne$, where n is charge carrier density and "e" is charge of electron. It is obvious that Hall coefficient depends on charge-carrier density, only [28, 20]. The magnetic materials possess magnetization which has a consequence in creation other contribution into Hall resistivity called the anomalous Hall effect (AHE). The total Hall resistivity of magnetic materials is described empirically as a sum of two terms; the normal and anomalous Hall resistivity [38-42]:

$$\rho_H(H) = R_H \mu_0 H = R_{Hall} \mu_0 H + R_s M, \tag{2.28}$$

where R_S is the anomalous Hall coefficient, M is magnetization. An AHE reflects three different mechanisms. The first one is caused by intrinsic features of band structure (called Berry phase), the other two mechanisms origin from the skew-scattering and side-jump scattering of conduction electrons. The AHE can be written as:

$$R_S = a\rho + b\rho^2, \tag{2.29}$$

where $a\rho$ represents skew scattering and $b\rho^2$ the intrinsic and side-scattering mechanism [39, 40]. This empirical formula agrees with experimental data for many materials.

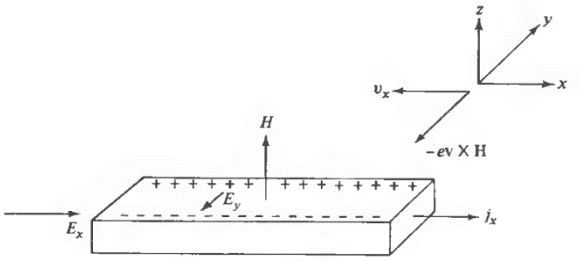

Fig. 2.3: Arrangement of Hall resistivity measurement [28]

2.4.3 Thermal expansion and magnetostriction

The dimensions change of the material is expressed by relative length change of the sample $\Delta l_{sample}/l$. The characteristic feature of the material is thermal expansion coefficient which is defined as:

$$\alpha_i(T) = \frac{1}{l} \cdot \frac{dl(T)}{dT}, \tag{2.30}$$

where i marks crystallographic direction which was measured within the experiment. If the change of the length is small for small temperature changes in an isotropic material, the volume expansion coefficient can be written as:

$$\alpha_v(T) \approx \alpha_a(T) + \alpha_b(T) + \alpha_c(T), \tag{2.31}$$

where thermal expansion coefficient have been measured along three orthogonal axes.

In magnetic materials, the change of volume can also be caused by application of external magnetic field. The volume changes caused by external magnetic field are called magnetostriction. Magnetostriction for itinerant system has simple relation with compressibility and magnetization as:

$$\frac{\Delta \mathrm{V}}{\mathrm{V_0}} = \kappa \cdot \mathrm{C_{ME}} \cdot M^2, \tag{2.32}$$

where $\mathrm{C_{ME}}$ is magnetoelastic-coupling constant [43].

Ehrenfest relation

The thermodynamics provides useful relation for estimation of transition-temperature dependence with pressure. The second order phase transitions which has continuous change of entropy underline Ehrenfest relation:

$$\frac{\mathrm{d}T_c}{\mathrm{d}p_i} = V_\mathrm{m} \cdot \frac{\Delta\alpha_i}{\Delta(C_p/T)}, \tag{2.33}$$

where $\Delta\alpha_i$ is change of the thermal expansion coefficient at the transition, $\Delta C_p/T$ is step of specific heat divided by temperature at the transition and V_m is molar volume of the elemental unit. The Ehrenfest relation makes estimation for uniaxial pressure evolution of the transition which depends on thermal expansion coefficient measured along certain crystallographic direction. The estimation for hydrostatic pressure evolution can be done by using volume expansion coefficient (Eq. 2.31).

2.5. Pressure effects to solid state materials

Pressure definition

Generally, the pressure is defined as a force (F) per unit area (A):

$$p = \frac{F}{A}. \tag{2.34}$$

In laboratory conditions a more specific definition by stress tensor σ_{ij} is used:

$$\sigma_{ij} = \begin{pmatrix} \sigma_{11} & \sigma_{12} & \sigma_{13} \\ \sigma_{21} & \sigma_{22} & \sigma_{23} \\ \sigma_{31} & \sigma_{32} & \sigma_{33} \end{pmatrix}, \tag{2.35}$$

which is defined in Cartesian coordinate system. One can imagine the stress tensor as a stress acting on planes of an infinitesimal cube. Three component of stress along all three directions are needed for the description of stress on infinitesimal cube. The

diagonal components of the stress tensor are normal to the surface of infinitesimal cube and represents direct stress. The off-diagonal components are tangential to the surface of infinitesimal cube and represents shear stress. With using the stress tensor, the pressure is defined:

Hydrostatic pressure $$p = -\sigma_{11} = -\sigma_{22} = -\sigma_{33};\ \sigma_{ij} = 0, i \neq j \quad (2.36)$$

Quasi-hydrostatic pressure $$p = -\frac{1}{3}\sum \sigma_{ii}\ ;\ \sigma_{ij} \neq 0, i \neq j \quad (2.37)$$

Uniaxial pressure $$p = -\frac{\sigma_{11}}{3}; \sigma_{22} \neq 0;\ \sigma_{22} = \sigma_{33} = 0. \quad (2.38)$$

Effect to solid state materials

The external pressure changes the distances of the atoms in the crystal lattice. In the case of static pressures we distinguish hydrostatic pressure and uniaxial pressure. Hydrostatic pressure changes lattice parameters which may be decreased or increased but the resulting volume decreases. Uniaxial pressure means the application of the pressure exclusively along one particular direction. The lattice parameter of the chosen crystallographic axis is forced by pressure to make it shorter but the final volume is not necessarily decreased and my also remain unchanged. The changes of interatomic distances can lead to crucial modifications of materials properties (e.g. electrical resistivity, band structure, magnetic moment, strength of magnetic interactions etc.) or even change of bonding. Therefore, pressure is other tuning parameter in experimental science as one of the parameters in the equation of state.

The parameter describing pressure effect on the material is compressibility κ which is defined as:

$$\kappa = -\frac{1}{V}\left(\frac{dV}{dp}\right)_T. \quad (2.39)$$

Shrinking of interatomic distances by application of pressure affects outer electrons and band structure which are very sensitive to this change. Existing overlap of wave functions is increased leading to broadening of the energy bands, increase of delocalization of the electrons and can have a consequence in change of boding (ionic → covalent → metallic) in very high pressure. Increasing overlap of wave functions also influences density of states at Fermi level ($g(E_\mathrm{F})$) which decreases due to band-broadening. Even though the Coulomb interaction increases with larger overlap, the fulfill of Stoner criterion (see in section 2.2.3) is difficult. Application of enough pressure destroys itinerant magnetism via band-broadening [44]. Nevertheless, band structure is very complex and can initialize increasing of $g(E_\mathrm{F})$ over certain pressure range leading to stabilization of magnetism. On the other hand from the point of view of magnetism, 4f-electrons based magnetic moment is well localized. Nevertheless, sufficient high pressure can bring neighborhood atoms close enough that 4f-wave functions start to overlap. According to the Stoner criterion the 4f-electrons can further create magnetic moment but it changes to itinerant magnetism. Finally, further increasing pressure leads to loss of magnetic moment [44]. As it was mentioned in section 2.2.2, leading parameter for creation of magnetic ordering is exchange interaction and therefore magnetic ordering temperature depends on pressure influence on the exchange interactions.

3. Experimental methods

3.1. Sample preparation

Studied samples in this thesis have been prepared in technology lab of the Department of Condensed Matter Physics. The technology lab provides possibility of using several methods for the single crystal samples growth [45]. For the $UIrSi_3$ single crystals preparation the floating zone melting method was used. Before growing of the crystals polycrystalline samples with the proper stoichiometry were melted.

Polycrystalline samples were prepared in the mono-arc furnace (Fig. 3.1) dedicated for preparation of intermetallic compounds from initial pure elements.

Fig. 3.1: The mono-arc furnace for preparation of polycrystalline samples [45].

In mono-arc furnace, the requested amount of constituent elements in the ratio corresponding to stoichiometric composition is placed on a Cu crucible inside the chamber which is evacuated (10^{-6} mbar). During the evacuation process the walls are heated to desorb gases. After evacuation, the chamber is filled by the Ar protective atmosphere (6N purity). Pure elements are melted by electric current together. The crucible, walls and electrode are cooled by cold water during the melting process. The obtained sample is turned over and remelted several times for better homogeneity.

In order to prepare a rod for the floating zone method, polycrystalline pieces (2 pieces) in the amount of approx. 5 g was prepared by the above-mentioned process are then crashed into small pieces and put into a special Cu crucible for making rods. The pieces are melted in the mono-arc into a rod ingot of the requested material which can be then used for growing of a single crystal by using the floating zone melting method.

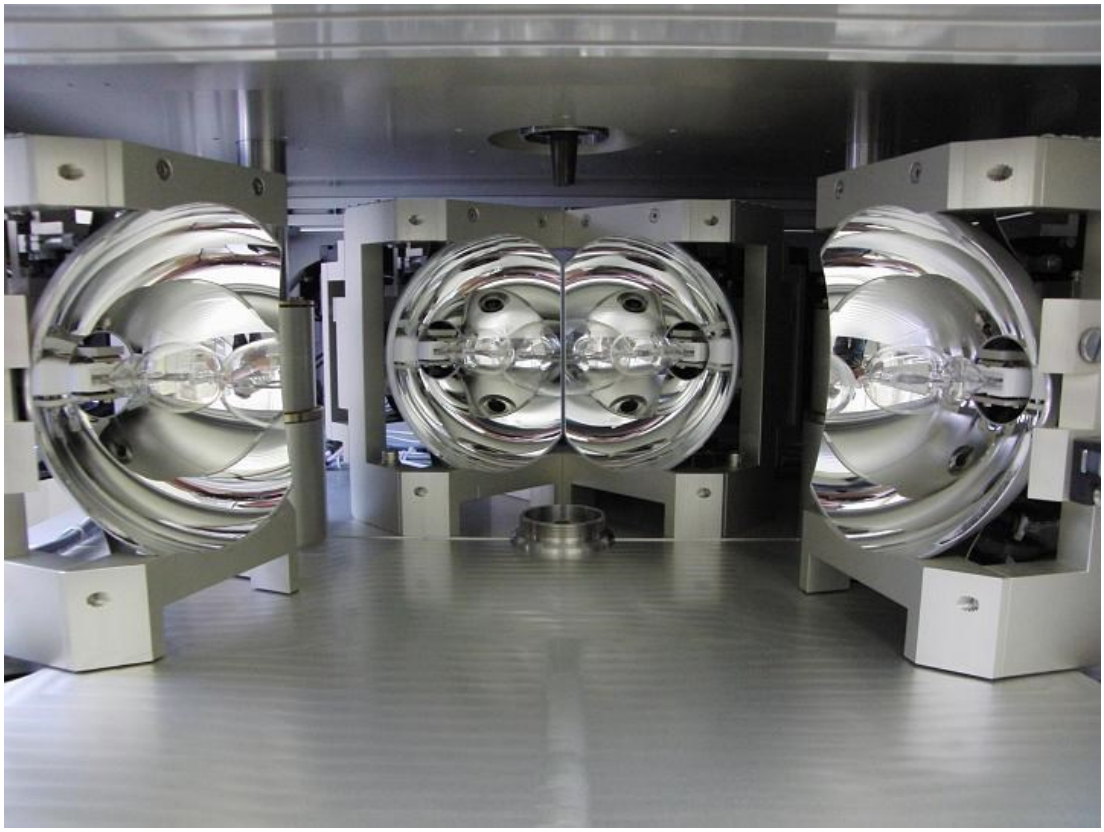

Fig. 3.2: Four-mirror furnace with halogen lamps in the open state [45].

The device dedicated for the floating zone melting method (made by Crystal Systems Corp., Japan), consists of four-mirror optical furnaces with halogen lamps (with power of each lamp 1 000 W) (Fig. 3.2). The prepared rod of the considered material has two parts (a short one - approx. 2 cm - and a long one – approx. 8 cm) which are fixed by holders using a tantalum wire. Chamber of the device with the material is closed and evacuated (around 10^{-6} mbar). The chamber is then filled by the argon (6N) protection atmosphere with overpressure atmospheric pressure. During the growing of crystals the argon flow (~ 0.25 – 0.5 dm^3/min) is used. The two parts of the sample rod approach to each other at the focus point of the mirrors. The four-mirror with halogen lamps in the proper positions make then both parts of the sample rod melt and make them joined. The rod is then pulled slowly through the hot zone.

Samples without any other heat treatment are called as-cast samples. These samples where fast cooling causes high internal lattice stress, may easily crack and it can lead to miss occupancy of the atoms resulting in lattice defects and possibly also the impurity phase creation. These involuntary changes can be fully or partly removed by annealing process. Samples for annealing are wrapped in a tantalum foil and closed in evacuated (below 10^{-6} mbar) quartz tube. The quartz tube is placed into a furnace where the annealing process takes place. Usually, a temperature close to the recrystallization temperature or melting point of the annealed material sample is reached and kept for several hours or days. Further, temperature is decreases with low cooling rate to allow adiabatic relaxation of the lattice and to avoid lattice imperfections, internal stress, vacancies etc.

3.2. Sample characterization

The prepared samples were characterized with several experimental methods allowing observation of crystal structure, real stoichiometry, presence of crystallographic phases and chemical purities. X-ray power diffraction and scanning electron microscope with EDX analyzer (Energy Dispersive X-ray analysis) was used for structural characterization and phase purity of investigated materials. Laue x-ray diffraction method was used for confirmation of the crystallinity and orientation of the single crystals.

3.2.1. X-ray powder diffraction

Frequently used method for characterization of samples (phase composition, crystal structure and lattice parameters determination) is the x-ray powder diffraction (XRPD). Measurements of XRPD were performed using Bruker D8 Advanced and Seifert XRD7 diffractometers both working in Bragg-Brentano parafocusing geometry. X-ray source is a sealed tube with copper anode (wave lengths $\lambda_{K\alpha1} = 1.54050 \cdot 10^{-10}$ m and $\lambda_{K\alpha2} = 1.54434 \cdot 10^{-10}$ m in both cases). Background is eliminated by monochromatic filters. Piece of an analyzed sample is powdered and fixed on a glass plate which is placed inside the diffractometer.

Measured diffraction patterns were evaluated by the whole pattern fitting procedure - Rietveld method [46] using the FullProf program [47, 48]. The method is based on refinement of parameters which are approximately estimated for certain crystal structure. Therefore, a structural model containing basic information about crystal structure and external conditions (space group number, atomic positons, wave length, background level etc.) has to be provide at a starting point. The program calculates a diffraction pattern based on the structural model in each measured point. Calculated diffraction pattern is compared with the measured diffraction intensities and by variation of the refined parameters it searches for the best agreement [49]. The sum of residuals between calculated and measured diffraction patterns is minimized during the fitting (the least squares method).

The method allows us to get the phase composition, the lattice parameters, atomic positions, occupancy, and texture.

3.2.2. Scanning electron microscope

The studied samples were analyzed using scanning electron microscope (SEM) Tescan Mira I LMH equipped with an energy dispersive x-ray analyzer (EDX) Bruker AXS. Scanning electron microscope scans the sample surface with a high-energy electron beam. It displays pictures created by the secondary electrons and backscattered electrons.

The electron's beam interacts with material and produces secondary electrons from the surface of the scanned material. These electrons provide information about the surface topography. The backscattered electrons are reflected from the sample due to elastic scattering. Signal of these electrons is strongly influenced by atomic number of the specimen. The image of backscattered electrons provides information about atomic distribution and can reveal foreign phases.

EDX allows observing of elemental composition of the sample. The method consists in measurement of characteristic x-ray of certain atoms. Characteristic x-ray is emitted by excited atoms from a surface of the sample due to high intensity beam of electrons. The excited atom emits electrons from its inner shell. Empty state after the emitted electron is then occupied by electrons from higher situated energy shells. This process is accompanied with emission of a photon with energy corresponding to the energy difference between its previous and the new energy levels. Such a ray is called characteristic radiation and it has a unique energy scheme for each atom what enables to distinguish the types of atoms present in the studied material.

3.2.3. Laue method

Laue method is fast and useful method for orientation and determination of quality of single crystals. Equipment provided by technology lab of DCMP allows working with oriented crystals to prepare needed shape of single crystal (for example: cube or rectangular shape where *a*,*b*,*c* crystal axes direct perpendicular to sides of the shape). The orientations of single crystals were performed using the x-ray Laue System by Photonic Science, UK. The device provides back reflection arrangement of Laue method and diffracted pattern is recorded on a CCD detector with 155×105 mm. The standard distance between the sample and detector is 3.9 cm. The Laue device using polychromatic x-ray beam is scattered by a single crystal with resulting diffractions by agreement of diffraction condition [49]. The image created from reflections is called Laueogram and has characteristic scheme according to the crystal structure of the measured single crystal which allows single crystal orientation.

3.3. Measurement techniques at ambient pressure

Measurements of bulk properties (electrical resistivity, magnetization, specific heat, dilatometry…) were carried out in the Joint Laboratory for Magnetic Studies (JLMS) operated by the Department of Condensed Matter Physics, and the Institute of Physics of the Academy of Sciences of the Czech Republic. Measurement were carried out with using the following devices: MPMS 7XL (Magnetic Property Measurement System) which uses a very sensitive detector SQUID (Superconducting Quantum Interference Device), PPMS (Physical Property Measurement System), both from Quantum Design [50, 51] and Closed Cycle Refrigerator (CCR) from Janis Research/Sumitomo Heavy Industries.

3.3.1. MPMS

The MPMS is a standard device for measuring of magnetic flux with high precision. For that a SQUID technology is used (Superconducting Quantum Interference Device). The technology allows to detect measurement of magnetization (magnetic moment) on the lowest possible level. In principle, the technology is capable to distinguish the quantum of magnetic flux. We used MPMS 7XL device which is shown in Figure 3.3.

The MPMS device is composed of four main parts: a sample chamber, superconducting detection coils, the SQUID detector and a superconducting magnet. Scheme of main parts of the device is shown in Figure 3.4. The SQUID is made from two superconducting wires (e.g. Nd) which are separated by two very tinny layers from non-conducting materials (e.g. Al_2O_3). This junction between superconducting - non-conducting - superconducting materials is called Josephson's junction. We can consider the SQUID as a superconducting loop separated by two Josephson's junctions. Josephson's junctions make the SQUID the best convertor of magnetic flux to voltage where a quantum magnetic flux can be measured (*h/2e*, for more information see [52]). In principle, the SQUID works as a detector of magnetic flux change: it measures difference between magnetic flux in the loop which is generated from detection coils and a ticker coil. The ticker coil makes balance of the change of magnetic flux inside the SQUID loop therefore a feedback voltage is proportional to the magnetic flux of the detection coil.

External magnetic field is generated by superconducting magnet. The magnet is permanently inside the liquid helium reservoir in order the superconducting wires are in the superconducting state. Detection coils, which are made of superconducting material as well, are oriented in gradiometer set-up with sample in the middle. The measurement is done by moving of the sample inside the gradiometer. According to principle of Faraday's law, in the detection coil is induced electric current which is proportional to magnetic flux.

Fig. 3.3: MPMS 7XL [53]

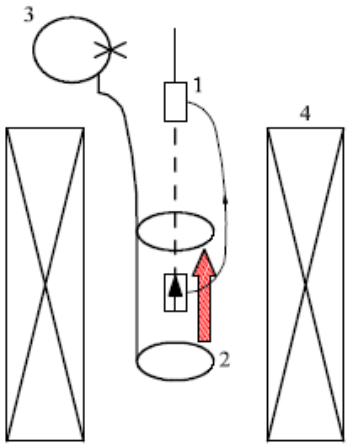

Fig. 3.4: Schema of main parts of the MPMS device: 1 – sample, 2 – superconducting coils, 3 – SQUID, 4 – superconducting magnet [54]

3.3.2. PPMS

The PPMS is a device with installed superconducting magnet (9 T or 14 T) providing possibility of numerous types of physical properties: magnetization, magnetic susceptibility, heat capacity, electric resistivity and thermal transport. The scheme of the device is shown in Figure 3.5. It consists of dewar bottle with liquid nitrogen and helium where the superconducting magnet is submerged permanently. Sample chamber has a universal 12pin holder on the bottom for connecting of special insert provided each experimental option. The device is controlled by using MultiVu [55] software for all experimental options. Measurement can be operated in temperatures between 1.8 – 400 K and with applied external magnetic field up to 9 or 14 T.

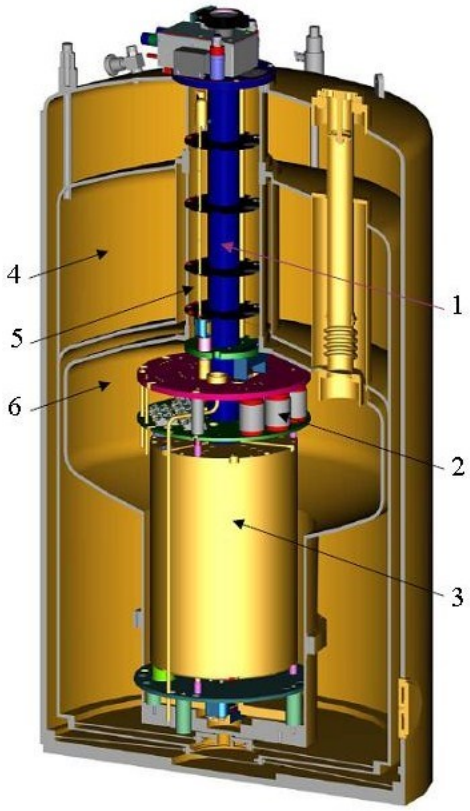

1 - PPMS probe inserted through top of dewar
2 - Magnet protection circuit
3 - Superconducting magnet
4 - Liquid nitrogen reservoir
5 - High-T_c Magnet Leads
6 - Liquid helium reservoir

Fig. 3.5: Scheme of the PPMS device [53].

Magnetic measurements in PPMS

For magnetic measurements, PPMS provides two experimental options ACMS (AC Measurement System) and VSM (Vibration Sample Magnetometer). Both options are using the induction Faraday's law. DC magnetization of the sample is measured inside detection coils where the sample is moving while a non-zero external magnetic field is applied. Resulting voltage proportional to magnetization of the sample is induced in the detection coils. The device can measure magnetization of the sample at applied magnetic field up to 14T. Alternating (AC) magnetic susceptibility in ACMS option can be measured with using detection and excitation coils which are co-axial.

The excitation coil is connected to a source of alternating current at certain frequency (10 Hz – 10 kHz) which generates alternating magnetic field inside the coil. The sample responds due to the alternating magnetic field and this response is detected by the secondary (detection) coils. In case of VSM the sample is located inside the set of detection coils where the signal is obtained upon vibration of sample inside a stable nonzero external magnetic field. This method was an advantage in faster measurement in good sensibility down to 10^{-6} emu. The VSM option is additionally equipped with the oven which can reach 900 K for measurement in high temperatures.

Electrical transport measurement in PPMS

Electrical transport measured by PPMS uses lock-in amplifier providing current range 0.01 – 100 mA and frequency range 0.1 – 200 Hz [56]. Small and tiny samples as well as experiments in very low temperatures (0.3 – 5 K) are measured with low electrical current up to 0.3 mA to avoid heating of the sample due to the passing current (Joule's heat). Prepared samples are fixed on the special puck (Fig. 3.6). Fixed sample is contacted by four gold wires (25 μm in diameter) with using colloidal silver paste or spot welding. Micromanipulators connected to spot welding electronics can be used to improve precision in case of very small samples and wires to help to filter out hand shaking. Besides the mechanical hand manipulators and also electronic manipulators with spot welding electronics are available for still more precise work, namely in case of samples with length smaller than 1 mm. Electrical resistance is measured by standard four point method for to eliminate the contribution of contacts and connecting wires which have usually higher resistance than the measured sample.

Fig. 3.6: Special puck for measurement of electric resistivity by Quantum Design [53].

Specific heat

The measurements of specific heat were performed with using of PPMS devices. The 2-τ relaxation method is utilized for specific heat measurement [51]. Sample is placed inside a special puck (Quantum Design, Fig. 3.7) on a corundum plate with dimensions 3×3 mm and between the sample and plate Apiezon grease is inserted for good thermal contact. On the puck there are two Cernox-type thermometers and a heater mounted on the bottom of the sapphire plate. The puck has also a radiation cover and is inserted into PPMS chamber where a high vacuum (< 10^{-3} mbar) is reached for thermal insulation from the surrounding. During the measurement process the plane is heated by using a defined heat pulse with simultaneous recording the temperature of the sample with time. Temperature is recorded also during cooling of the sample to observe all response of the sample on the defined heat pulse. This response is

subsequently fitted by two exponential functions to obtain specific heat of the sample. Resulting specific heat can contains contribution from Apiezon grease ("addenda") which can be subtracted by measurement of the known specific heat of Apiezon grease from the calibration measurement of the addenda itself prior to inserting the sample on the plate. The PPMS device allows also the use a single-slope method where a long heat pulse of several Kelvins is used and recorded response of the sample is fitted by two exponentials separately (heating, cooling). This method is especially useful for measurements of first-order type transitions.

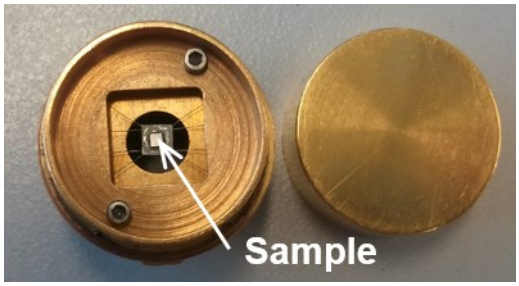

Fig. 3.7: Sample puck for measurement of heat capacity.

Dilatometry measurement

Thermal expansion and magnetostriction measurements were carried out with using microdilatometric cell and PPMS device. Microdilatometric cell used in JLMS works on a principle of change of capacitance as a function the distance between capacitors [57]. The sample placed inside the cell is the governing parameter changing this distance. The cell is made of silver due to low heat capacity without nuclear contribution at low temperatures and low influence from high magnetic field. Schematic drawing of the cell is shown in Figure 3.8. The maximum sample size is $3\times3\times3$ mm^3, and the sample must have one flat surface which sits on the sample support. The microdilatometric cell is specially developed for use inside PPMS which provides measurement under conditions available in this device (low temperatures, magnetic field) and for measurement of small samples. Calibration with using silver standard sample defines a detailed formula describing the relation $C(T) \leftrightarrow \{\Delta l/l\}(T)$. It can be found in the literature [57]. The capacitance is measured by using the Andeen-Hagerling AH2500A capacitance bridge. The data about sample environment and capacitance are recorded by using interface software which communicates with MultiVu and capacitance bridge. It provides control and change of temperature and magnetic field during the measurement.

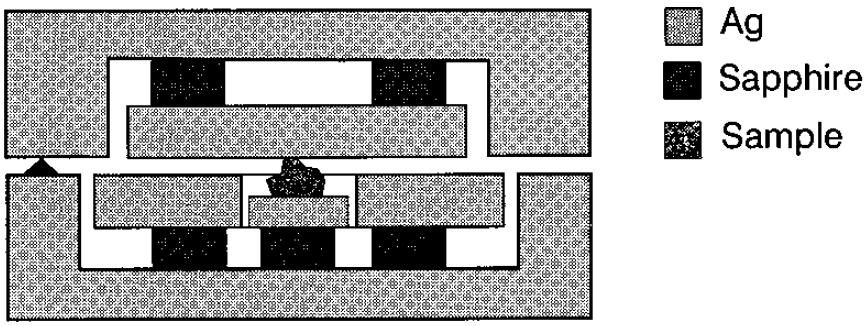

Fig 3.8: Schematic drawing of the microdilatometric cell [57].

3.3.3. Closed Cycle Refrigerator

The closed cycle refrigerator is constructed for temperature dependence measurements of electric resistivity down to 3 K without using cryogenic liquids. The electrical resistivity is measured by lock-in amplifiers (SR830) with voltage source between 0.004 V – 5 V and frequencies 0.01 Hz – 102 kHz [58]. Due to lacking of current source the current circulating in the electric circuit is measured by Keithley 2002 multimeter using measurement of voltage on the thermally stabilized resistance standard. The obtained current and voltage measured on the sample is then used for recalculating of the sample resistivity. The advantage of Closed Cycle Refrigerator is enough large sample space allowing to fix both – sample puck as for use in PPMS (Fig 3.6) making this measurement method compatible – and also all types of pressure cells can be mounted inside the Closed Cycle Refrigerator.

3.4. High pressure cells

Measurements under high pressure require patience and carefulness during experimental preparation of the measurement setup and closing of the pressure cells. Depending on the type of pressure – hydrostatic and uniaxial – the construction of the pressure cell is to be chosen. For hydrostatic pressures the pressure is usually generated by pushing of a piston into a sample space which is filled by the pressure transmitting medium. Many types of hydrostatic pressure cells exist from very sophisticated ones (3D multi-anvils cells) through anvil pressure cells to simple clamp piston pressure cells, depending on the requested pressure range and quality of hydrostatic conditions. On the other hand, there are several limiting factors - sample space size, temperature and magnetic field range, type of measured physical property and many others. Further, pressure cells can be characterized according to the stability of the resulting pressures – Static or Dynamic pressures. Dynamical pressures are characteristic for a shot-like reaching pressures which preserves their use at low temperatures due to increasing temperature during the pressurizing process. These cells reach much higher pressures than the cells for using the static pressures but for very short time. Devices reaching dynamic pressures are moreover very sophisticated, large and they are located in big scientific centers [59]. For the purpose of measurements in frame of this thesis the static pressures are used, which are suitable for the high-pressure and low-temperature measurements of the studied compounds.

The pressure cells available in the laboratories of the Department of Condensed Matter Physics (and MGML – see https://mgml.eu/) consist of the piston-cylinder clamp pressure cells (clamp pressure cell, CPC), Bridgman-anvil type pressure cells (Bridgman cells, BAC) [60] and miniature uniaxial pressure cell [61]. Clamp pressure cells are designed for measurements under hydrostatic pressure. As a pressure transmitting medium a special liquid with low compressibility is being used. Pressure is increased by pushing a piston into a bore of the pressure cell (sample space). The pressure conservation is managed by screws holding the piston in a required positon. This type of pressure cells exists in many different variants and dimensions depending on the requested type of measured quantity and simultaneously to ensure compatibility with other devices.

Bridgman cells are based on two parallel anvils located inside the body of the pressure cell. The measured sample is located in sample space between these anvils

which is sealed by a gasket. Increasing of pressure is reached by moving anvils against each other. As the pressurizing process includes plastic deformation of the gasket, the pressure sequence can be scheduled only with increasing pressure order. BAC's usually reach higher pressures than the clamp pressure cells. It has smaller sample volume and area perpendicular to acting force. Smaller conserved energy makes this type of cells safer. Sometimes a perfect hydrostaticity is not reached and a partial uniaxial pressure contribution is present in these cells leads to the quasihydrostatic pressure (see section 2.5).

Other type of pressure measurement uses uniaxial pressure (definition is written in section 2.5). The sample with precisely parallel planes with normal to the requested uniaxial acting is located between two pistons and due to lacking of pressure transmitting medium the stress is applied only along one direction of the pistons, and thus along one particular direction of the studied crystal. Compression of the sample along one directions is very useful in studies of highly anisotropic materials where the properties embody differences along different axis.

3.4.1. Uniaxial pressure cells for measurement in the MPMS

Magnetization measurements in MPMS were performed with using miniature uniaxial pressure cell. This uniaxial pressure cell was designed and constructed specially for measurements inside the MPMS device by scientists from Institute of Physics of the Czech Academy of Sciences [61]. The pressure is applied along center line of the pressure cell (see Fig. 3.9) which requires sufficiently polished and highly plan-parallel surfaces of the oriented single crystal. Pressure transmitting medium is not used in this case and pressure is determined directly from the definition: applied force (F) divided by area the of sample surface (A) which presses pistons ($p = \frac{F}{A}$). The pressure cell is made of a non-magnetic CuBe bronze but pistons are made of ZrO-ceramic. The sensitively controlled force is generated by Belleville springs (CuBe disc-shaped springs) with maximum force 20 kN. The generated force is calibrated from compressing of Belleville springs via precision load transducer [61].

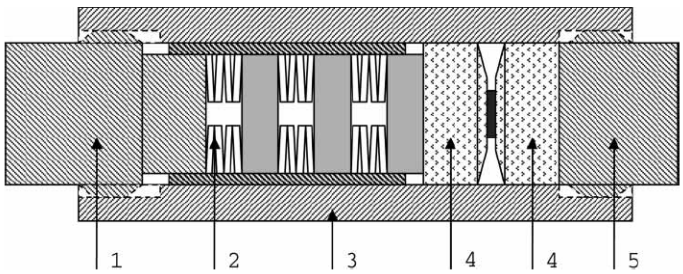

Fig. 3.9: Schematic drawing of miniature uniaxial pressure cell: 1 – CuBe squeezing screw, 2 – set of the Belleville springs, 3 – CuBe cell, 4 – ZrO pistons, 5 – CuBe fixing screw [61].

3.4.2. Clamp pressure cell

The piston-cylinder clamp pressure cell used in PPMS devices, is commercial product from the C&T Factory Co., Ltd - Figure 3.10. The pressure cell consists of two layers.

Arrangement of the two layers together makes main body of the cell which allows achieving higher pressures compared to a single-layer pressure cell with the same outer diameter. The inner layer is made of Ni-Cr-Al alloy and the outer layer is made of CuBe alloy. The pressure cell is designed for safety pressure up to 3 GPa and the outer diameter is 25 mm assures the compatibility with PPMS devices. The pressure cell together with a PPMS device allows measurements in temperatures down to 2 K and in magnetic field up to 14 T. The Daphne oil 7373 is used as a pressure transmitting medium [62-64]. The measured signal is conducted by Cu wires (0.1 mm in diameter) passing through the plug out of the pressure cell (Fig. 3.10). The wires are fixed inside the plug by Stycast 2850 FT epoxy. Before closing of the pressure cell the plug is used as a sample holder and wires are connected to the sample or any other component necessary for a measurement (AC coil etc.). The other wires are used for connection with a manometer. Pressure inside the cell is measured with using manganin wire as a manometer. The pressure is determined by the change of electric resistivity of the manganin wire. The pressure dependence of electric resistivity is expressed by the formula:

$$R(T,p) = R(T,0)[1 + p\alpha(T)],$$
$$p(T) = \frac{R(T,p)-R(T,0)}{R(T,0)}\frac{1}{\alpha(T)}, \quad (3.1)$$

where R marks electric resistivity of a manganin wire, p marks pressure and α is a pressure coefficient of electric resistivity of the manganin wire which depends on the diameter of manganin wire and real composition of wire (in our case it is α (293K) = 0.0245 GPa^{-1}) [65].

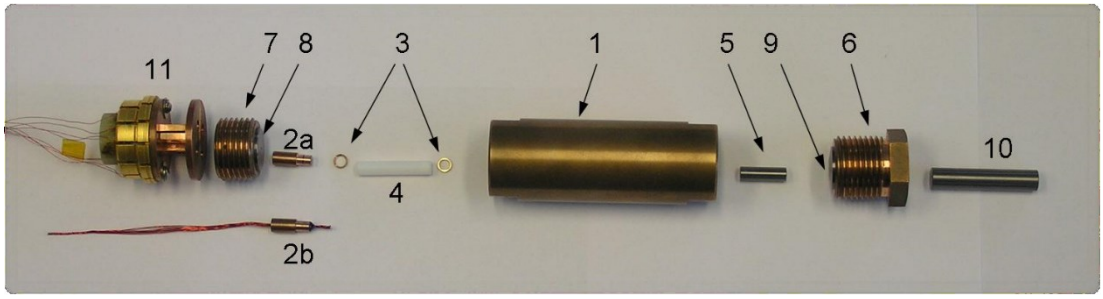

Fig. 3.10: Double layered CuBe/NiCrAl piston-cylinder pressure cell for measurements in PPMS and CCR devices. 1 – body of the pressure cell, 2a – plug, 2b – plug with sealed Cu wires, 3 – CuBe sealing rings, 4 – teflon capsule, 5 – piston, 6 and 7 – upper and lower fixing screw, 8 a 9 – WC support of plug and piston, 10 – WC rod for application of the load in the hydraulic press, 11 – puck with reduction for connection with PPMS devices from Quantum Design.

The design of the cell allows its use in most of equipment available in the laboratories of DCMP (MGML) – i.e. PPMS, DR, 20T, CCR.

Measurement of electrical resistivity with using clamp pressure cells

Measurements of electrical resistivity of the studied samples under pressure were performed in the 4-wires connection allowing measurements of small values of

electrical resistance, usually measured on small-size samples of intermetallic compounds. It can be performed at high pressures as well due to electric insulating properties of pressure transmitting medium and teflon capsule which protects short-circuit to the main body of the pressure-cell. Non-insulated wires (gold, silver, copper or platinum with 25 μm in diameter) were used for experimental assembly of electrical resistivity measurement under applied hydrostatic pressure. The assembly of high pressure experiment of electric resistivity is shown in Figure 3.11. The size of the sample is necessary to be adjusted due to restricted sample space (2.7 mm in diameter and 17 mm in length). The usual dimensions of the sample are ~ 0.3 x 0.5 x 2 mm^3. The standard four point method is used in measurement of electrical resistance of both - a sample and a manganin wire. Electric contact between non-insulated wires and a sample is provided by either spot welding (Au wires) or silver paste, in case of sufficient sample size. These wires are connected by solder or silver paste to thicker (usually 100 μm in diameter) Cu electric leads passing through the plug.

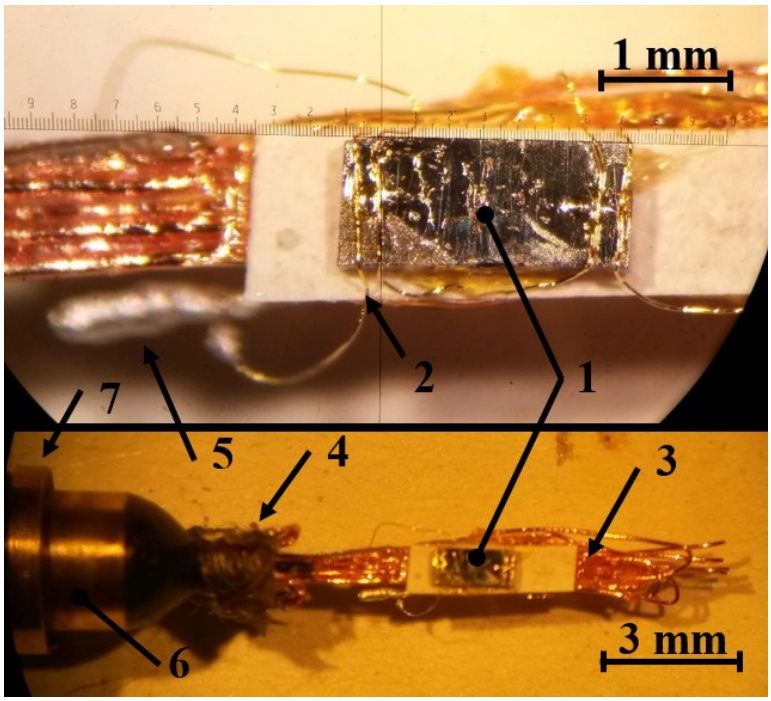

1 - Sample
2 - Gold wire
3 - Conductor leads
4 - Manganin wire
5 - Silver paste
6 - Plug
7 - CuBe sealing

Fig. 3.11: The experimental assembly of electric resistivity measurement under hydrostatic pressure.

Measurement of compressibility

The compressibility represents the response of the interatomic distances (lattice parameters) and the resulting volume to the applied external pressure and can be defined as:

$$\kappa = -\frac{1}{V} \cdot \left(\frac{dV}{dp}\right)_T , \tag{3.2}$$

for constant temperature. The measurement of compressibility was performed using a set of strain gages installed to the clamp pressure cell. A strain gauge produced by Kyowa Electronic Instruments co. (Tokyo, Japan), type KFL-05-120-C1-11 with the

length of the active part 0.5 mm was used (see in Fig. 3.12). The strain gauge consists of metallic grid which is very thin. The grid is printed on a polymer layer and covered with other polymer film on the other side. The resistance of the strain gauge is R_0 = 120.0(6) Ω at room conditions. This R_0 value linearly changes upon the change of the active-zone dimensions which can be written as:

$$r_m = G \cdot \varepsilon, \tag{3.3}$$

where $r_m = \Delta R/R_0$ is relative resistance of the strain gauge, parameter G = 2.03(3) is gauge factor at room temperature provided by the producer and $\varepsilon = \Delta l/l_0$ is relative strain [66]. The isothermal compressibility can be expressed by neglecting the higher powers of mathematical series of small magnitudes with using isothermal volume changes $\Delta V/V_0 = 3 \cdot \varepsilon$ as:

$$\kappa = -3 \cdot \frac{\varepsilon}{p}. \tag{3.4}$$

The measurement also has to consider non-neglectable additional signal originating in the pressure dependence of electric resistivity of a grid alloy. This signal can be subtracted by using reference material with known compressibility, for example Cu which has the value of compressibility κ_{Cu} = 0.0073 GPa^{-1} [20]. Afterwards, the strain of the sample ε_s can be written as:

$$\varepsilon_s(p) = \varepsilon_{R,tab}(p) + \frac{1}{G}\left[r_{m,s}(p) - r_{m,R}(p)\right], \tag{3.5}$$

where the $\varepsilon_{R,tab}(p)$ is strain derived from the tabulated data of compressibility by using Equation 3.4, the $r_{m,s}(p)$ and $r_{m,R}(p)$ are measured relative resistivity of sample and reference material, respectively. The resulting compressibility of the sample is determined by a slope of the pressure dependence of the sample strain $\varepsilon_s(p)$ according to Equation 3.4.

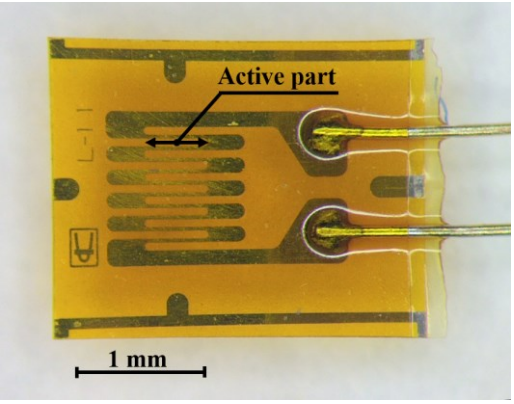

Fig. 3.12: The strain gauge with marked active part.

3.4.3. Bridgman anvil pressure cell

The electric resistivity measurements have also been performed with using Bridgman anvil pressure cell (BAC) designed in Prof. Onuki laboratory, Osaka University, Japan

see in Figure 3.13. Liquid transmitting pressure medium Daphne 7373 for this BAC was used to guarantee hydrostatic pressure. The pressure is determined by pressure dependence of the temperature of superconducting transition of Pb which was used as a pure element with 4N purity [67].

Our used BAC has unusual design possessing a special hole in the bottom anvil for bringing the leads into the sample space with dimension of Ø 1.5x0.3 mm^3. The hole has a conic shape on the side of the sample space which is filled by a cone and fixed by an epoxy glue (Stycast 2850FT). The anvils are made of tungsten carbide and the cone is made of the MP35N alloy or of a ceramic. For delimitation of the sample space a two-part gasket is used. The gasket is plate-like shape consisting of two coaxial parts. It is made of CuBe (inner part) and harder MP35N alloy (the outer part). The main body of the BAC is also made of MP35N alloy and the whole setup allows the load of the BAC up to ~7 ton. The resulting pressure in maximum load is approximately 6 GPa. This BAC is designed to be compatible with PPMS device. The technical drawing of the used BAC is shown in Figure. 3.14.

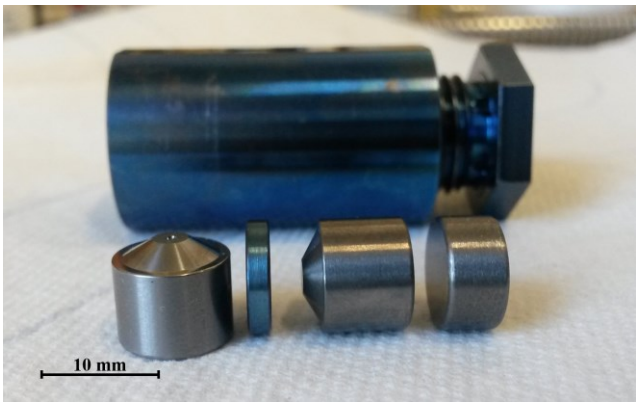

Fig. 3.13: The Bridgman anvil cell for measurements of transport properties.

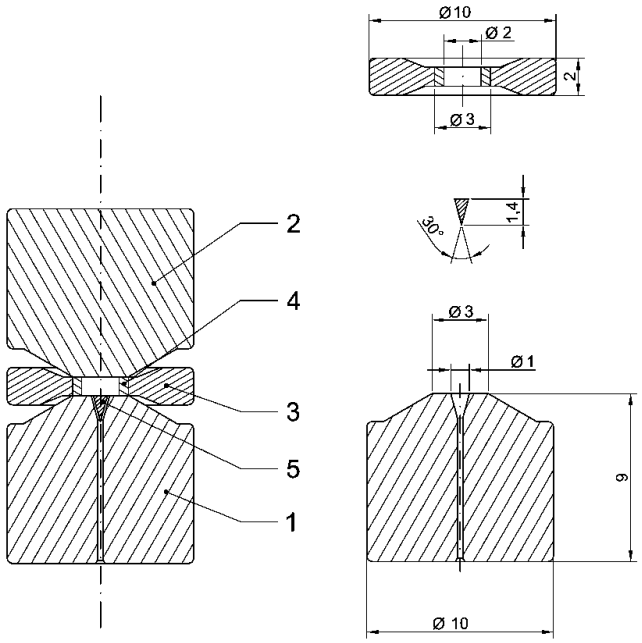

Fig. 3.14: The arrangement of BAC in technical drawing: 1) the bottom anvil with hole, 2) the upper anvil, 3) the outer part of the gasket, 4) the inner part of the gasket, 5) the cone.

3.5. Neutron diffraction

Neutron diffraction is a microscopic experimental method which uses scattering of neutrons inside the studied material. The physical properties of neutrons bring new possibilities for experimental view into materials. Advantage of neutrons is their electrical neutrality. Neutrons thus scatter directly on the nuclei of the studied compound. It also leads to long penetration depth of order of centimeters, contrary to charged particles or X-ray beam with penetration depth of micrometers. Other difference which originates in the zero electric charge of neutrons is no systematic dependence of atomic form factor on the mass number. It makes neutrons a unique isotope-sensitive probe. In contrast to x-rays, where the atomic form factor increases systematically with increasing atomic number. Aside of the interaction with nuclei and thus observation of the crystal structure, the neutrons possessing its own spin interacts also with the magnetic moments. It allows us to study also the magnetic structure.

Another characterization of the neutrons is their wavelength (de Broglie). For investigation of solid compounds so called thermal neutrons are the most frequently used due to their wavelength which is close to the interatomic distances in the matter.

3.5.1. Nuclear and magnetic neutron scattering

Generally, the interaction of neutrons with the solid materials is either elastic or inelastic. For elastic scattering the initial wavevector $\boldsymbol{k}_i$ (destined to a sample) and final wavevector $\boldsymbol{k}_f$ (coming from a sample) have the same energy. Conversely, change of the energies leads to inelastic scattering. This thesis contains data from elastic scattering only therefore this part is focused on elastic neutron scattering.

First, scattering vector is defined as a difference of $\boldsymbol{k}_i$ and $\boldsymbol{k}_f$ wavevectors and it is marked as $\boldsymbol{Q}$. Scattering process itself can be described by a double differential cross-section expressed with using Fermi's Golden Rule as:

$$\frac{\mathrm{d}^2\sigma}{\mathrm{d}\Omega\mathrm{d}E}(\boldsymbol{Q}) = \frac{|\boldsymbol{k}_f|}{|\boldsymbol{k}_i|}\left(\frac{m_n}{2\pi\hbar^2}\right)^2 \sum_{\lambda,\sigma}\left|\langle \boldsymbol{k}_f\sigma_f\lambda_f|V(\boldsymbol{Q})|\boldsymbol{k}_i\sigma_i\lambda_i\rangle\right|^2 \delta\left(E_f - E_f - E_{trans}\right), \tag{3.6}$$

where the double differential cross-section is over angle dΩ and energies dE. The m_n is the mass of neutron, the sum is over all λ_i initial states, σ_i initial spin-states of neutrons and λ_f final states, σ_i spin-states. The right side expresses conservation of energy where delta function allows transfer of energy E_{trans}. For elastic neutron scattering initial energy E_i is the same as final energy E_f and no E_{trans}. The $V(\boldsymbol{Q})$ means Fourier transformation of interaction potential $V(\boldsymbol{r})$ both the nuclear and magnetic contribution.

Nuclear neutron scattering

Nuclear neutron scattering is fingerprint of neutron interactions with nuclei via strong nuclear force. This interaction happens at positions of nuclei and nuclear interaction potential is described as:

$$V_{\mathrm{N}}(\boldsymbol{r}) = \frac{2\pi\hbar^2}{m_n}\sum_i b_i \delta(\boldsymbol{r} - \boldsymbol{r}_i), \tag{3.7}$$

where b_i is the scattering length of the respective atomic nucleus. In case of unpolarized neutron scattering, the differential cross-section Equation (3.6) with nuclear interaction potential (Eq. 3.7) can be decomposed to coherent and incoherent terms. The deeper view into coherent and incoherent terms brings the knowledge that incoherent terms don't lead to interference but it increases the background, only [68]. Assuming elastic scattering, the interference occurs from scattered neutrons on periodic planes in the crystal. The Bragg peaks are observed at the positions were the scattering vector $\boldsymbol{Q}$ is perpendicular to the crystal planes (denote *h,k,l* – Miller indices) and equal to the reciprocal lattice vector $\boldsymbol{q}$. Nuclear structure factor carries the whole information about a structure of the unit cell of studied crystal and can be written as:

$$F_{\mathrm{N}}(\boldsymbol{Q}) = \sum_j b_j e^{i\boldsymbol{Q}\cdot\boldsymbol{r}_j}, \tag{3.8}$$

where the sum is over all nuclei in the unit cell with position $\boldsymbol{r}_j$. The cross-section (3.6) can be rewritten:

$$\left(\frac{d^2\sigma}{d\Omega \mathrm{d}E}(\boldsymbol{Q})\right)_{\mathrm{coh,elas}} = \frac{(2\pi)^2}{V_0}\sum_{\boldsymbol{q}}|F_{\mathrm{N}}(\boldsymbol{Q})|^2\delta(\boldsymbol{Q}-\boldsymbol{q})\delta(E). \tag{3.9}$$

The equation of cross-section is proportional to measured intensity $I(\boldsymbol{Q})$ of Bragg peaks and therefore can be written from Equation (3.9) through relation:

$$I(\boldsymbol{Q}) \sim |F_{\mathrm{N}}(\boldsymbol{Q})|^2. \tag{3.10}$$

Magnetic neutron scattering

Neutrons carry magnetic moment which allows that neutrons interact with the magnetic fields, through the dipole-dipole interaction, which origins from magnetic moments of the measured sample. The Fourier transformation of magnetic interaction potential can be written as:

$$V_{\mathrm{M}}(\boldsymbol{Q}) = -\boldsymbol{\mu}_{\mathrm{n}} \cdot \boldsymbol{B}(\boldsymbol{Q}) = -\mu_0 \boldsymbol{\mu}_{\mathrm{n}} \boldsymbol{M}_{\perp}(\boldsymbol{Q}), \tag{3.11}$$

where $\boldsymbol{\mu}_{\mathrm{n}}$ is neutron magnetic dipole moment, $\boldsymbol{B}$ is magnetic field, μ_0 represents magnetic constant and $\boldsymbol{M}_{\perp}(\boldsymbol{Q})$ is a sample magnetization which is perpendicular to the scattering vector. The cross-section formula (3.6) for magnetic scattering can be written with using Equation (3.11) as:

$$\left(\frac{\mathrm{d}^2\sigma}{\mathrm{d}\Omega \mathrm{d}E}(\boldsymbol{Q})\right)_{\mathrm{mag,elas}} = \frac{(2\pi)^3}{V_{0\mathrm{m}}}\left(\frac{\gamma r_0}{2}\right)^2 \sum_{\boldsymbol{q}_{\mathrm{M}}}|F_{\mathrm{M}}(\boldsymbol{Q})|^2\delta(\boldsymbol{Q}-\boldsymbol{q}_{\mathrm{M}})\delta(E), \tag{3.12}$$

where the variables have similar meaning as in the Equation (3.9) but now for magnetic scattering: $V_{0\mathrm{m}}$ – volume of magnetic unit cell, $\boldsymbol{q}_{\mathrm{M}}$ – magnetic reciprocal vector, $F_{\mathrm{M}}(\boldsymbol{Q})$ – magnetic structural factor. Similar as for nuclear scattering the intensity of observed diffraction (magnetic) peaks follow the same relation as (3.10) but instead of $|F_{\mathrm{N}}(\boldsymbol{Q})|^2$ is $|F_{\mathrm{M}}(\boldsymbol{Q})|^2$.

4. Results and discussion

4.1. $UIrSi_3$

4.1.1. Introduction and previous results

U-based intermetallics are known mainly for their properties originating from the 5f-electron wave functions. 5f-electrons are more distant from the core than 4f-electrons and allow for interaction with other 5f-electrons from nearest-neighbor U atoms or with other electrons. In case of direct overlap 5f-wave functions of nearest-neighbor U atoms, the overlap prevents creation of a localized 5f-electron magnetic moment. The distance of the nearest-neighbor U atoms, needed for creation of a 5f- moment, is larger than the Hill limit (340-360 pm) [21]. This is connected with the itinerant character of the 5f-electrons due to a partly filled 5f-band. Consequently, the U magnetic moment is often found reduced in comparison with the free-ion U moments of U^{4+} or U^{3+}. The U 5f-electrons carry a large orbital magnetic moment which in the crystal lattice usually gives rise to a huge magnetocrystalline anisotropy. The orientation of the U moments is forced to be perpendicular to the planes or chains created by strong U-U bonding [12]. Another possibility is that a ligand atom is positioned between two U atoms and 5f-states hybridize with electronic states of the ligand atom. In this case, in contrast with direct overlap of 5f-wave functions which gives rise to direct exchange interaction, there is indirect exchange interaction mediated by the ligand atom.

In the last two decades, the study of intermetallic compounds crystallizing in a non-centrosymmetric crystal structure has been impressive. The popularity of these compounds, especially RTX_3 compounds, is associated with the observation of unconventional superconductivity, high critical fields, vibron states, quantum critical point, etc. [5-11]. The connecting attribute of these intermetallic compounds are the 4f-electrons in lanthanide compounds. On the other hand, only two U compounds crystalizing in the tetragonal non-centrosymmetric crystal structure, $UIrSi_3$ and $UNiGa_3$, are reported in literature. Both compounds have been studied as polycrystalline samples exhibiting antiferromagnetic (AFM) order below 42 K ($UIrSi_3$) [17] and 39 K ($UNiGa_3$) [18], respectively. The polycrystalline samples show the presence of a metamagnetic transition (MT) at a field of 5.6 T at 30 K ($UIrSi_3$) and at 7.6 T at 4.2 K ($UNiGa_3$) [17, 18].

In this part of the thesis, results on single-crystalline $UIrSi_3$ are presented which demonstrate a MT in this strongly anisotropic material. The measurements confirm AFM order below the Néel temperature $T_N = 41.7$ K and strong anisotropic response to magnetic field. This strong uniaxial anisotropy in antiferromagnet creates similarities with the Ising antiferromagnet [29, 69]. Application of an external magnetic field induces a MT at 2 K at a critical field $\mu_0 H_C = 7.3$ T applied along the c axis. The maximum value of the magnetization in the field-polarized PM state is about 0.66 μ_B/f.u. which is much lower than the value of the free-ion U moment. In comparison with other U intermetallic compounds, for instance with compounds with a magnetic moment of about 1 μ_B and $T_N > 40$ K, this value of H_C is much lower. At low temperatures, the MT is a first-order magnetic phase transition (FOMPT) and

shows an asymmetric field hysteresis. Increasing temperature leads to a decrease of H_C with shrinking of hysteresis which eventually vanishes at about 28 K. In the temperature interval 28 K < T < T_N, the character of the MT dramatically changes from FOMPT to a second-order magnetic phase transition (SOMPT) This change is manifested by a change of character of all measured physical properties.

Also first-principles electronic-structure calculations have been performed with focus on the magnetism of $UIrSi_3$. The calculations concern the type of anisotropy and the calculated magnitude of the anisotropy energy shows reasonable agreement with the experimental values, although the agreement depends on the calculation method used.

The compound was investigated also under hydrostatic and uniaxial pressure. The results show peculiarity in opposite pressure evolution of H_C and T_N. The T_N increases with increasing pressure suggests resulting magnifying AFM interaction in contrast with decreasing of H_C points to easier polarization of the magnetic moment into *c* axis. Large anisotropy in elasticity of the unit cell was observed from compressibility measurement demonstrate much softer *a* lattice parameter. Uniaxial pressure along *c* axis experiment provide evidence of almost no dependence on changing *c* lattice parameter imply that the magnetic properties depend on magnetoelastic coupling many along *a* axis.

Magnetic structure ground state is probably complicated and its determination is not determined yet. The propagation vector was determined as (0.1, 0.1, 0) and its field dependent has been observed.

4.1.2. Single-crystal growth and characterization

A single crystal of $UIrSi_3$ has been grown using the floating-zone melting-method. The process was started by synthesis of a stoichiometric polycrystal from high-purity elements: U (99.9%, further treated by Solid State Electrotransport [70, 15]), Ir (99.99%), and Si (99.999%). The polycrystalline ingot was prepared by arc melting in a special water-cooled Cu mold in protective Ar (6N) atmosphere. A precursor rod was prepared with approximate dimensions of 6.5 mm in diameter and 85 mm in length. For the growth process commercial four-mirror optical furnace with halogen lamps, each 1 kW (modelFZ-T-4000-VPM-PC, Crystal Systems Corp., Japan) was used. The quartz chamber with precursor in the optical furnace was first evacuated by a turbomolecular pump to 10^{-6} mbar and the precursor was passed through the hot zone (~50% for melting power) several times in order to desorb gases from the surface of the precursor. Then, the quartz chamber was quickly filled with high-purity Ar (6N). The growth process itself was performed under an Ar pressure of about 2 bar with a flow of 0.25 l/min. At the beginning of the growth, a narrow neck was created by variation of the speed of the upper and bottom pulling shafts. Furthermore, the neck was extended and the pulling rate was stabilized to very low value, only 0.5 mm/h, without rotation. This process provided a large single crystal (verified by the Laue method, see Fig. 4.1) of cylindrical shape with a diameter of 4 mm and a length of about 50 mm. The main part of the single crystal was annealed at 700 °C for 10 days, followed by slow cooling.

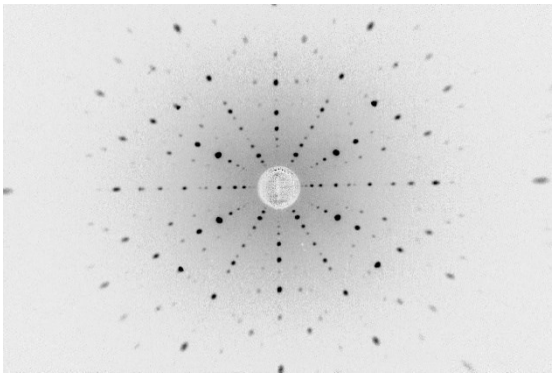

Fig. 4.1: Laue pattern of the single crystal of $UIrSi_3$ oriented along [100].

X-ray powder diffraction confirms the tetragonal $BaNiSn_3$-type non-centrosymmetric structure of $UIrSi_3$ and there is no indication of foreign phases (see Fig. 4.2). The lattice parameters a = 417.22 pm and c = 996.04 pm (see Fig. 4.3) have been determined and are in good agreement with literature [17]. A detailed verification of the stoichiometry of the composition and of possible presence of foreign phases was performed by means of scanning electron microscopy using a Tescan Mira I LMH system equipped with an energy-dispersive X-ray detector Bruker AXS. The single crystal has 1:1:3 composition and no other phases were detected.

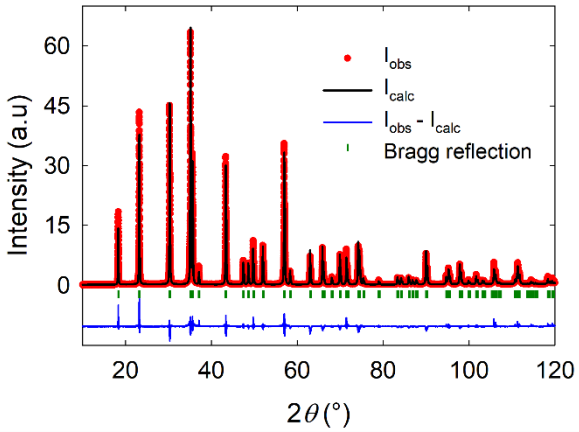

Fig. 4.2: X-ray powder diffraction diagram of the $UIrSi_3$ single crystal.

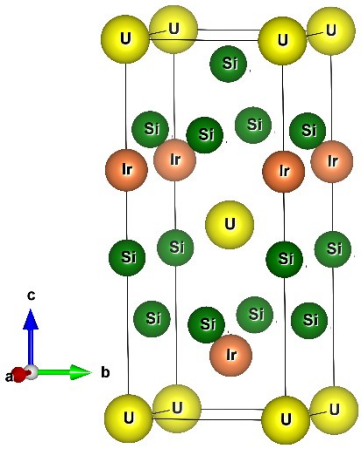

Fig. 4.3: Tetragonal non-centrosymmetric structure of $UIrSi_3$.

4.1.3. Characteristic properties of the $UIrSi_3$ single crystal

The temperature dependence of the specific heat C_p(T) of the $UIrSi_3$ single crystal exhibits an anomaly at 41.7 K (see Fig. 4.4). The anomaly has a lambda shape which is characteristic for the second-order phase transition. The position of the anomaly is in good agreement with the Néel temperature T_N reported for a polycrystalline sample of this compound [17]. Measurement of the specific heat allows making an estimate of 0.14Rln2 for the magnetic entropy associated with the AFM transition. This value is very low which can be attributed to the itinerant character of the U-magnetism. Furthermore, extrapolation of C_p/T vs T^2 (inset of Fig. 4.4) at low temperatures

($T < 4$ K) provides a value of the Sommerfeld coefficient $\gamma = 31$ mJmol^{-1}K^{-2} which is low in comparison with other U intermetallics.

Measurements of the temperature dependence of the electric resistivity $\rho(T)$ of $UIrSi_3$ with current applied along a axis ($\rho_{[100]}$) and c axis ($\rho_{[001]}$) reveal large anisotropy which may indicate an anisotropic Fermi surface (FS) of $UIrSi_3$. For both current directions, Figure 4.5 shows a gradual tendency of saturation of the resistivity with increasing temperature above T_N. The saturation is much more pronounced for the higher resistivity $\rho_{[001]}(T)$. Similar behavior in transition metals is connected with a narrow d-electron band crossing the Fermi level (E_F) and has been explained by Mott [71] and Jones [72] in terms of an s-d scattering mechanism. Tentatively, we suppose for U intermetallics a scattering mechanism analogue to the s-d scattering mechanism for transition metals. The characteristic behavior of U intermetallics is caused by the narrow 5f-electron band (for transition metals, this is the d-electron band) which crosses E_F. Analog to s-d scattering, there will be s-f scattering.

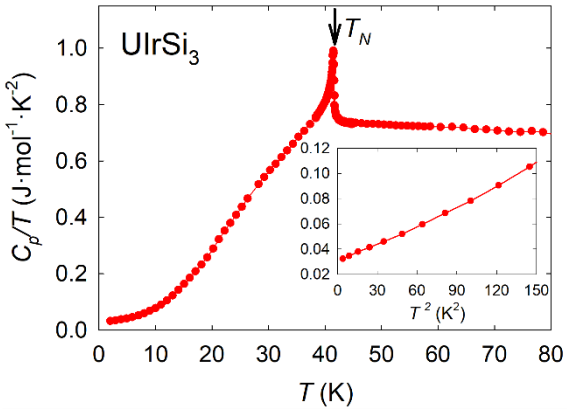

Fig. 4.4: Temperature dependence of the specific heat (in C_p/T representation) of $UIrSi_3$ in the temperature range 2-80 K. The inset shows C_p/T vs T^2 at low temperatures.

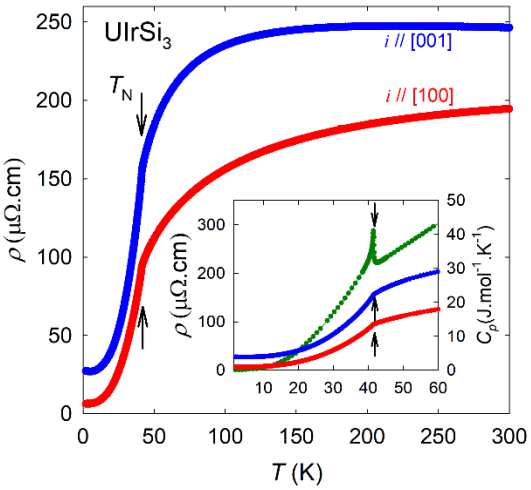

Fig. 4.5: Temperature dependence of the electric resistivity of $UIrSi_3$ for current applied along the [001] and [100] directions. The inset shows low-temperature details of the resistivity, together with the corresponding specific-heat data (green dots).

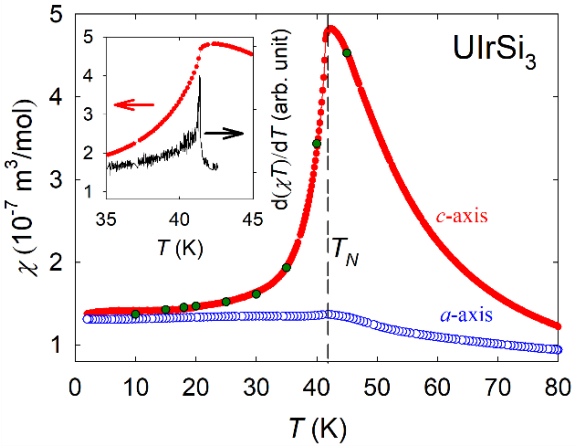

Fig. 4.6: Temperature dependence of the magnetic susceptibility (χ vs T) of $UIrSi_3$. The filled red circles represent measurements in a magnetic field ($\mu_0 H = 0.1$ T) applied along the c-axis and the empty blue circles in a field ($\mu_0 H = 0.5$ T) along the a-axis. The broken line marks T_N (= 41.7 K) determined from specific-heat data whereas the maximum of χ is at higher temperature (42.3 K). The inset shows the χ curve and $\partial(\chi T)/\partial T$ vs T (black line) which exhibits a maximum at 41.4 K. The dark green points correspond to values of the susceptibility derived from magnetic isotherms measured at a number of fixed temperatures.

As indicated by the specific-heat data (see inset of Fig. 4.5), the AFM phase transition is represented in the electric resistivity as a change of curvature from positive to negative during heating The residual resistivity ratio is 14 for $\rho_{[001]}(T)$ and, a much larger value, 34 for $\rho_{[100]}(T)$.

The AFM phase transition is also manifested in the temperature dependence of the magnetic susceptibility χ (= M/H; M: magnetization; H: magnetic field) displayed in a χ vs T plot in Figure 4.6. The maximum of χ vs T at 42.3 K does not coincide with the somewhat lower T_N value of 41.7 K determined by specific heat measurements. This is because, for exact determination of the AFM transition temperature from χ the genuine thermodynamic variable χT has to be used. The maximum of the $\partial(\chi T)/\partial T$ vs T curve corresponds to T_N (see inset of Fig. 4.6) [73, 74]. In this way, for T_N = 41.4 K s found. For magnetic field applied along the c axis, χ is much larger than along the a axis which shows that the c axis is the easier-magnetization axis.

Figure 4.7 displays the temperature dependences of the inverse magnetic susceptibility in the PM region which demonstrates strong magnetocrystalline anisotropy, as present in most magnetic U compounds. Magnetocrystalline anisotropy in the PM region is a common feature in these compounds and can be compared through differences of the Weiss temperatures (paramagnetic Curie temperatures) θ_p that can be obtained from fits the so-called modified Curie-Weiss (MCW) law:

$$\chi(T) = \frac{C}{T-\theta_P} + \chi_0, \qquad (4.1)$$

where C is the Curie constant from which the value of effective magnetic moment μ_{eff} can be derived (see Eq. 2.6), T is the temperature and χ_0 is a temperature-independent susceptibility, including diamagnetic and Pauli-paramagnetic contributions.

The susceptibility has been measured in temperature interval from 2 to 600 K but in order to avoid the influence of correlations arising from the magnetic ordering the fit has been performed for temperatures above 60 K.

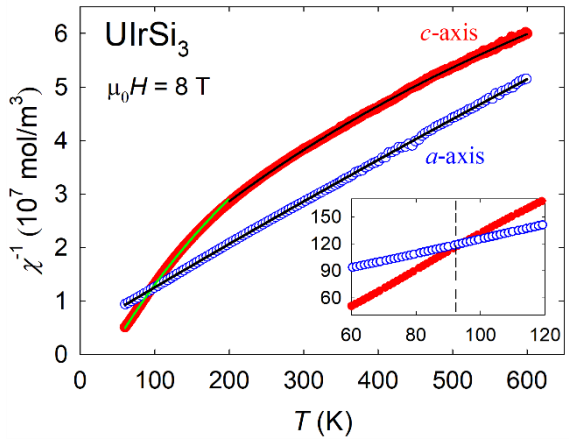

Fig. 4.7: Temperature dependence of the inverse magnetic susceptibility. The full red circles represent measurements with the magnetic field applied along the *c* axis and the empty blue circles measurements along the *a*-axis. Both measurements have been performed at $\mu_0 H = 8$ T. The black lines represent fits to the MCW law for *a* axis 60-300 K, *c* axis 200-600 K and green line for temperatures 60-200 K. The inset shows in detail the crossing of the *a*-axis and the *c*-axis results in χ^{-1} vs *T*.

The χ values measured with the magnetic field applied along the *a*-axis follow a MCW law in the temperature interval 60-600 K, see Fig. 4.7. The fit to equation 4.1 gives $\theta_p = -51$ K which is comparable with T_N (41.7 K) as expected for simple antiferromagnets entirely governed by an AFM interaction. Assuming that Ir and Si contribute negligibly to μ_{eff}, the MCW fit gives a value of 2.7 μ_B for the effective moment of U (Table A). This is much lower value than the values for the free U^{3+} and U^{4+} ions (3.62 μ_B and 3.58 μ_B, respectively) points to the itinerant character of the magnetism. The χ data measured with the magnetic field applied along the *c*-axis do not follow a MCW law in the whole temperature interval 60-600 K. To get values for comparison and insight into the complex situation, the data have been separated into two temperature intervals 60-200 K (lower temperatures) and 200-600 K (higher temperatures) and fitted separately. The obtained fitting parameters θ_p, μ_{eff} and χ_0 are collected in Table A. The separation of the fitted interval is done due to impossibility to fit the whole temperature interval and we would to point how large are the differences.

The inset in Figure 4.7 clearly shows that the crossing (~93 K) of the *a*- and *c*-axis reciprocal-susceptibility curves is mainly caused by deviation of the *c*-axis susceptibility. This peculiar behavior may reflect competition between AFM and ferromagnetic (FM) interactions in the low-temperature region. It might be explanation for large differences in particular MCW fits at *c* axis (see in Table A) mainly opposite sight of θ_p in low temperatures. It should be mentioned that a qualitatively similar situation (crossing temperature dependences of $1/\chi_a$ and $1/\chi_c$) is observed in the case of UIr_2Si_2 [75]. UIr_2Si_2 crystallizes in the tetragonal $CaBe_2Ge_2$-type of structure where U ions are in a non-centrosymmetric surrounding of ligands, similar to the $UIrSi_3$ case. So far, there is no reasonable explanation for this crossing.

Table A: MCW fits of the magnetic susceptibility, measured with field applied along the *a*-axis and the *c*-axis.

H //	fitting range (K)	μ_{eff} (μ_B/U)	Θ_p (K)	χ_0 (10^{-9} m^3/mol)
a	60 – 600	2.7	-51	1.3
c	200 – 600	2.0	-24	6.5
c	60 – 200	1.6	38	8.3

The measurement of the magnetization curve at 2 K (see Fig. 4.8) with magnetic field applied along the *c* and the *a* axis clearly demonstrates the strong magnetocrystalline anisotropy of $UIrSi_3$. The easier-magnetization axis is evidently the *c* axis and the magnetization of only 0.2 μ_B/f.u. at 14 T along the *a* axis shows this axis to be like the hard-magnetization axis. Up to 7 T, the $M(H)$ dependence is almost the same for both field directions. Above 7 T is a sharp MT is observed with a resulting saturation magnetization of 0.64 μ_B.

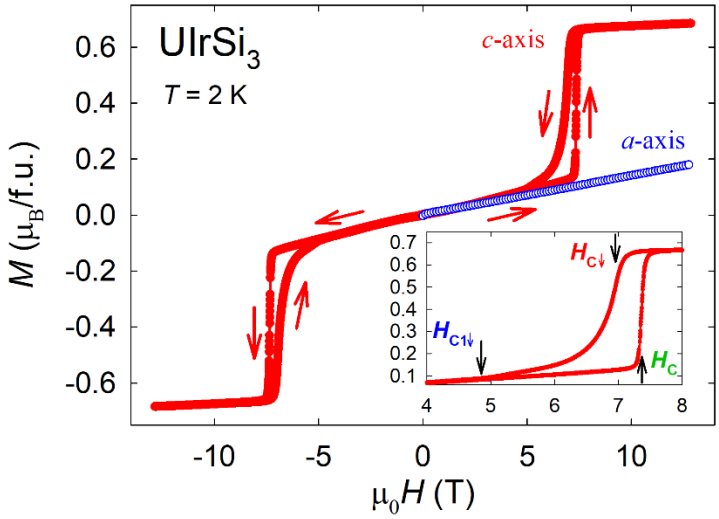

Fig. 4.8: Field dependence of the magnetization measured at 2 K with the field along the *c*-axis (full red symbols) and along the *a*-axis (empty blue symbols). The arrows show the direction of the field sweep. The inset displays details for the magnetic field applied along the *c* axis.

4.1.3. First-principles calculations

First-principles calculations based on density functional theory (DFT) have been performed to obtain the spin and orbital U magnetic moments, the magnetocrystalline anisotropy energy, the easy-magnetization axis, the equilibrium volume and the stability of the AFM structure. The Dirac-Kohn-Sham equations for a FM configuration give the values M_S = -1.42 μ_B and M_L = 1.87 μ_B which lead to a total magnetic moment M = 0.45 μ_B, much smaller than experimentally observed. The calculations have been extended about polarization correction by full potential local orbitals (FPLO) code (using the division 24×24×24 for both the *a* and *c* axis, corresponding to 1764 and 3756 irreducible *k* points in the Brillouin zone) [76]. This

provides a total magnetic moment of 1.78 μ_B which overestimates the experimental value. Therefore, another method has been used which realizes relativistic conditions. The local spin density approximation (LSDA) method with adjustable Hubbard parameter U [77] gives very good agreement with the experimental magnetic moment through M_S = -1.20 μ_B, M_L = 1.86 μ_B and U = 0.28 eV. These results (see Table B) show that the 5f-electrons in $UIrSi_3$ are moderately correlated.

Table B. Spin moment μ_S, orbital moment μ_L and total magnetic moment μ, calculated by different methods, and the experimental value.

Method	μ_S (μ_B)	μ_L (μ_B)	μ (μ_B)
Dirac	-1.42	1.87	0.45
Dirac + OPC	-1.99	3.77	1.78
LSDA + U + SOC	-1.20	1.86	0.66
Experiment			0.64

Calculations of the total energies of the FM and simple AFM (up-down-up-down…) structures were done using augmented spherical waves (ASW) in the LSDA method which include spin-orbit coupling [78, 79]. The AFM structure was found in the form of two FM U layers in the *a*-*b* plane with magnetic moments in opposite direction and parallel to the easy *c*-axis direction. This AFM structure has 16 meV/f.u higher energy than the FM structure. The cell for the calculation has been increased along the *c* axis and another AFM structure (up-up-down-down) has been considered. The energy of this structure is smaller but the FM state energy is still preferable by 5 meV/f.u. The results are in agreement with expectation of the expected complex AFM structure in $UIrSi_3$, due to competition of AFM and FM interactions.

The calculations confirm the easy-magnetization axis to be along the *c* axis. From the total energy with the magnetic moments along the *a* and along the *c* axis, the magnetocrystalline anisotropy energy (MAE) is found to be 4.57 meV. The experimental value of the MAE can be estimated from extrapolation of the $M(H)$ curves measured in fields along the *a* and *c* axis. The $M(H)$ curves cross at about 59 T which is smaller than the anisotropy fields of the majority of the UTX and UT_2X_2 compounds, which usually exhibit anisotropy field of about hundred tesla [12]. The U compounds UIr_2Si_2 and UPt_2Si_2, that crystallize in the $CaBe_2Ge_2$-type of structure which is similar to the $BaNiSn_3$ structure of $UIrSi_3$, have comparable anisotropy fields [75,80]. A rough estimation of the MAE of $UIrSi_3$ from the crossing of the magnetization curves gives about 1.1 meV which is in fair agreement with the calculated value.

4.1.4. Metamagnetic transition in $UIrSi_3$

The MT is clearly manifested by a rapid increase of the magnetization (see Fig. 4.8) but only upon application of a magnetic field along the *c* axis. Magnetization measurement with the field along the *a* axis gives PM response up to 14 T. The critical field H_C of the MT is determined by the first derivative (minimum) and is situated around the midpoint of the magnetization step upon increasing magnetic field. When the magnetic field is decreased, large field hysteresis is observed which is intrinsic for

a FOMPT [81]. The hysteresis is rather unusual and, as seen in Figure 4.8, asymmetric which is due to the reverse (field-sweep-down) transition which is broader and contains a wide tail at the low-magnetic side. This peculiar behavior can be tentatively explained by gradual reentry of a complex magnetic ground state of the AFM structure through the intermediate arrangement of uncompensated spin phases. In order to characterize this transition, two characteristic fields in reverse transition curve have been marked: $H_{C\downarrow}$ (determined by the minimum of the first derivative) and $H_{C1\downarrow}$ (end of the hysteresis), as indicated in Figure 4.8.

The $M(H)$ curves at selected different temperatures reveal a temperature evolution of the MT which is plotted in Figure 4.9. With increasing temperature, H_C clearly decreases and the hysteresis rapidly vanishes. The magnetization step at the MT becomes smaller with increasing temperature but above 25 K it is reduced at a higher rate. The inset in Figure 4.9 shows the temperature dependence of the hysteresis $\mu_0(H_C - H_{C1\downarrow})$ which has been fitted to the equation

$$\mu_0(H_C - H_{C1\downarrow}) = c\left(1 - \sqrt{\frac{T}{T_1}}\right). \tag{4.2}$$

This expression describes temperature dependence of the coercive field in single-domain particle systems and was applied to granular $Cu_{97}Co_3$ and $Cu_{90}Co_{10}$ alloys [82]. The fitting parameters in the case of $UIrSi_3$ are c = 3.3 and T_1 = 24 K.

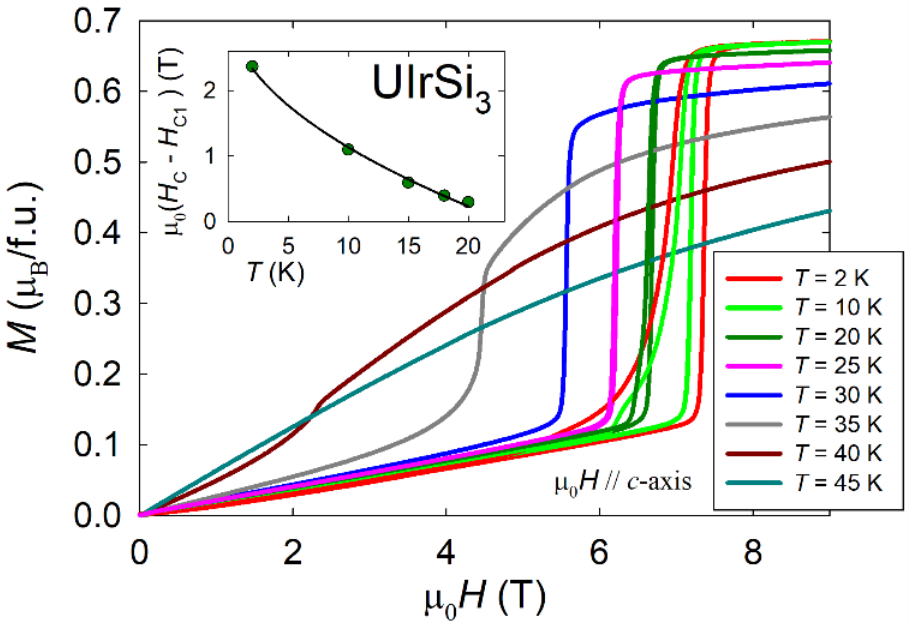

Fig. 4.9: Magnetization measured at various temperatures with the magnetic field applied along the c axis. The inset shows the temperature dependence of the field hysteresis at the MT. The solid line represents a fit to equation 4.2.

Closer inspection of the magnetization curves points to the presence of two types of $M(H)$ curves:

(i) At low temperatures up to 25 K, the $M(H)$ curves are characterized by a sharp magnetization step ΔM at H_C and field hysteresis $\mu_0(H_C - H_{C1\downarrow})$ which both decrease with increasing temperature. The field dependence is practically linear below 0.9 H_C and there is saturation above 1.1 H_C. These features are characteristic for a FOMPT.

(ii) The $M(H)$ curves above 25 K exhibit an upturn at fields below H_C followed by a cusp at H_C. This cusp is followed by gradual saturation at fields above H_C. With increasing temperature, H_C decreases, becoming zero at T_N. The decrease of H_C is accompanied by a gradually less pronounced upturn and cusp. No field hysteresis is observed. These effects characterize a SOMPT.

The change of the type of order of MT from FOMPT to SOMPT is clearly visible in the magnetic-field dependence of the specific heat which, together with the $M(H)$ curves, is shown in Figures 4.10 and 4.11.

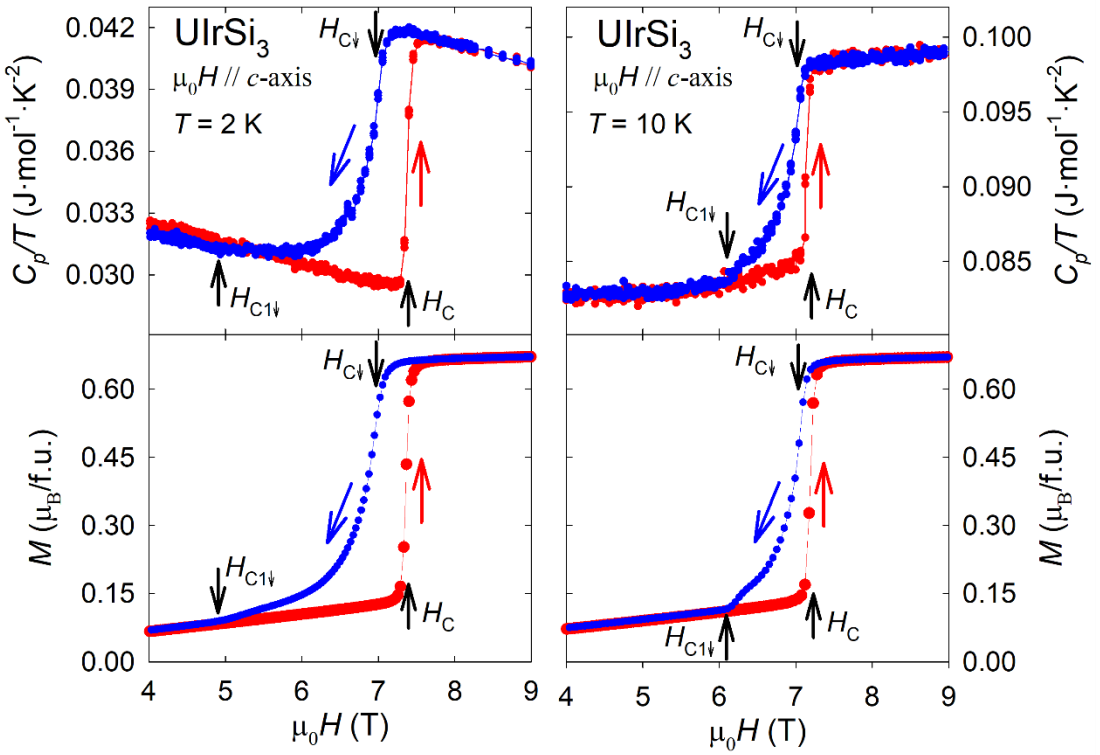

Fig. 4.10: Magnetic-field dependence of the specific heat (upper plots) and the magnetization (lower plots) of a $UIrSi_3$ single crystal (left panel at 2 K and right panel at 10 K) with the field applied along the c axis (red points – increasing field, blue points – decreasing field).

The FOMPT gives rise to a step in C_p/T at H_C which is accompanied by field hysteresis when the field is decreased, which qualitatively resembles the magnetization behavior. The sharp positive step in C_p/T at H_C reflects an increase of the density of conduction-electron states originating from Fermi-surface reconstruction at MT which

is characteristic for a magnetic-field-induced Lifshitz transition [83]. In contrast with this, the SOMPT gives rise to a λ-shape anomaly in C_p/T at H_C. At lower field, the value of C_p/T is enhanced which reflects spin-flip fluctuations that originate from the AFM state below H_C. This effect is more pronounced at temperatures approaching T_N (see Fig. 4.11).

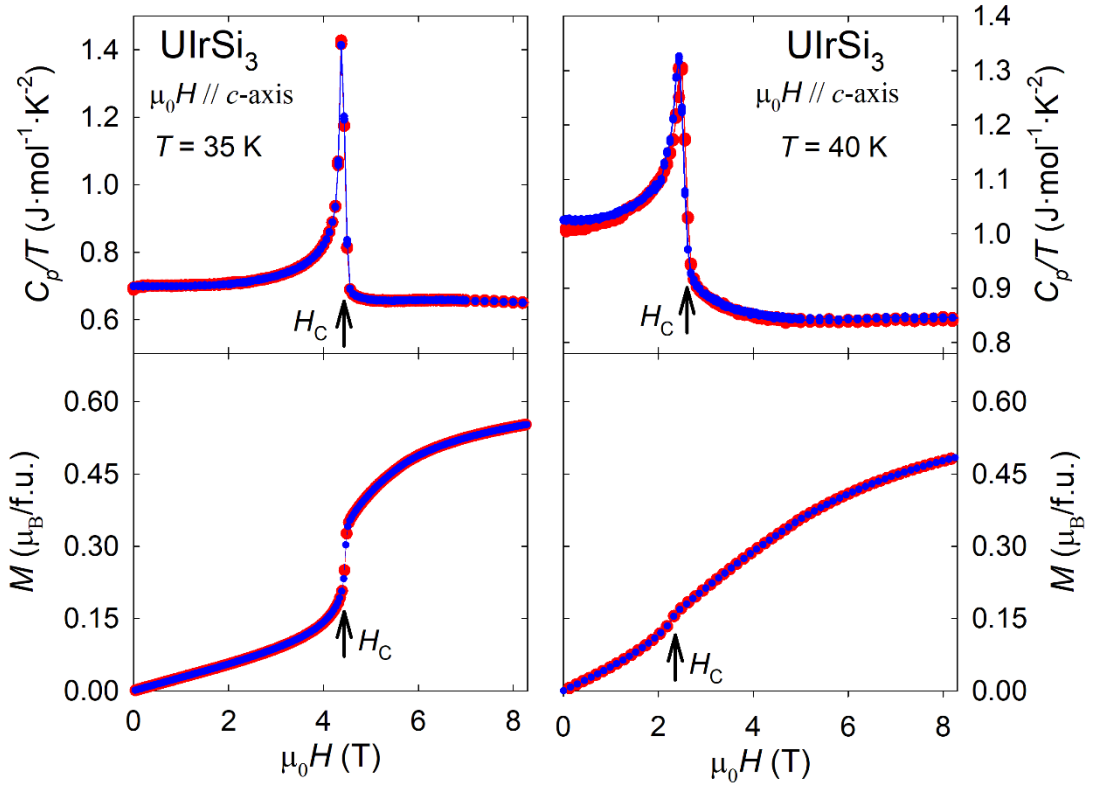

Fig. 4.11: Magnetic-field dependence of the specific heat (upper plots) and magnetization (lower plots) of a $UIrSi_3$single crystal (left panel at 35 K and right panel at 40 K) with the field applied along the c-axis (red points – increasing field, blue points – decreasing field).

The temperature dependence of the specific heat has also been measured at increasing and decreasing temperature at constant magnetic field. The inset in Figure 4.12 shows the presence of temperature hysteresis at the transition at fields above 5.8 T which indicates emerging latent heat associated with the FOMPT. The temperature hysteresis vanishes at fields below 5.8 T. Closer inspection of Figure 4.12 reveals that the typical λ-shape anomaly is observed at the transition which points to the SOMPT and that the transition is roughly symmetric at fields above 5.8 T. The vanishing of the transition at high magnetic fields is caused by ineffective crossing of the MT border in the *H-T* diagram, which is tangential with respect to the temperature dependence. However, the transition is clearly visible in the magnetic-field dependence of the specific heat.

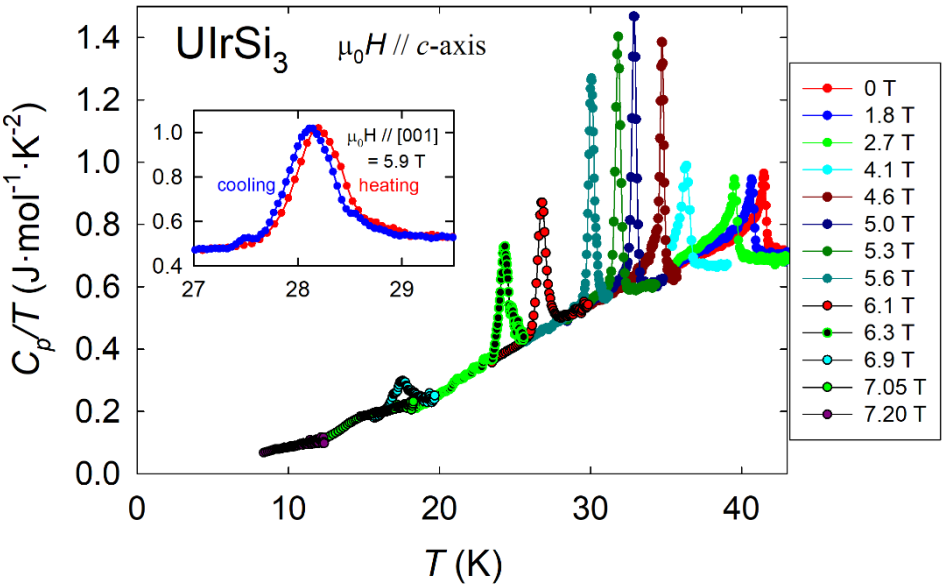

Fig. 4.12: Temperature dependence of the specific heat (C_p/T vs T) under application of various magnetic fields along the c-axis. The inset shows the presence of temperature hysteresis at 5.9 T

The measurements of magnetization and specific heat make it possible to construct the magnetic phase diagram of $UIrSi_3$ shown in Figure 4.13. The diagram shows a decrease of the critical field H_C with increasing temperature and a reduction of the magnetic hysteresis represented by the approaching of H_C by $H_{C\downarrow}$ and $H_{C1\downarrow}$ to meet finally at 28 K and 5.8 T. This point separates two parts of the magnetic phase diagram: the FOMPT below 28 K and the SOMPT above 28 K. The point separating the FOMPT and SOMPT regimes in the magnetic phase diagram is considered as a

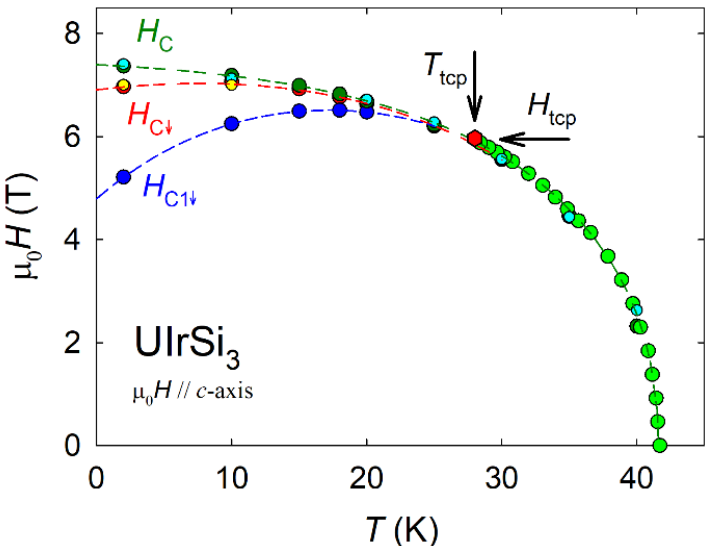

Fig. 4.13: Magnetic phase diagram of $UIrSi_3$ for magnetic field applied along the c-axis. The quantities H_c, $H_{c\downarrow}$ and $H_{c1\downarrow}$ are defined in the inset of Figure 4.8. The colors of the data points represent the origin of the data: $C_p(T)$... H_c - light green; $M(H)$ … H_c - green, $H_{c\downarrow}$ - red, $H_{c1\downarrow}$ - blue; $C_p(H)$ … H_c - cyan, $H_{c\downarrow}$ - yellow. The dashed lines are guides to the eyes. The red hexagonal point indicates the tricritical point (T_{tcp} = 28 K, $\mu_0 H_{tcp}$ = 5.8 T).

tricritical point for $UIrSi_3$ with coordinates $T_{tcp} = 28$ K, $\mu_0 H_{tcp} = 5.8$ T. This point separates three involved phases as has been found for other AFM U intermetallics in Refs [84-86]. In literature, also materials are reported without precise specification of the three involved phases [87, 88]. The prediction of tricritical point is reported by Landau in Ref. [29] for Ising Antiferromagnets. The $UIrSi_3$ possess strong uniaxial anisotropy is being very similar to Ising Antiferromagnet and it could partially explained presence of tricritical point.

4.1.5. Magnetotransport properties at the metamagnetic transition

The electrical-transport measurement is a powerful tool to study the conduction-electron interactions with unpaired electrons carrying magnetic moments. The large sensitivity of electric resistivity and Hall resistivity for magnetic moments makes these properties important probes for studying the collective magnetic behavior in metallic materials.

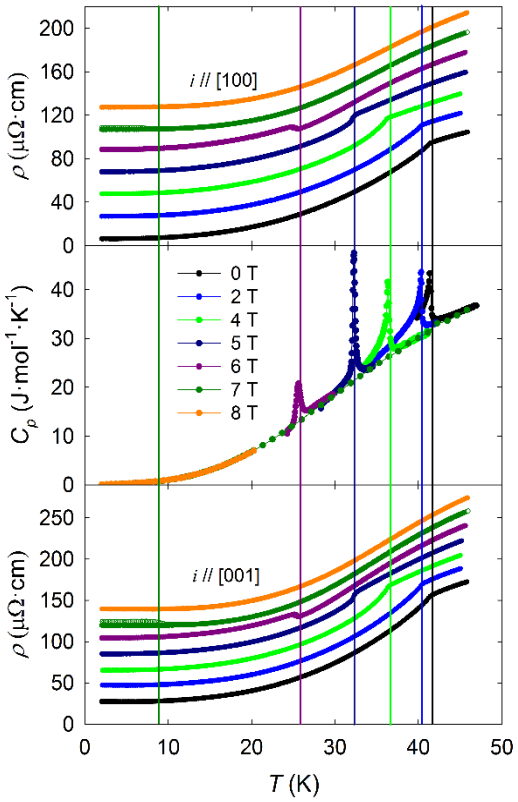

Fig. 4.14: Temperature dependence of the electric resistivities $\rho_{[001]}(T)$ (bottom panel) and $\rho_{[100]}(T)$ (top panel) and the specific heat (middle panel) measured at several magnetic fields applied along the c axis. For clarity, the $\rho(T)$ curves measured at different fields have been shifted by 20 μΩ·cm on the vertical scale.

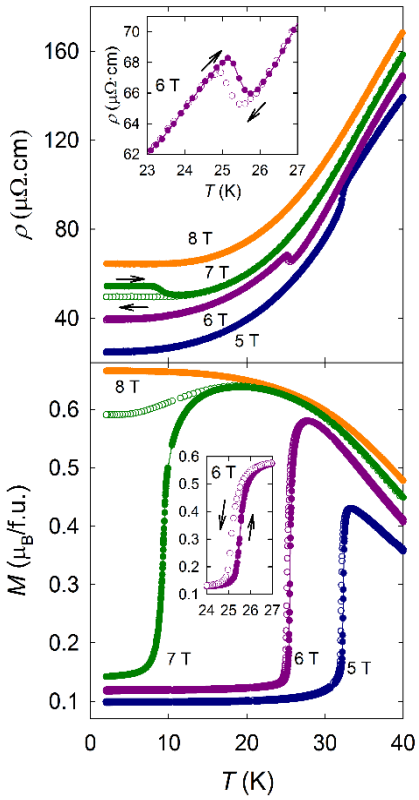

Fig. 4.15: Temperature dependence of the electric resistivity $\rho_{[001]}(T)$ (top panel) and the magnetization (lower panel) measured at several magnetic fields applied along the c axis. The insets show details of the T_N-related anomaly for $\rho_{[001]}(T)$ and $M(T)$ at 6 T. For clarity, the $\rho(T)$ curves at different fields have been shifted by 15 μΩ·cm on the vertical scale.

The temperature dependence of the electric resistivities $\rho_{[001]}(T)$ and $\rho_{[100]}(T)$ in magnetic field applied along the *c* axis was measured in field-cooled (FC) and zero-field-cooled (ZFC) mode and with increasing and decreasing temperature. Relevant differences between these measurements are described below. The results exhibit a shift of the T_N-related anomaly to lower temperature with increasing field, which is in agreement with the specific-heat measurements. Figure 4.14 shows that, for both the $\rho_{[001]}(T)$ and the $\rho_{[100]}(T)$ dependence, the T_N-related anomaly changes with increasing magnetic field from a negative $\partial\rho/\partial T$ at zero field to a clearly positive $\Delta\rho$ step at 5 T. The transition at T_N has been determined as the maximum of $\partial\rho/\partial T$ up to 5 T and has a character which is typical for magnetic transitions. At 6 T, suddenly a negative $\Delta\rho$ step is observed at T_N. Also at 7 T, a $\Delta\rho$ step is found in the ZFC curves. At 8 T, the $\rho_{[001]}(T)$ and $\rho_{[100]}(T)$ curves are both smooth without any indication of a transition anomaly. The corresponding $\rho_{[001]}(T)$ and $M(T)$ curves measured at 6 T show the presence of temperature hysteresis, manifesting a FOMPT (see Fig. 4.15). On the other hand, the $\rho_{[001]}(T)$ and $M(T)$ curves measured at 5 T show no hysteresis at T_N. The bifurcation of the $\rho_{[001]}(T)$ and $M(T)$ curves at 7 T in the ZFC and FC measurements is caused by the large field hysteresis shown in Figure. 4.9.

For studying the MT, also the Hall resistivity ρ_H has been measured with the field applied along the *c* axis (Fig. 4.16). At 1 T, T_N is manifested in ρ_H by a change of $\partial\rho_H/\partial T$. With increasing field, this change of $\partial\rho_H/\partial T$ shifts to lower temperatures until, at 5 T, and a clear negative $\Delta\rho_H$ step has developed. This development is analog to the normal-resistivity case and the transition temperatures determined by the minimum of $\partial\rho_H/\partial T$ correspond to the T_N values determined by the specific heat. In Figure 4.16, the Hall-resistivity and magnetization measurements are compared, showing nice coincidence of the T_N-related anomalies in both physical quantities. The $\rho_H(T)$ measurements in fields up to 5 T and in higher fields exhibit the same change of the T_N-related anomaly as the resistivity measurements. $\rho_H(T)$ also exhibits a dramatic change of the T_N-related anomaly in fields above 5 T where a sudden positive $\Delta\rho_H$ step at T_N and temperature hysteresis are observed. The coincident changes between 5 T and 6 T in the $\rho(T)$, $\rho_H(T)$ and $M(T)$ dependencies clearly manifest a change from SOMPT to FOMPT as is also demonstrated by the specific-heat measurement where the tricritical point at $T_{tcp} = 28$ K, $\mu_0 H_{tcp} = 5.8$ T separates the SOMPT from the FOMPT.

The $\rho_H(T)$ curve at 8 T is smooth both in the resistivity and the magnetization measurements. This is because the field is sufficiently higher than $\mu_0 H_C = 7.3$ T at 2 K (see Fig. 4.8) which prevents creation of AFM ordering at sufficiently low temperature. This is the reason why the curves measured at 8 T ($\rho(T)$, $\rho_H(T)$ and $M(T)$ – see Figs. 4.14 – 4.16) are smooth and without any indication of a transition because the PM state remains preserved. At low temperatures, the magnetic moments are polarized and this is called the polarized paramagnetic (PPM) state.

The ZFC and FC curves at 7 T are evidently bifurcated (Figs. 4.41 – 4.16) in the vicinity of T_N, manifesting large hysteresis of the MT (Fig. 4.8). Closer inspection of Figure 4.8 shows that the curve at 7 T reaches a maximum value at about 20 K and then decreases about 10% upon further cooling before magnetic ordering. This suggests somehow a disturbed PPM state as the low-temperature FC state which also exhibits a clearly lower resistivity than the ZFC state. In the ZFC measurement, the AFM ordering remains, as can be seen in the $M(T)$ curves, which probably has higher resistivity than the PPM region. This can be due to truncation of the FS by energy gaps caused by different periodicities of the crystallographic and AFM order. The

temperature dependence of $\rho_H(T)$ (top panel of Fig. 4.16) exhibit broad minima which roughly coincide with the inflection points (minimum of $\partial M/\partial T$) of the magnetization. The negative values of $\rho_H(T)$ provide evidence of the ordinary Hall effect predominantly caused by conduction electrons. At low temperatures, positive values for $\rho_H(T)$ are observed at 8 T and, for ZFC, at 7 T. This indicates a large contribution of the anomalous Hall effect in the PPM state.

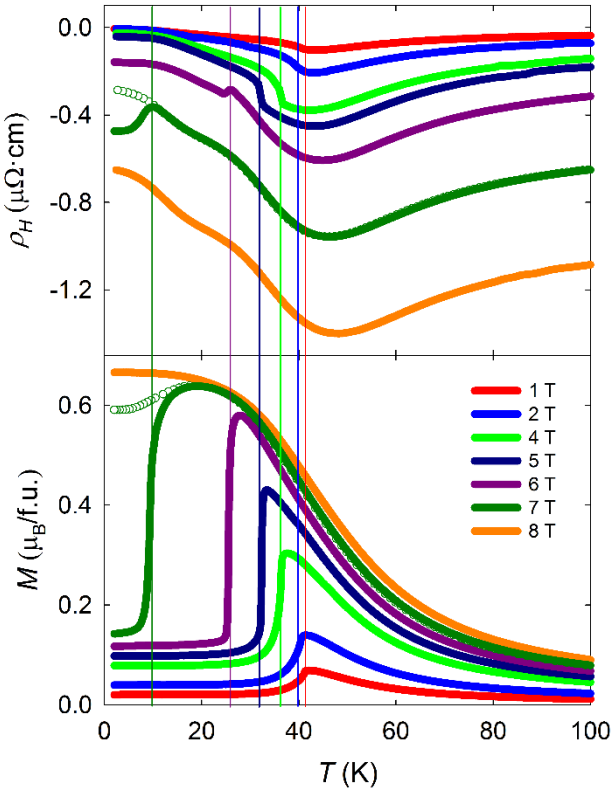

Fig. 4.16: Temperature dependences of the Hall resistivity ρ_H (top panel) and the magnetization M (bottom panel) at different magnetic fields applied along the c axis. The $\rho_H(T)$ curves measured at 6 T, 7 T and 8 T have been shifted vertically by -0.1, -0.4, -0.8 μΩ·cm, respectively. The curves at 7 T are plotted as a full line for ZFC and open symbols for FC measurement. The vertical colored lines represent T_N values determined from specific-heat measurements.

In Figure 4.17, the longitudinal magnetoresistance $\rho_{[001]}(H)$ and the transversal magnetoresistance $\rho_{[100]}(H)$ in a magnetic field along the c axis are presented. Below T_{tcp}, the MT-related anomaly manifests a FOMPT (lower panels in Fig. 4.17) and has analogous character as the magnetization curve (Fig. 4.9). At H_C, the value of $\rho(H)$ sharply drops during sweeping up the magnetic field but, when the magnetic field is swept down, the $\rho(H)$ curve shows asymmetric hysteresis of the MT. The upper panels in Figure 4.17 represent isotherms measured at $T_{tcp} < T < T_N$ where $UIrSi_3$ undergoes a field-induced SOMPT between the AFM and the PM state. The SOMPT has a dramatically different manifestation in the $\rho(H)$ curves than the FOMPT. The resistivity gradually increases with increasing magnetic field up to H_C where it has a maximum value. Further increasing the field above H_C leads to a fast decay of the resistivity. In contrast with FOMPTs, no field hysteresis is observed.

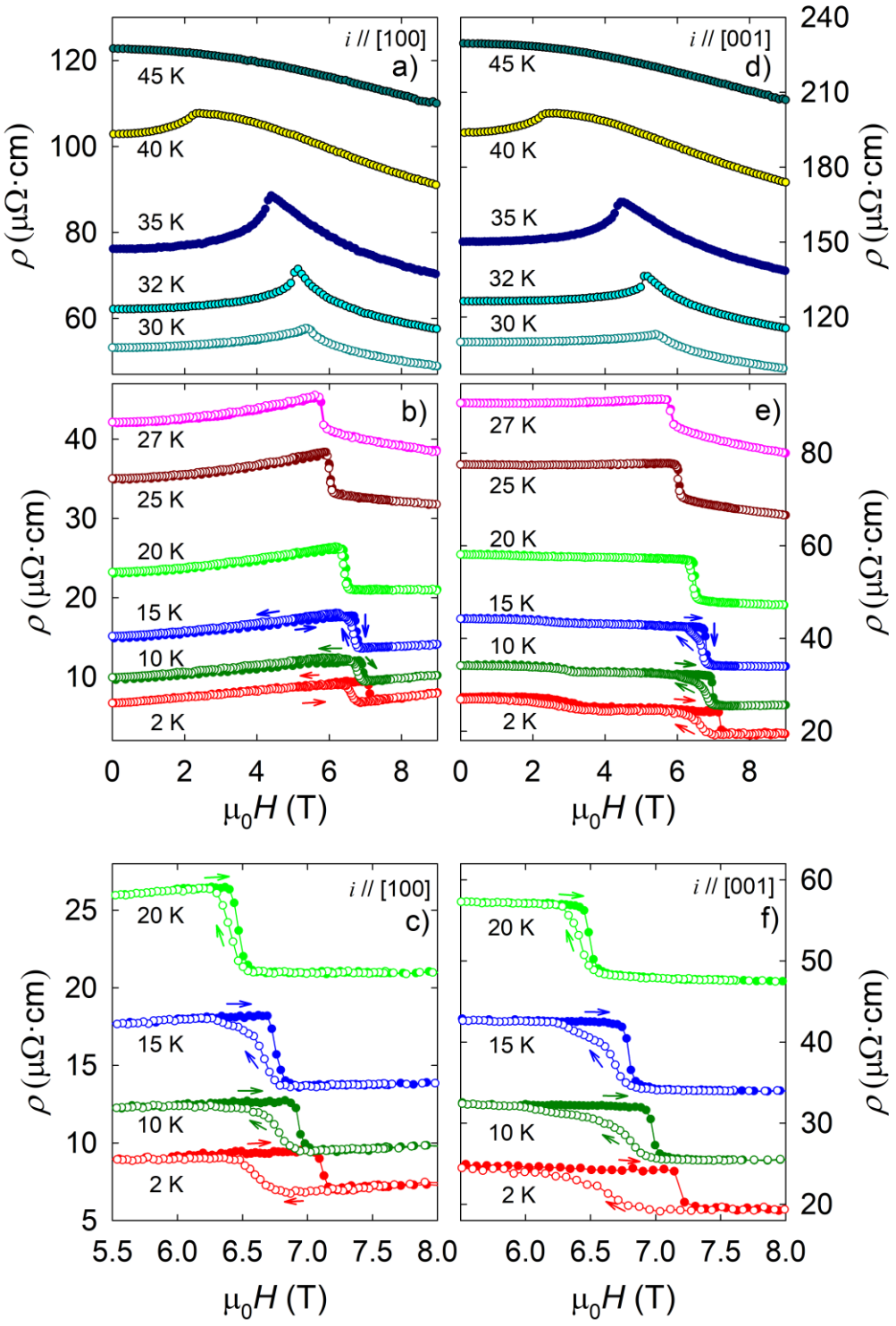

Fig. 4.17: Transversal (left panels a, b and c) and longitudinal magnetoresistance (right panels d, e and f) measured in magnetic field applied along the *c* axis. For clarity, the $\rho(H)$ curves have been shifted vertically by 2 μΩ·cm (left panels) and 6 μΩ·cm (right panels). The panels c and f show the details of the MT-related anomaly.

The correctness of the measured asymmetric hysteresis had been tested by time evolution of the electric resistivity at 2 K and 6.8 T. A small deviation of about 2% from the starting value was observed, as is shown in Figure 4.18.

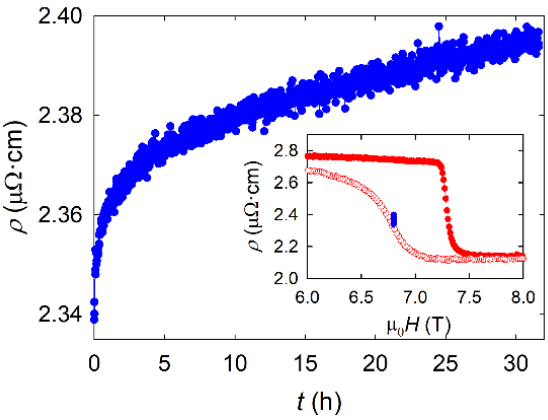

Fig. 4.18: Time evolution of the electric resistivity measured at 2 K and 6.8 T applied along the *c* axis. The inset demonstrates the relaxation at the MT-related anomaly in detail.

The field dependence of the Hall resistivity has also been measured and the isotherms are plotted in Figure 4.19. At the FOMPT below T_{tcp}, the $\rho_H(H)$ isotherms show a sharp positive $\Delta\rho_H(H)$ step manifesting H_C and asymmetric field hysteresis during field sweep down similarly as the magnetization curves. On the other hand, the $\rho_H(H)$ isotherms measured at $T_{tcp} < T < T_N$ exhibit a rounded negative $\Delta\rho_H(H)$ step without hysteresis. The curvature of the rounded negative $\Delta\rho_H(H)$ step gradually increases, efficiently smearing out the MT-related anomaly to disappearance around 40 K. Contrary to $\rho(H)$, $M(H)$ and $C_p(H)$, $\rho_H(H)$ exhibits a sharp change of the MT-related anomaly due to change from FOMPT to SOMPT. Therefore, $\rho_H(H)$ can most appropriately be used for TCP determination.

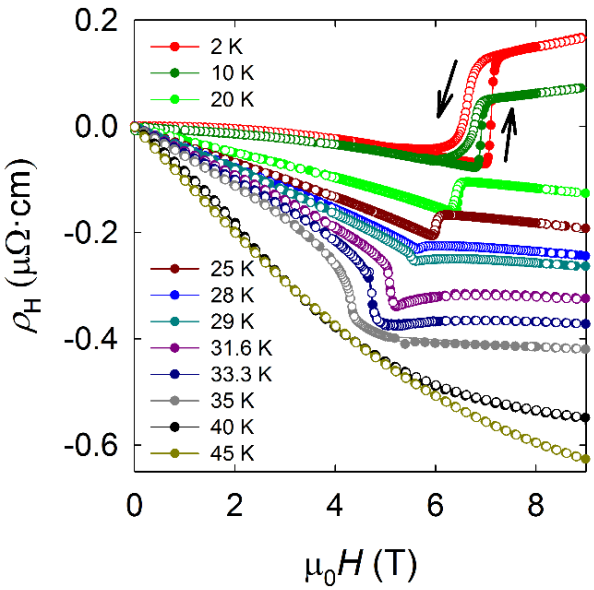

Fig. 4.19: Dependence of the Hall resistivity on a magnetic field oriented along the *c* axis at different temperatures.

A profound analysis of the $\rho_H(H)$ and $\rho_H(T)$ dependences had been performed by fitting to the empirical Equations 2.28 and 2.29 resulting from the investigation of the anomalous Hall effect in ferromagnets. Nevertheless, the fit does not mesh with

observed data in AFM or PM intervals. It is caused by lacking description of Hall resistivity for AFMs which is probably more complex than empirical formulas Equations 2.28 and 2.29 for ferromagnets.

The performed experiments reveal an evolution of the MT measured with the field along the *c* axis. The temperature dependence at 8 T clearly shows that $UIrSi_3$ is in the PM state down to 2 K. At 2 K, the highest value of M and ρ_H are observed whereas ρ exhibits its lowest value (Figs. 4.14 – 4.16). From the saturation of M can be deduced that the magnetic moments are aligned (polarized) in the direction of the applied magnetic field, corresponding to the PPM regime (Figs. 4.15 and 4.16). The same feature is observed in the ZFC mode when a magnetic field up to 8 T is applied at 2 K (Figs. 4.8, 4.17, 4.19). During cooling at zero field, $UIrSi_3$ undergoes AFM ordering which is maintained to low temperatures. Application of magnetic field on $UIrSi_3$ in the AFM ground state gives rise to a FOMPT at H_C from the AFM to a PM phase with polarized magnetic moments (PPM state). The FOMPT is manifested as a positive magnetization step at H_C, a positive $\rho_H(H)$ step and a negative $\rho(H)$ step where the magnetization and $\rho_H(H)$ reach maximum values and the resistivity reaches a minimum value.

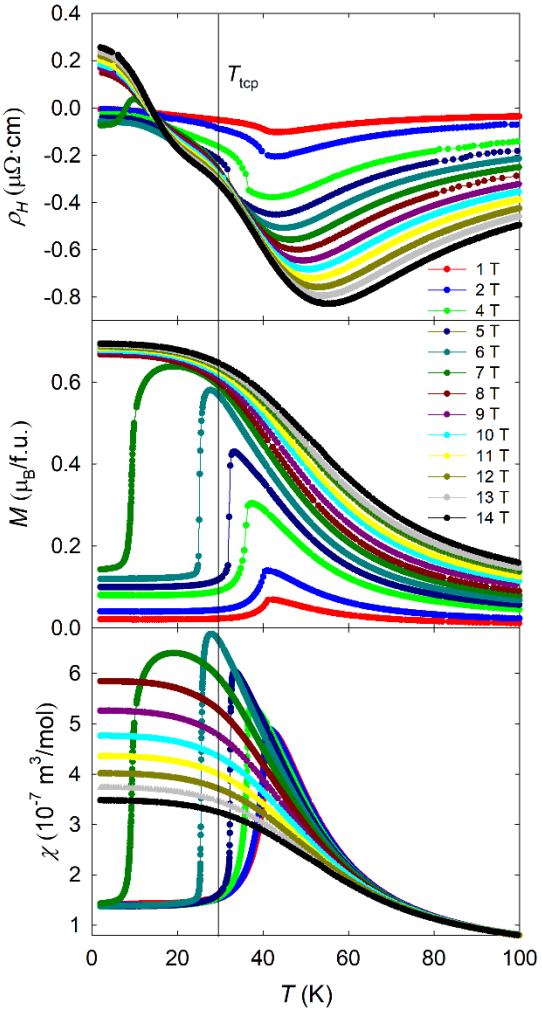

Fig. 4.20: Temperature dependence of the Hall resistivity (top panel), magnetization (middle panel) and magnetic susceptibility (bottom panel) measured at different constant magnetic fields applied along the *c* axis. The curves in the top panel are vertically shifted by -0.05 μΩ·cm.

It should be emphasized that the field-induced PPM state of an antiferromagnet in fields above H_c at low temperature is not FM but PM [69, 89]. In the transport properties, the low-temperature PPM regime of the PM state has several similarities with a collinear ferromagnet, but the underlying mechanism is fundamentally different. The order parameter of the ferromagnetism is spontaneous magnetization which is equal to the saturation magnetization at the low-temperature limit. The polarization of magnetic moments in the PPM regime at this low H_C reflects the FM (intra-sublattice) interaction between two AFM sublattices. The PPM regime of the PM state is metastable and undergoes a transition back to the AFM state when the magnetic field is reduced below $H_{c\downarrow}$. In the case of field-induced FM state, $UIrSi_3$ should undergo at a certain temperature a FM→ PM phase transition upon heating in a constant magnetic field higher than H_c (e.g. 8 T in the present case).

Such a transition should be visible in the temperature dependence of the specific heat measured in 8 T but, from 2 to 50 K, there is no sign of any anomaly. It is important fact that the PPM and the normal PM state are not two different magnetic phases but they are two different regimes of the same PM state. Therefore, these two regimes are not separated by any magnetic phase transition but a crossover region spreading in the PM phase space above the TCP. This crossover region (see Fig. 4.20) is gradually extended with increasing magnetic field and there can be observed indication of cross over region from the low-temperature border T_{LT} (for $T < T_{LT}$ the nearest isofield $M(T)$ curves are parallel indicating the fully polarized regime), and the high-temperature border T_{HT} (for $T > T_{HT}$ the nearest $M/H(T)$ curves coincide within experimental error). Closer inspection of Figure 4.20 reveals that the crossover is reflected in the temperature dependence of Hall resistivity mainly as a very broad bump on the negative slope followed by a valley (see Fig. 4.16). The normal PM regime (PPM regime) seems to be at temperatures above (below) the temperature of the inflection point on the positive (negative) slope of the $\rho_H(T)$ curve above 50 K (below 20 K).

In Figures 4.9, 4.17 and 4.19, positive $\Delta M(H)$ and $\Delta\rho_H(H)$ steps and a negative $\Delta\rho(H)$ step are clearly visible at H_C below T_{tcp} (28 K), corresponding to the FOMPT from AFM to PPM. Strikingly different behavior of $\rho_H(H)$ and $\rho(H)$ is observed in the temperature interval $T_{tcp} < T < T_N$ where $UIrSi_3$ undergoes a SOMPT from the AFM to the PM state.

These findings suggest the following simple approach to explain the experimental findings for $UIrSi_3$:

The FOMPT is the transition between the AFM and the PPM regime, whereas the SOMPT is the transition between AFM and PM regime. The PM regime is the classical PM state governed by thermal fluctuations of the magnetic moments. On the other hand, the PPM regime, present at low temperatures, is characterized by magnetic moments aligned along the magnetic field direction. The polarization of magnetic moments in the PPM state leads to a lower magnetic contribution to the electric resistivity but to a large contribution to the anomalous Hall resistivity. The point where the AFM ↔ PPM and the AFM ↔ PM transition come together is called the tricritical point. The following relationships between the values of the electric resistivity and the Hall resistivity exist in the three regimes:

$$\rho^{PM} > \rho^{AFM} > \rho^{PPM}, \tag{4.1}$$

$$\rho_H^{PM} < \rho_H^{AFM} < \rho_H^{PPM}. \tag{4.2}$$

A detailed study of the ρ_H and ρ anomalies in the neighborhood of the TCP in *T-H* phase space was performed by measuring the temperature dependences of $\rho_H(T)$ and $\rho_{[100]}(T)$ in constant field from 5.2 T to 6 T in 0.1 T steps. Furthermore, $\rho_H(H)$ and $\rho_{[100]}(H)$ were measured at temperatures from 25 K to 31 K in 1 K steps. The obtained data are plotted in Figures 4.21 and 4.22. The results clearly show a continuous change

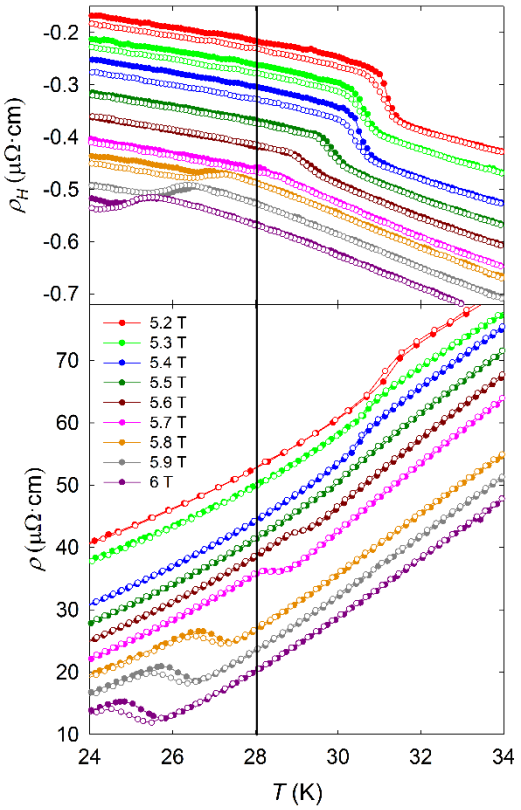

Fig. 4.21: Temperature dependence of the Hall resistivity (top panel), and the electric resistivity (bottom panel) at selected magnetic fields applied along the c axis in vicinity of the TCP. The full symbols represent measurements with increasing temperature and the open symbols measurements upon cooling. The vertical line is an estimation of the temperature where the polarity of the $\Delta\rho_H(T)$ step changes ($T \sim 28$ K at $\mu_0 H \sim 5.7$ T).

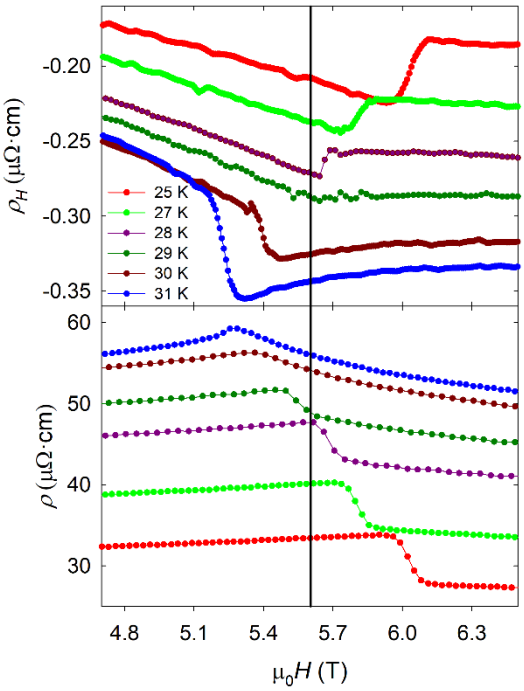

Fig. 4.22: Magnetic field dependence of Hall resistivity (top panel), and electric resistivity (bottom panel) measured at selected constant temperatures in the vicinity of the TCP with magnetic field applied along the c axis. Only data measured with increasing field are displayed. The vertical line is an estimation of the point where the polarity of the $\Delta\rho_H(H)$ step changes ($\mu_0 H \sim 5.6$ T at $T \sim 29$ K).

from positive $\Delta\rho_H(H)$ and $\Delta\rho_H(T)$ steps (below the TCP) to negative $\Delta\rho_H(H)$ and $\Delta\rho_H(T)$ steps (above the TCP) with increasing temperature and magnetic field, respectively. The change of polarity of the Hall resistivity, which is reflected by the absence of a step in the measured curves, corresponds very well with the expected position of the TCP. It is found that the evolution of the $\Delta\rho_{[100]}(H)$ and $\Delta\rho_{[100]}(T)$ steps does not correlate with the evolution of the $\Delta\rho_H(H)$ and $\Delta\rho_H(T)$ steps. This is due to the important role of field-induced spin-flip fluctuations in the AFM state which causes enhancement of the electric resistivity at temperatures above T_{tcp}.

The simultaneous sharp steps in the magnetization, specific heat, electric resistivity and Hall resistivity characterize the first-order MT phase transition and, in addition, the sharp steps in the latter three properties points to the occurrence of FS

reconstruction, which is called the Lifshitz transition [83] at MT. Recently, the possible occurrence of a Lifshitz transition has been reported for the antiferromagnet UPd_2Si_2 [90, 91]. In UPd_2Al_3 interesting phenomena concerning a cascade of Lifshitz transitions are indicated by anomalies in the Seebeck coefficient in the AFM state below H_C followed by a Lifshitz transition [92]. In the light of these facts, a measurement of the Seebeck coefficient was performed. The Seebeck coefficient is given by

$$S = -\frac{\pi^2 k_B^2}{3|e|} T\left[\frac{\partial lnN(E)}{\partial E} + \frac{\partial ln\tau(E)}{\partial E}\right]_{E=E_F}, \qquad (7)$$

where $N(E)$ is the density of states and τ(E) the relaxation time of the conduction electrons [93] which is linked with the FS. By means of the Seebeck coefficient, the FS reconstruction can be established through the change of the energy derivative of the density of states at E_F which can be observed as a sudden change of $S(H)$ at the transition. The results of measurement of the field dependence of the Seebeck effect, with applied magnetic field and heat pulse along the *c* axis, are presented in Figure 4.23 Below T_{tcp}, the $S(H)$ curves clearly exhibit a sharp step at H_C, as observed in isotherms where the MT is first order. The observed step in $S(H)$ with simultaneous steps in $\rho(H)$, $\rho_H(H)$ and $C_p(H)$ at temperatures below T_{tcp} suggests that the FOMPT in $UIrSi_3$ is probably a Lifshitz transition with FS reconstruction.

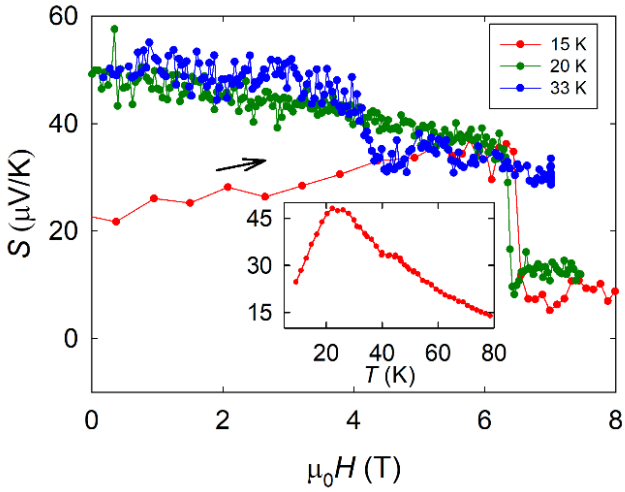

Fig. 4.23: Seeback coefficient measured at 15 K, 20 K and 33 K in magnetic field along the c axis. The arrow shows the direction of magnetic field sweep. The inset displays the temperature dependence of the Seebeck coefficient at zero field.

The isofield $S(H)$ curves measured above T_{tcp} have no sharp step but a narrow valley manifesting the SOMPT. Figure 4.23 shows the differences in the initial slope in the field dependences between 15 K and higher temperatures. These differences are explained by temperature dependence of $S(T)$ in zero field, shown in the inset of Figure 4.23, where a peak centered at ½ T_N is seen, which is expected as a result of gapping of the FS below T_N [94].

Closer inspection of the results obtained for the field dependence of electric resistivity, Hall resistivity, magnetization and specific heat in Figure 4.24 clearly shows that, in the measurement of the electric resistivity with current along the *c* axis, another anomaly is observed below H_C. However, no anomaly is observed in the measurements of Hall resistivity, magnetization and specific heat on the same sample. However, there

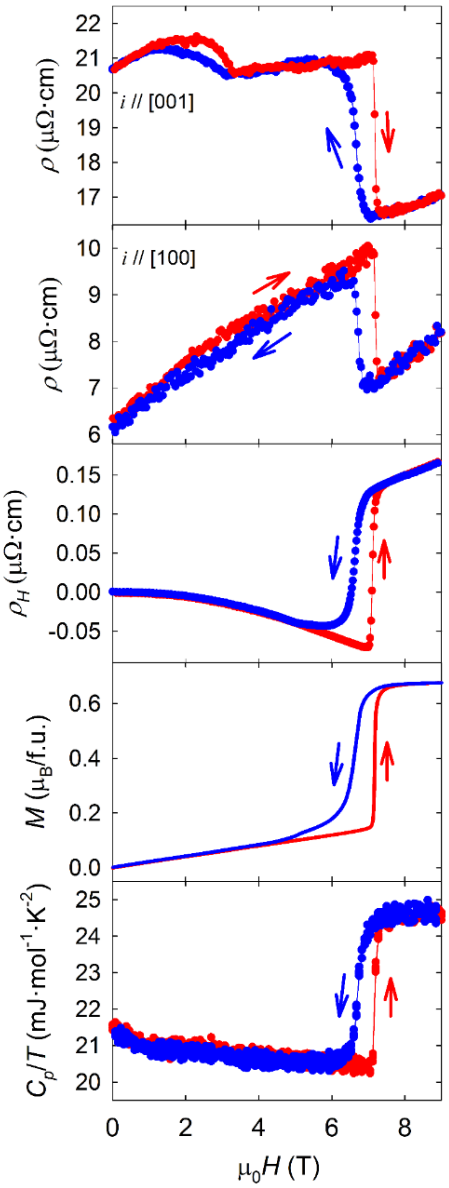

Fig. 4.24: From top to bottom panel:
- electrical resistivity for *i*//[001],
- electrical resistivity for *i*//[100],
- Hall resistivity,
- magnetization,
- specific heat divided by temperature

of $UIrSi_3$ at 2 K as functions of a magnetic field applied along the *c* axis.

is a certain analogy with CePtSn [95-98] which may indicate a transition between two AFM phases give no indication in magnetization curves. The electric resistivity results from scattering of conduction electrons to which also the magnetic moments contribute. A change of magnetic structure implies a change of the scattering factor of the conduction electrons and therefore may influences the electric resistivity. Depending on change of the magnetic structure, there may be a change of the electric resistivity without measureable changes in magnetization and specific heat. However, this is pure speculation and more experiments have to be done focused on the magnetic structure for example neutron or μSR experiments. The observed value of H_C from measurements of electric resistivity, Hall resistivity and Seebeck coefficient perfectly agree well with the values displayed in the magnetic phase diagram (Fig. 4.25).

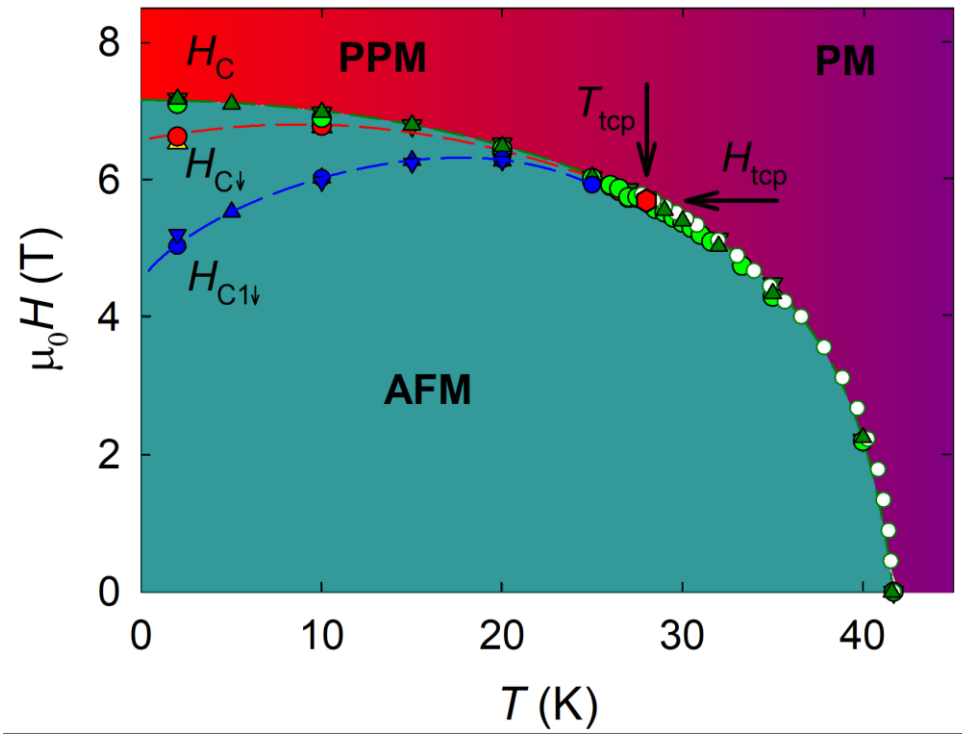

Fig. 4.25: Constructed magnetic phase diagram of $UIrSi_3$. The quantities H_c, $H_{c\downarrow}$ and $H_{c1\downarrow}$ are colorfully separated. The shape of the data points represent the origin of the data: $C_p(T)$... H_c - green open circles; $M(H)$ - triangle up; ρ_H - full circles, ρ - triangle down. The dashed lines are guides to the eyes. The red hexagonal point indicates the tricritical point (T_{tcp} = 28 K, $\mu_0 H_{tcp}$ = 5.8 T).

4.1.6. Dilatometry and magnetostriction measurements

Dilatometry measurements provide knowledge on crystal-lattice changes by external parameters like temperature, magnetic field, electric field and pressure, but also, for instance, on the magnetic state of materials, etc. We have focused on the thermal expansion, which includes effects of magnetic ordering, and on the influence of a magnetic field.

The thermal expansion of the *a* and the *c* axis was measured on a $UIrSi_3$ single crystal. The results displayed in Figure 4.26 show large anisotropy of the thermal expansion. Upon cooling, the thermal expansion along the *a* axis continuously decreases down to the AFM ordering temperature T_N where it exhibits a clear change of curvature. The thermal expansion along the *c* axis decreases at a much lower rate, exhibiting a very gentle minimum around 50 K and, like along the *a*-axis, an inflection point at T_N. Further cooling does not lead to an appreciable change of the *c* axis thermal expansion. In contrast, the change of the thermal expansion of the *a* axis in the AFM state is considerably larger. Reminding the tetragonal crystal structure the change of volume can be calculated. The volume change derived from the thermal-expansion results along the *a* axis and *c* axis, exhibits a pronounced change of curvature at T_N.

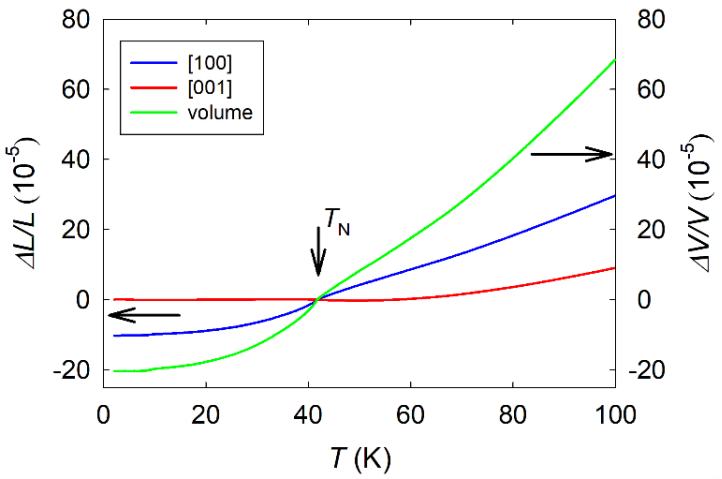

Fig. 4.26: Linear thermal expansion for the *a* and *c* axis (blue and red lines, respectively) and the volume thermal expansion (green line). The vertical arrow marks the magnetic transition as determined by specific-heat measurement.

The thermal-expansion coefficients can be calculated using equation 2.30 and are displayed in Figure 4.27. As expected, the magnetic ordering, manifested as a peak-shape anomaly, is much more pronounced in the *a*-axis thermal-expansion coefficient (α_a) than in the *c*-axis thermal-expansion coefficient (α_c). Knowing the step of the thermal-expansion coefficients step at T_N together with the step of the specific heat divided by temperature ($\Delta C_p/T$) at the magnetic ordering, the pressure dependencies can be calculated via the thermodynamic Ehrenfest relations (Eq. 2.33). The anisotropic pressure dependence can be estimated via $\Delta\alpha_a$ and $\Delta\alpha_c$ and are shown in Table C. The calculations provide a quite high hydrostatic-pressure dependence of T_N amounting to dT_N/dp = 1.93(5) K/GPa.

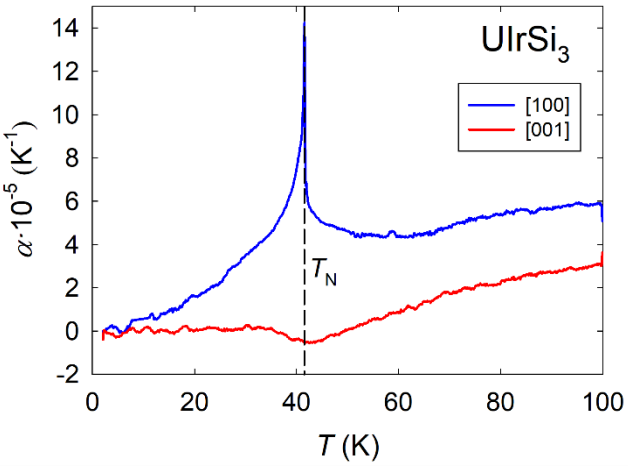

Fig. 4.27: Linear-thermal-expansion coefficients for the *a* axis (blue curve) and the *c* axis (red curve). The dashed line marks T_N as obtained from measurement of the specific heat.

Table C: Steps of the thermal-expansion coefficient $\Delta\alpha_i$ at T_N for the *a* axis, the *c* axis and the volume with corresponding pressure coefficients calculated via the Ehrenfest relations.

	$\Delta\alpha_i$ (K^{-1})	dT_N/dp (K/GPa)
a	$1.42(5)\cdot10^{-5}$	0.92(5)
c	$-5.3(4)\cdot10^{-7}$	-0.04(5)
V	$2.79(5)\cdot10^{-5}$	1.93(5)

The magnetostriction along the *a* and the *c* axis was measured in a magnetic field applied along the *c* axis. As can be seen in Figure 4.28, large changes of the dimensions of the sample are observed at the MT. With increasing field, the magnetostriction shows a sharp expansion along the *c* axis and a sharp contraction along the *a* axis for a field sweep up measurement with hysteretic behaviour which is characteristic for a FOMPT. The asymmetric hysteresis observed in the measurements of $M(H)$, $\rho(H)$, $\rho_H(H)$ and $C_p(H)$ is also observed in the magnetostriction measurements. In Figure 4.29, the magnetostriction measurements along *c* and *a* axis around the MT are compared. Increasing the temperature in the magnetostriction measurements induces the same behavior at H_C as in other measurements. It is clear that magnetostriction along the *c* axis is similar to the $M(H)$ isotherms and, above 25 K, the height of the expansion step gradually decreases with increasing temperature. With increasing temperature, the contraction step along the *a* axis becomes gradually smaller. Nevertheless, the field hysteresis of the MT vanishes with increasing temperature for both magnetostriction measurements in the same way. The knowledge of the structure allows to derive the volume change from the results of the magnetostrictrion measurements for both directions. The resulting volume change is plotted in Figure 4.29, showing a sharp contraction at H_C and the presence of asymmetric hysteresis. Similar to the magnetostriction measured along the *a* axis, increasing temperature causes reduction of the hysteresis and a contraction step at H_C. The sudden change of the volume at H_C vanishes above 30 K and, at higher fields, the volume change curve gradually gets a convex curvature.

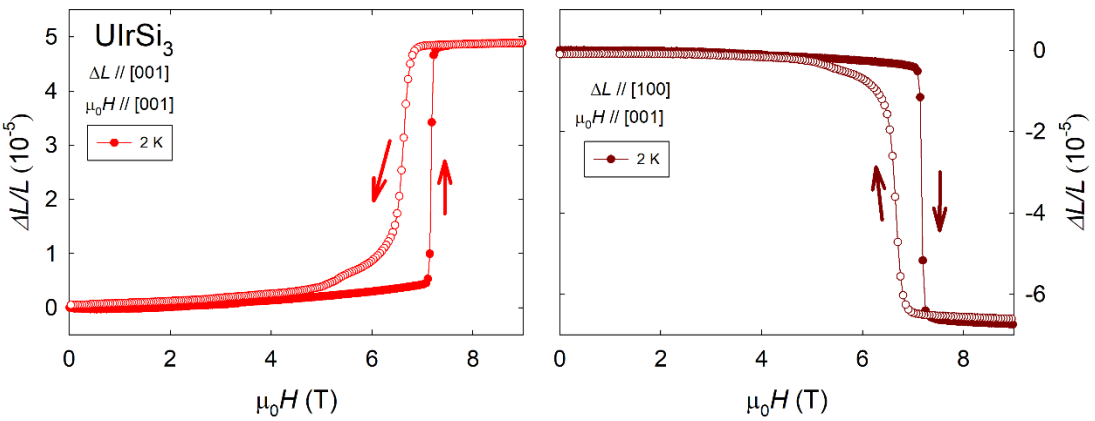

Fig. 4.28: Longitudinal magnetostriction measured along the *c* axis (left panel) and transversal magnetostriction measured along the *a* axis (right panel) in magnetic field applied along the *c* axis. The arrows show the sweep direction of the magnetic field.

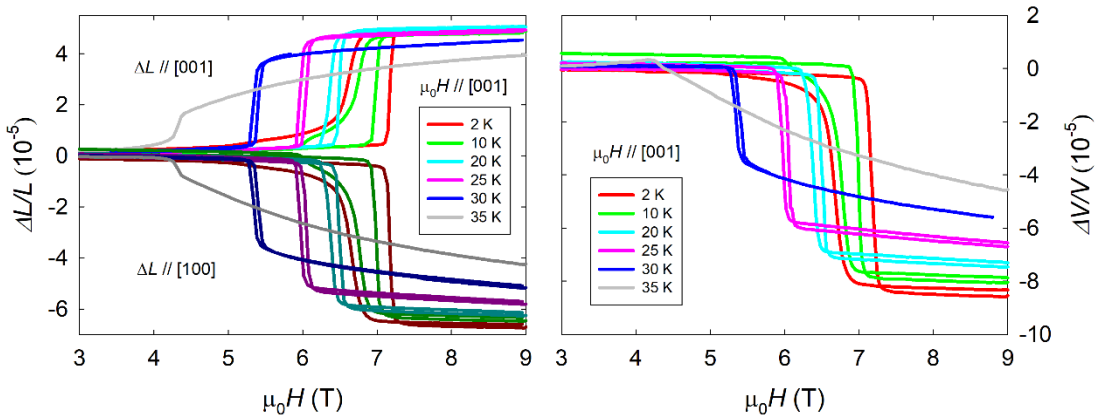

Fig. 4.29: Longitudinal (light colors) and transversal (dark colors) isothermal magnetostriction measured with the magnetic field applied along the *c* axis (left panel) and the change of volume derived from the magnetostrictrion measurements (right panel).

4.2. Pressure effect on $UIrSi_3$

4.2.1. Electric resistivity under pressure

Electric-resistivity measurements were performed using a clamp pressure cell CPC (see Section 3.4.2) and a Bridgman anvil pressure cell BAC (see Section 3.4.3). Pressure cells have been inserted into the PPMS device and connected with the measurement system. For the BAC, the pressure was calibrated with the superconducting transition of lead and, in the case of the CPC, a calibrated manganin wire has been used which gives the pressure at room temperature. The pressure correction for determination of the pressure at low temperatures for measurements with the CPC has been used according to Ref. [99].

The experimental assembly for the electric-resistivity measurements with the CPC is shown in Figure 3.13 in Section 3.4.2. For the BAC, the assembly is shown in

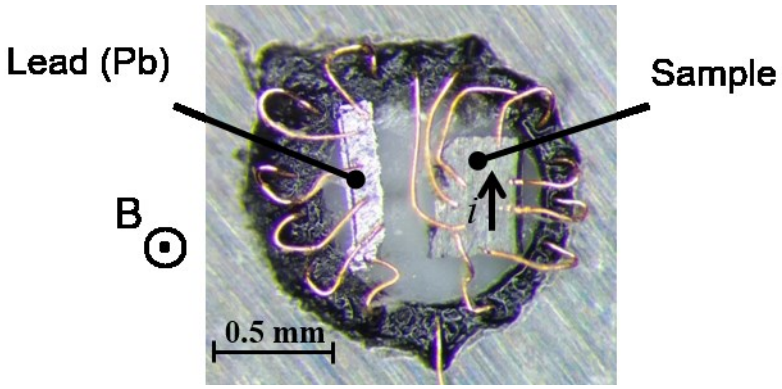

Fig. 4.30: Experimental assembly of the electric-resistivity measurement with the BAC. Details of the bottom anvil with contacted sample and lead are shown. The arrow shows the direction of the current which is perpendicular to the direction of the external magnetic field.

Figure 4.30. The sample was contacted with insulated Cu wires (Ø 25 µm) by spot-welding after removing the insulation of the wire using the chemical DEPAINT. In the same way, the pressure manometer was contacted, with lead in this case.

Firstly, a pressure measurement with the CPC was performed with the current oriented along the *c* axis. Figure 4.31 shows the temperature dependence of the electric resistivity at different pressures up to 2.5 GPa.

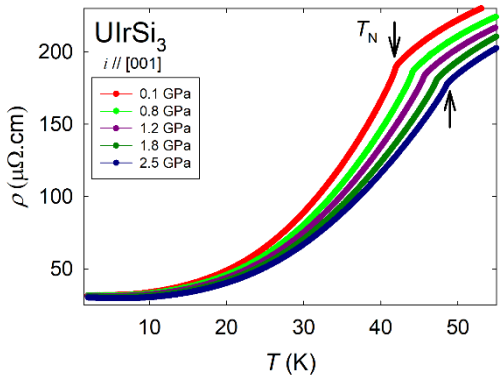

Fig. 4.31: Temperature dependence of the electric resistivity at different pressures up to 2.5 GPa.

The application of pressure causes a shift of T_N to higher temperatures. The increase of T_N seems to be nicely represented by two linear dependences which was chosen *ad-hoc* for comparison of the pressure dependences (Fig. 4.32). At low pressures, T_N increases with a rate of dT_N/dp = 3.0(2) K/GPa. The connecting measurement with the BAC shows continued increasing of T_N and, at higher pressures, the pressure coefficient of T_N is 1.7(2) K/GPa (Fig. 4.32).

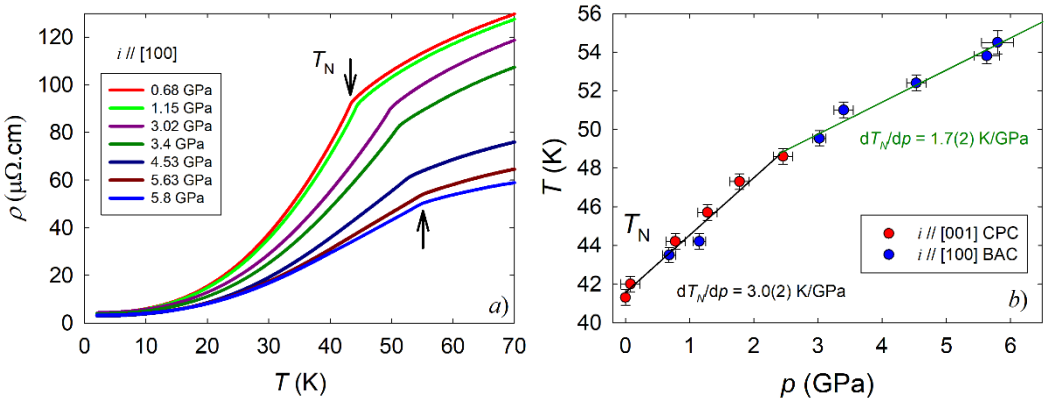

Fig. 4.32: *a*) Temperature dependence of the electric resistivity measured at different pressures and with the current along the *a* axis. *b*) Pressure evolution of T_N. The black line represents a linear fit at low pressures and the green line represents a fit of the data from 2.5 to 5.8 GPa.

The results suggest that the pressure sensitivity of the ordering temperature will continue to higher pressures so that the expected decrease of T_N will be observed at even higher pressures. Eventually, T_N is expected to decrease due to the loss of the itinerant U magnetic moment, caused by shortening of the distance between the U spacing atoms which leads to high hybridization. Depending on the initial spacing, the

antiferromagnetic interaction can be firstly strengthen without significant weakening of U magnetic moment.

Magnetoresistance under pressure

The H_C of the MT is clearly observable by measurement of the magnetoresistance in applied magnetic fields up to 14 T. Due to sample-space restriction within the used pressure cells, the electric current and external magnetic field are fixed with respect to the crystallographic direction of the sample. The longitudinal magnetoresistance with electrical current along the *c* axis was measured in the CPC and the transversal magnetoresistance with electric current along the *a* axis was measured in the BAC.

Under application of pressure, H_C of the MT shifts to lower magnetic field as is displayed in Figure 4.33. The anomaly observed below H_C (around 3 T), presumably associated with another AFM phase, decreases with increasing pressure but with a slower rate than H_C. Under application of pressure, a new anomaly appears above H_C and becomes more pronounced with increasing pressure. The origin of this anomaly is not yet understood.

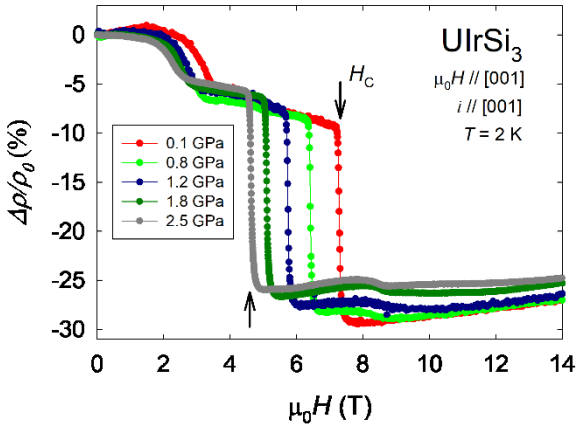

Fig. 4.33: Longitudinal magnetoresistance curves at 2 K at different pressures.

The transversal magnetoresistance under pressure measured with the BAC shows a decrease of H_C up to the maximal applied pressure of 5.8 GPa (Fig. 4.34). The MT remains a FOMPT with asymmetrical hysteresis at 2 T as is shown in Figure 4.34. The sharp drop of resistivity becomes gradually broader which can be caused by not ideal hydrostaticity of the pressure in the sample space.

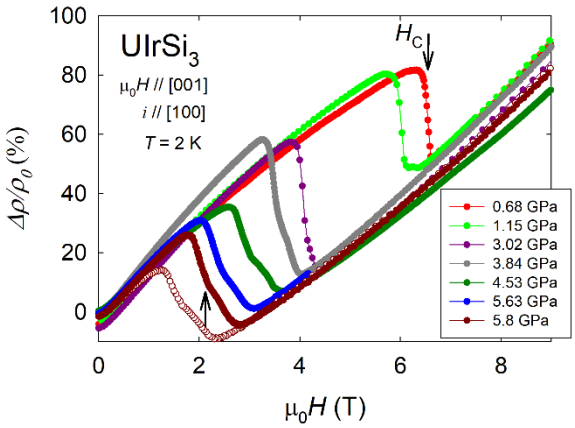

Fig. 4.34: Transversal magnetoresistance at 2 K at different pressures up to 5.8 GPa. The full symbols represent measurements with increasing magnetic field and the open symbols (at 5.8 GPa) show data measured with decreasing magnetic field for observation of the field hysteresis.

The pressure evolution of H_C at 2 K is plotted in Figure 4.35. H_C decreases nearly linearly with increasing pressure but there is clear evidence of a change to a decreasing rate. The change of H_C at low pressures below is dH_C/dp = -1.15(4) K/GPa and, at higher pressures, a linear fit gives dH_C/dp = -0.73(5) K/GPa. As is clearly seen in Figure 4.34, the hysteresis remains under pressure and becomes slightly larger with increasing pressure (Fig. 4.35).

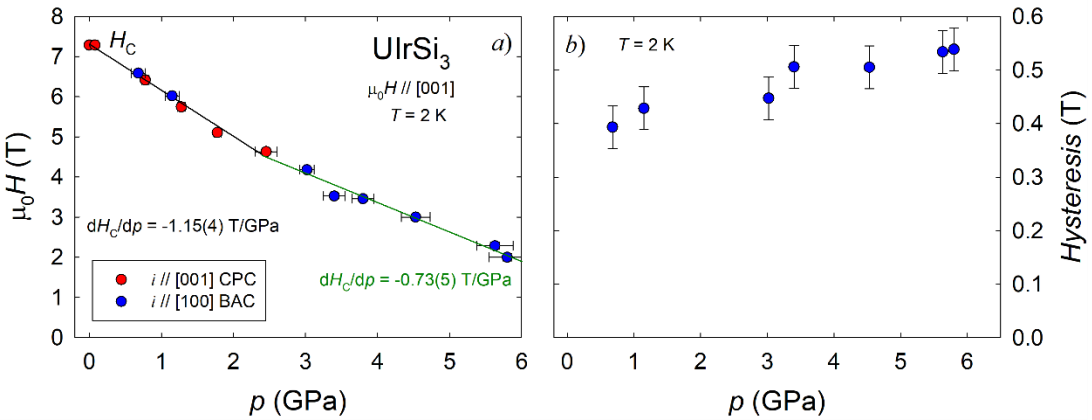

Fig. 4.35: *a*) Pressure dependence of H_C measured at 2 K. The black line represents a linear fit below 2.5 GPa and the linear fit above 2.5 GPa is represented by the green line. *b*) Pressure evolution of the field hysteresis.

The magnetoresistance curves measured at different temperatures provide information about the order of the transition, as is shown in Section 4.1.5 and Figure 4.17. Similar temperatures have been used for measurement of the magnetoresistance curves under pressure where a pressure-induced magnetic transition is observed. Figure 4.36 presents magnetoresistance data measured at 45 K at different pressures. Clear evidence of the paramagnetic state is observed up to 3 GPa where the magnetoresistance curve has a maximum and the positive magnetoresistance evolution below H_C is followed by a negative magnetoresistance evolution above H_C. This provides evidence of a pressure-induced AFM transition at 45 K between 1.15 and 3.02 GPa which is second order magnetic transition induced by pressure and

characterized by a maximum at H_C. Above 4.53 GPa, the magnetoresistance does not exhibit a positive magnetoresistance anomaly below H_C and no sharp maximum. The transition is connected with a sudden drop of the resistivity which is a sign of a FOMPT. Furthermore, field hysteresis can be observed. Evidently, at 45 K the system has passed the TCP between 4.53 and 5.63 GPa.

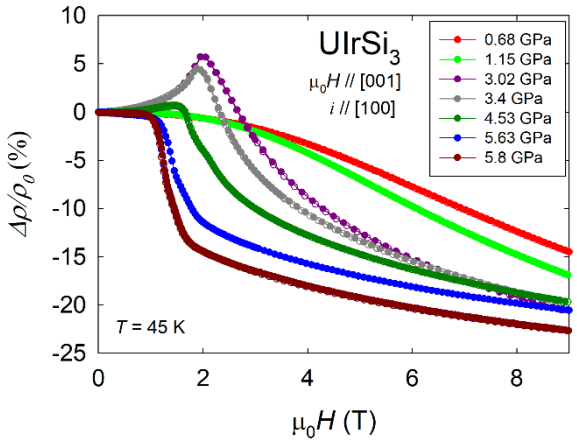

Fig. 4.36: Magnetoresistance curves at 45 K at different pressures.

The magnetoresistance curves provide an observation of the pressure evolution of the TCP (see Fig. 4.37). The temperature of the TCP follows the pressure evolution of T_N but the pressure coefficient of T_{tcp} has a higher value than for T_N. A similar pressure evolution as for H_C is observed for H_{tcp}. The initial, almost the same, pressure coefficient determined at low pressures but in the high pressure region the H_{tcp} has a slower rate than rate for H_C.

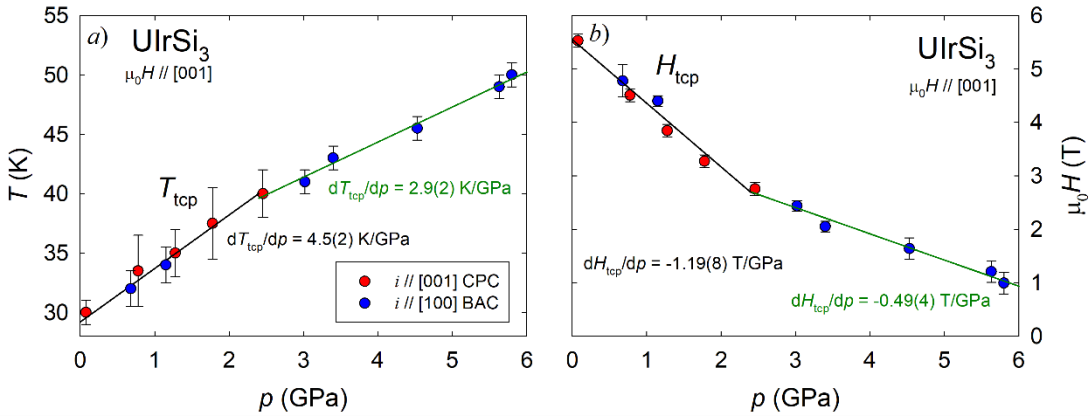

Fig. 4.37: Pressure phase diagrams of T_{tcp} (*a*) and H_C (*b*) with fits at low pressures (black line) and high pressures (green line).

Based on the results of the pressure measurements, we can make an estimation of evolution T_N, T_{tcp} and H_C in higher pressures. The different rate of the pressure evolution for T_N and T_{tcp} is displayed in Figure 4.38 and it shows a possible crossing point at 9.5 GPa where probably a FOMPT will be present at zero magnetic field. Nevertheless, extrapolation of the H_C pressure evolution gives a critical pressure for suppression of the AFM order of 8.6 GPa. There can only be speculation what will

happen above the accessible pressure region. We estimate that, at suppression of H_C, which is the magnetic field necessary to force parallel alignment of magnetic moments, to zero field, ferromagnetic order will be induced by pressure. Disappearance of T_{tcp} is estimated when $H_C = 0$ T and T_N will change T_C.

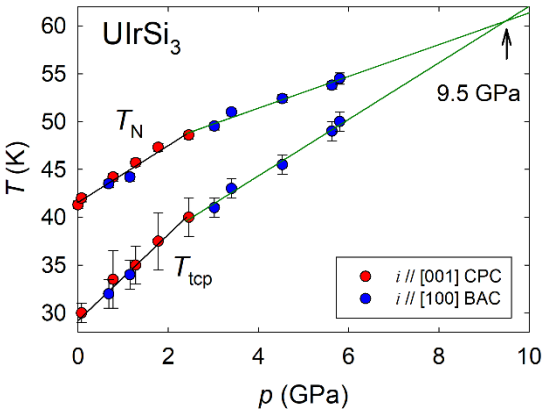

Fig. 4.38: Extrapolation of the pressure evolution of T_N and T_{tcp} above the measured region.

The final pressure phase diagram is plotted in Figure 4.39 showing opposite pressure evolution of H_C and T_N. H_C decreases with increasing pressure in contrast to T_N which increases. The TCP (T_{tcp}, H_{tcp}) follow pressure evolution of T_N and H_C. The increasing T_N suggests stronger AFM interactions. On the other hand, the decrease of H_C reflects easier suppression of the AFM ordering by the magnetic field. It can be a manifestation of stronger FM interactions between two magnetic sublattices along the *c* axis.

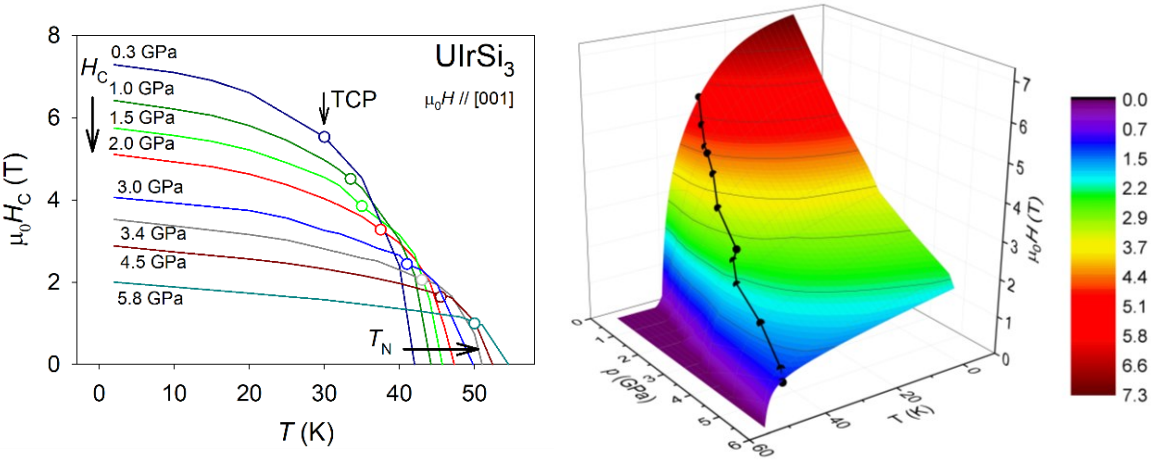

Fig. 4.39: Constructed phase diagrams of $UIrSi_3$. The left part shows a 2D diagram with several isobar curves. The open circle represents the presence of a TCP. Right part shows 3D phase diagram with marked TCP as black points.

4.2.2. Compressibility

The measurement of the compressibility was performed using strain gauges (described in Section 3.4.2) oriented in sensitivity direction along the *a* and *c* axis of $UIrSi_3$. Two samples with appropriate shape have been used (see Fig. 4.40). A clamp pressure cell with inner diameter of 6 mm and Daphne 7373 as pressure transmitting medium was used. The compressibility was measured at room temperature. The correction for the material of the used strain gauge was obtained from measurement of Cu using the same type of strain gauges. The measured strain is plotted in Figure 4.41 with a determined compressibility $\kappa_{L//c} = 2.17(1)\cdot10^{-3}$ GPa^{-1} for the *c* axis and $\kappa_{L//a} = 7.48(2)\cdot10^{-3}$ GPa^{-1} for the *a* axis. The results clearly show that the *a* axis is more than three times softer than the *c* axis. This result is in agreement with the thermal expansion (Fig. 4.26) where, below T_N, the lattice parameter *c* is almost unchanged and the lattice parameter *a* decreases with increasing temperature.

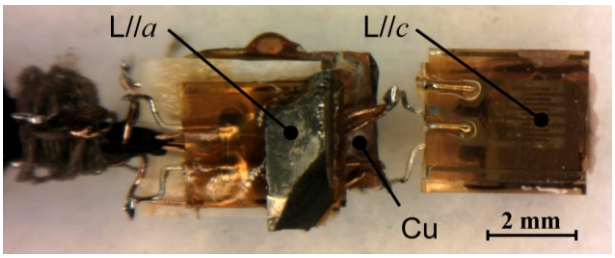

Fig. 4.40: Pressure assembly for measurement of the compressibility by means of strain gauges.

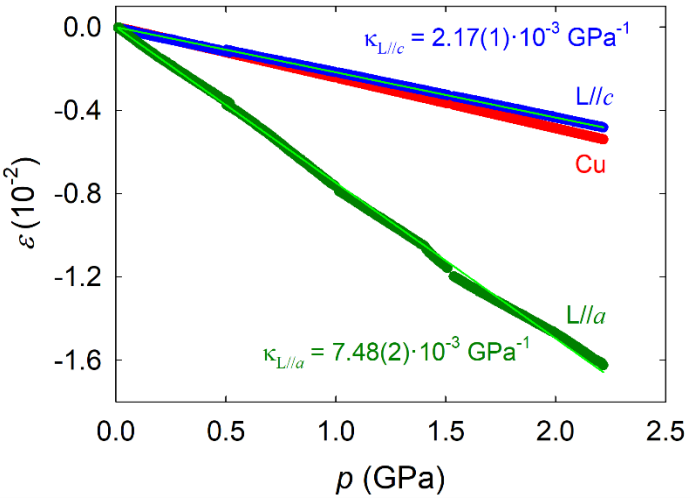

Fig. 4.41: Evaluated strain from measurement of resistivity change of the strain gauges for Cu and two crystallographic directions of $UIrSi_3$.The colored lines show fits used for the evaluation of compressibility.

The results of the compressibility measurements lead to the conclusion that under hydrostatic pressure the lattice parameter *a* changes more than the parameter *c*. The larger reduction of *a* may be responsible for the increase of T_N. The U-U distances are reduced which results in a change of the 5f-electron hybridization and ultimately the strength of magnetic interactions along the *a* axis and/or the value magnetic moment. In a model of two magnetic sublattices with antiparallel orientation of

magnetic moments, the intra-lattice exchange interaction becomes stronger. There is a competition between the FM and AFM interactions which are also indicated by the susceptibility measurements Section 4.1.3. The most logical reason of the increase of T_N is strengthening of the AFM interaction along the *a* axis. On the other hand, the decrease of H_C points to weakening of the resulting AFM interaction along the *c* axis. This can be interpreted as strengthening of the AFM intra-lattice exchange interaction as well as of the FM inter-lattice exchange interaction which still remains smaller than AFM inter-lattice exchange interaction. Evidently, the pressure evolution of magnetism in $UIrSi_3$ is driven by magnetoelastic coupling.

4.2.3. Magnetization under uniaxial pressure

A sample of $UIrSi_3$ with dimensions 1.4x0.63x0.33 mm^3 has been used for a magnetization measurement under uniaxial pressure along the *c* axis in the MPMS device. The measurement was performed using a miniature uniaxial pressure cell (see Section 3.4.1). The low signal of the sample does not allow measurement of the temperature dependence of magnetization but due to large increase of magnetization at MT the magnetization curves were measured. The results at 25 K and 35 K are plotted in Figure 4.42. Up to a uniaxial pressure of 0.69 GPa along the *c* axis, H_C shows a slight shift and a broadening of the magnetization jump at the MT is observed. The saturation magnetization is unchanged under the applied pressures. The broadening of the magnetization jump be caused by non-homogeneous distribution of the applied load on the sample. The distribution of the load was almost homogenous as the sample was not broken under the applied uniaxial pressures up to 0.69 GPa. The growth of a microscopic lattice defect can be the cause of the broadening.

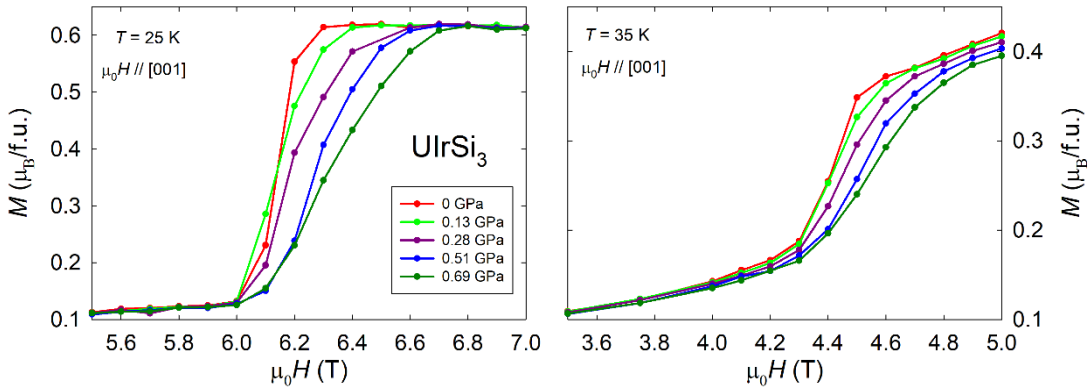

Fig. 4.42: Magnetization of $UIrSi_3$ at 25 K (left picture) and 35 K (right picture) measured in magnetic field along the *c* axis under uniaxial pressure also applied along the *c* axis.

The slight shift of H_C suggests that the magnetic phase is almost insensitive to a change of the lattice parameter *c*. For simplicity we can suppose the sample as incompressible which leads to volume conservation under uniaxial pressure. In such a case, shortening of the lattice parameter *c* implies a small expansion of the lattice parameter *a* which could explain the slight increase of the H_C. Considering the results of the hydrostatic-pressure measurements, it is obvious that the lattice parameter *a* is a leading parameter for magnetic changes caused by application of pressure.

4.3. Neutron diffraction on $UIrSi_3$

4.3.1. Neutron-diffraction experiments

Neutron-diffraction experiments have been performed on the nuclear and magnetic structure of a $UIrSi_3$ single crystal using the Cylindrical Ccd Laue Octagonal Photo Scintillator (CYCLOPS) and D10 neutron diffractometers at the Institute Laue-Langevin (ILL), Grenoble, France.

In the first step, we performed a Laue neutron-diffraction experiment using the CYCLOPS diffractometer. The Laue diffraction confirmed the good quality of the investigated single crystal as well as the AFM ground state of $UIrSi_3$ (see Fig. 4.43). Comparison of the Laue patterns taken in the PM state and below T_N allowed us to identify at least ten magnetic reflections in addition to the nuclear reflections (one set of magnetic reflections is marked as white circles in the detail of Figure 4.43). Employing ESMERALDA suite for evaluation of data [100], all observed magnetic satellites could be described with the propagation vector k = (0.1, 0.1, 0).

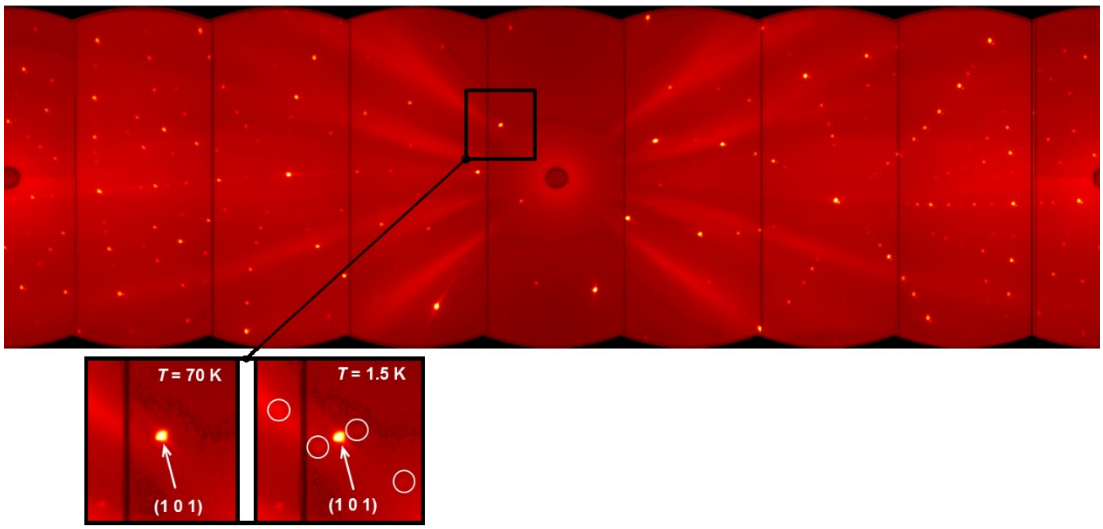

Fig. 4.43: Laue pattern recorded above T_N at 70 K (upper picture) and details around the (1 0 1) nuclear reflection at temperatures above (70 K) and below (1.5 K) T_N.

The knowledge of the propagation vector and the nuclear structure allowed us to perform a symmetry analysis leading to two irreducible representations. The first representation has one basis vector (1 -1 0) which allows orientation of magnetic moments in basal plane, only. The second representation possesses two basis vectors (1 1 0) and (0 0 1) which allows also orientation in the c-axis direction.

In the next step, we performed an experiment on the D10 diffractometer using a neutron wavelength of 2.36 Å. Omega-scans of 129 nuclear reflections at 2 K were measured, from which 40 reflections were independent. The refinement of the nuclear structure confirmed the non-centrosymmetric tetragonal structure of $BaNiSn_3$-type to be the crystal structure of $UIrSi_3$ with crystal lattice parameters a = 4.162(1) Å and c = 9.665(10) Å. Fullprof package agreement factors were R_B = 0.944% and R_F = 5.14%.

The temperature evolution of the magnetic and nuclear reflections was followed in the temperature range from 1.7 to 50 K (Fig. 4.44). The integrated intensity of the nuclear reflections remains the same (within the error) within the whole investigated temperature interval indicating that there is no magnetic intensity on the positions of the nuclear reflections. The intensity of the magnetic reflections starts to develop below T_N = 42 K and increases down to 20 K where the measured magnetic moments remain saturated. The fit of critical exponent $\beta = 0.24(1)$ is close to the predicted critical exponent $\beta = 0.3$ for the 3D Ising model [101]. No magnetic intensity is observed at temperatures above T_N, in good agreement with the measured macroscopic properties.

A measurement of 83 magnetic reflections was performed. The collected data and the calculated irreducible representations were used for the refinement of the magnetic structure. However, so far, we were not able to refine the magnetic structure unambiguously. The agreement factors for our best-fit structure are R_B = 50.2% and R_F = 10.6%. It seems that the magnetic structure is more complicated.

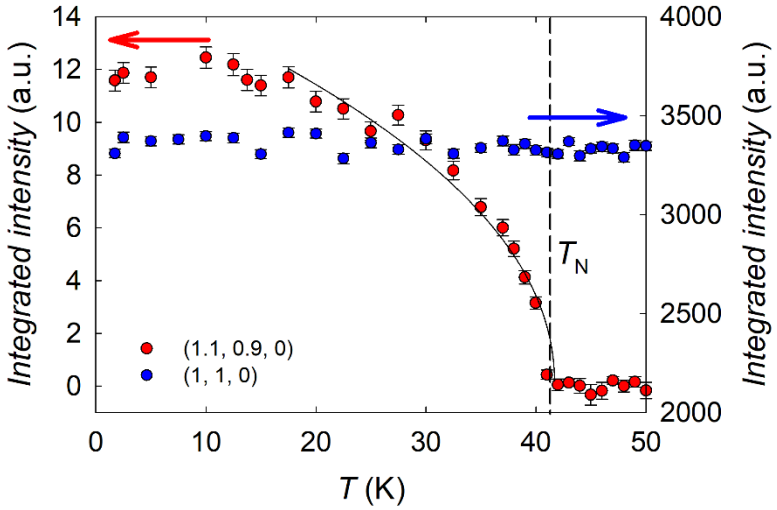

Fig. 4.44: Temperature dependence of the integrated intensity of the measured magnetic (red points) and nuclear reflections (blue points). The black line represents a fit of the critical exponent β.

4.3.2. Neutron diffraction in applied magnetic field

A neutron-diffraction experiment on a $UIrSi_3$ single crystal in magnetic fields up to 8 T applied along the *c* axis was performed in the POLI diffractometer at the Heinz Maier-Leibnitz Zentrum (MLZ), Munich, Germany.

Measurement of the integrated intensity of several nuclear reflections showed that there is no change of crystal structure at the MT (in the applied magnetic field). A linear increase of the integrated intensity of nuclear reflections shows an approximately linear dependence of the FM signal on the applied magnetic field (see Fig. 4.45).

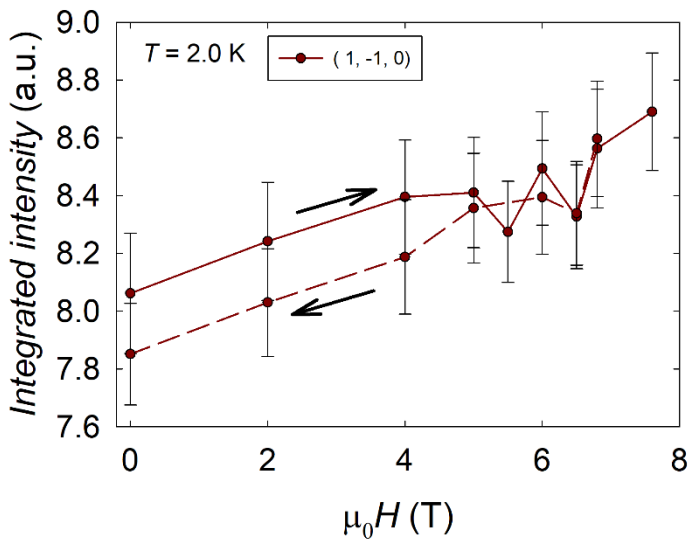

Fig. 4.45: Field dependence of the integrated intensity of nuclear reflections. Arrows mark measurement during increasing and decreasing magnetic field.

The magnetic-field dependence of the magnetic reflections revealed no change of the integrated intensity, within the experimental error, up to H_C where the magnetic reflections disappear. A shift of position of the magnetic reflections was observed by application of magnetic field. This shift manifests a change of the propagation vector. The several q-scans around magnetic satellites have been performed, revealing that the propagation vector always changes in the *hk0* direction and that no further symmetry breaking appears. The change of propagation vector is demonstrated in Figure 4.46 where the propagation vector is marked as (τ, τ, 0).

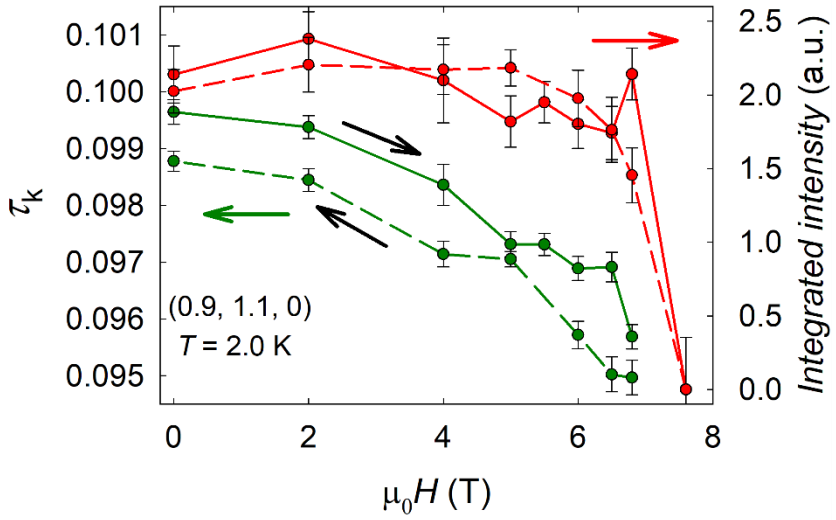

Fig. 4.46: Change of the propagation vector in applied magnetic field determined from measurement of the (0.9, 1.1, 0) magnetic reflection (left axis) and its integrated intensity (right axis). Arrows indicate increasing and decreasing magnetic field curves.

Figure 4.46 suggests field hysteresis in the propagation vector which may be expected. On the other hand, the change of the difference between curves measured

during increasing and decreasing of magnetic field is small and marked errors in Figure 4.46 origin from fit of the data. Nevertheless, the real errors originating from the devices are large so that we cannot confirm hysteresis of the propagation vector.

5. Conclusions

The successfully grown single crystal of $UIrSi_3$ was thoroughly characterized. Crystallization in tetragonal non-centrosymmetric $BaNiSn_3$-type crystal structure was confirmed. $UIrSi_3$ was found to undergo transition to antiferromagnetic ordering with strong uniaxial anisotropy below $T_N = 41.7$ K. The small magnetic entropy associated with the AFM transition and small magnetic moment in the polarized metamagnetic phase point to the itinerant character of the uranium magnetic moment. The opposite signs of the paramagnetic Currie temperatures of the *a*-axis and *c*-axis paramagnetic susceptibility as well as the low $H_C = 7.3$ T at 2K of metamagnetic transition contrasting with high value of T_N manifest the competition of AFM and FM interactions.

$UIrSi_3$ has been shown as an example of an antiferromagnet with strong uniaxial anisotropy showing the tricriticality typical for Ising antiferromagnets with competing AFM and FM interactions. The 1st order metamagnetic transition (FOMPT) accompanied by jumps of electrical resistivity, Hall resistivity and Seebeck coefficient, positive jump of observed quantities at temperatures < 28 K provide strong indications of a Fermi surface reconstruction, which is characteristic for a magnetic-filed-induced Lifshitz transition. Asymmetric hysteresis associated with FOMPT indicates complex magnetic ground state of the AFM structure. At temperatures from 28 K up to T_N the 2nd order (continuous) field-induced transition (SOMPT) with typical manifestations in magnetotransport and magnetoelastic properties have been observed. The FOMPT and SOMPT regions are separated by a tricritical point ($T_{tcp} = 28$ K, $\mu_0 H_{tcp} = 5.8$ T).

The results lead us to construction of a magnetic-phase diagram in fields parallel to the *c*-axis based on the scenario: the AFM↔PPM metamagnetic transition possess FOMPT and is separated by TCP from AFM↔PM metamagnetic transition which is SOMPT. Nevertheless, there is no PPM↔PM transition because it is one phase but with different regimes. Instead, a crossover with rather gradual change is present.

Hydrostatic pressure application gives an evidence of opposite pressure evolution of T_N (increases with increasing pressure) and H_C (decreased with increasing pressure). It leads to observed pressure induced AFM↔PM transition and FOMPT due to following TCP of T_N and H_C pressure evolution. The extrapolation of both pressure dependences predicts disappearance of H_C at 8.6 GPa where a change of the AFM- to FM-ordering is expected. The compressibility measurement clearly shows the *a* axis as the easy compression axis which is more than 3x softer than the *c* axis. Hydrostatic and uniaxial-pressure measurements indicate that the magnetic properties are driven by the magnetoelastic coupling.

The neutron diffraction experiment determined the propagation vector (0.1, 0.1, 0). Application of magnetic field causes a gradual reduction of the *h*- and *k*-components. The "antiferromagnetic" reflections disappear above the metamagnetic transition as it is expected and the increased "ferromagnetic" signal is observed with increasing magnetic field. The determination of the complete magnetic structure of $UIrSi_3$ requires further neutron diffraction experiments which are planned in near future.

The presented first complex investigation of a $UIrSi_3$ single crystal brings new knowledge about unique U compound crystalizing in a non-centrosymmetric $BaNiSn_3$-type crystal structure. The interesting physical behavior has been explained in the context of present understanding of U intermetallics.

Bibliography

[1] E. I. Rashba, Sov. Phys. Solid State 2, 1109 (1960); E. I. Rashba and V. I. Sheka, in *Landau Level Spectroscopy*, edited by G. Landwehr and E. I. Rashba (North-Holland, Amsterdam, 1991), Vol. 1, p. 131.

[2] G. Dresselhaust, *Phys. Rev.* **100**, 580-586 (1955).

[3] L. P. Gor'kov, and E. I. Rashba, *Phys. Rev. Lett.* **87**, 037004 (2001).

[4] A. Manchon, H. C. Koo, J. Nitta, S. M. Frolov, and R. A. Duine, *Nature Materials* **14**, 871–882 (2015).

[5] E. Bauer, G. Hilscher, H. Michor, Ch. Paul, E. W. Scheidt, A. Gribanov, Yu. Seropegin, H. Noël, M. Sigrist, and P. Rogl, *Phys. Rev. Lett*. **92**, 027003 (2004).

[6] Ch. Pfleiderer, *Rev. Mod. Phys.* **81**, 1551 (2009).

[7] E. Bauer and M. Sigrist, *Non-Centrosymmetric Superconductors: Introduction and Overview*, (Springer Berlin Heidelberg 2012) Lecture Notes in Physics.

[8] N. Kimura and I. Bonalde, "Chapter *Non-centrosymmetric Heavy-Fermion Superconductors*" in Non-Centrosymmetric Superconductors, Volume 847 (Springer Berlin Heidelberg 2012) pp. 35-79.

[9] N. Kimura, K. Ito, K. Saitoh, Y. Umeda, and H. Aoki, T. Terashima, *Phys. Rev. Lett.* **95**, 247004 (2005).

[10] I. Sugitani, Y. Okuda, H. Shishido, T. Yamada, A. Thamizhavel, E. Yamamoto, T. D. Matsuda, Y. Haga, T. Takeuchi, R. Settai, and Y. Onuki, *J. Phys. Soc. Jpn.* **75**, 043703 (2006).

[11] M. Klicpera, D.T. Adroja, K. Vlášková, M. Boehm, H. Mutka, B. Ouladdiaf, T. Guidi, P. Javorský, *Inorg. Chem.* **56**, 12839-12847, (2017).

[12] V. Sechovský and L. Havela, "*Chapter 1 magnetism of ternary intermetallic compounds of uranium*," in Handbook of Magnetic Materials , Vol. Volume 11 (Elsevier, 1998) pp. 1 289.

[13] D. Aoki, A. Nakamura, F. Honda, D.X. Li, Y. Homma, Y. Shimizu, Y. J. Sato, G. Knebel, J. P. Brison, A. Pourret, D. Braithwaite, G. Lapertot, Q. Niu, M. Vališka, H. Harima, and J. Flouquet, *J. Phys. Soc. Jpn.* **88**, 043702 (2019).

[14] V. Sechovský, Y. Kobayashi, H. Sato, H. Aoki, K. Prokeš, and E. Bru ck, *Physica* B 281&282 (2000) 210-212.

[15] J. Pospíšil, K. Prokeš, M. Reehuis, M. Tovar, J. P. Vejpravová, J. Prokleška, and V. Sechovský, *J. Phys. Soc. Jpn.* **80**, 084709 (2011).

[16] M. Vališka, M. Diviš, and V. Sechovský, *Phys. Rev.* B **95**, 085142 (2017).

[17] B. Buffat, B. Chevalier, B. Czeska, J. Etourneau, and P. Hagenmuller, *J. Magn. Magn. Mat.* **62**, 53-56 (1986).

[18] T. Takabatake, Y. Maeda, H. Fujii, S. Ikeda, S. Nishigori, T. Fujita, A. Minami, I. Oguro, K. Sugiyama, K. Oda, and M. Date, *Physica* B, 186-188, 734-737 (1993).

[19] S. Blundell: *Magnetism in Condensed Matter*, Oxford Masters Series in Condensed Matter Physics, Oxford University Press, Oxford 2001.

[20] Ch. Kittel, *Úvod do fyziky pevných látek*, ACADEMIA, Praha, 1985.

[21] H. H. Hill, Plutonium 1970 and Other Actinides, ed. W.N. Miner (AIME) pp. 1-19.

[22] B. Johansson and H. L. Skriver, *J. Magn. Magn. Mater*. **29**, 217 (1982).

[23] D. D. Koelling, B. D. Dunlap, and G. W. Crabtree, *Phys. Rev.* B **31**, 4966 (1985).

[24] T. Gasche, M. S. S. Brooks, and B. Johansson, *J. Phys.: Condens. Matter* **7**, 9499 (1995).

[25] M. S. S. Brooks and P. J. Kelly, *Phys. Rev. Lett.* **51**, 1708 (1983).

[26] V. Sechovsky, L. Havela, F. R. de Boer, and E. Brück, *J. Alloys Compd.* **181**, 179 (1992) 125.

[27] V. Sechovský, L. Havela, H. Nakotte, F. R. de Boer, and E. Brück, *J. Alloys Compd.* 207-208, 221 (1994).

[28] N.W. Ashcroft a D.N. Mermin, *Solid State Physics*, Thomas Learning, Toronto 1976.

[29] D. P. Landau, *Phys. Rev. Lett*. **28**, 449 (1972).

[30] R. B. Griffiths, *Phys. Rev. Lett*. **24**, 715 (1970).

[31] VG. R. Stewart, *Rev. Mod. Phys.* **56**, 755 (1984).

[32] N. H. Andersen and H. Smith, *Phys. Rev.* B **19**, 384 (1979).

[33] S. Legvold, "*Transport properties*," in Magnetic Properties of Rare Earth Metals, edited by R. J. Elliott (Springer US, Boston, MA, 1972) pp. 335_381.

[34] A. J. Dekker, *J. Appl. Phys.* **36**, 906 (1965).

[35] T. Kasuya, *Prog. Rep. Phys. (Kyoto)* **16**, 227 (1959).

[36] E. Jobiliong, J. S. Brooks, E. S. Choi, H. Lee, and Z. Fisk, *Phys. Rev*. B **72**, 104428 (2005).

[37] K. Kadowaki and S. B. Woods, *Solid State Commun.* **58**, 507 (1986).

[38] E. Hall, *Philos. Mag.* **12** (1881) 157.

[39] E.M. Pugh, *Phys. Rev.* **36**, (1930) 1503.

[40] E.M. Pugh and T. W. Lippert, *Phys. Rev*. **42** (1932) 709.

[41] C.M. Hurd, The Hall Effect in Metals and Alloys, *Plenum Press*, New York, 1972.

[42] N. Nagaosa, J. Sinova, S. Onoda, A. H. MacDonald, and N. P. Ong, *Rev. Mod. Phys.* **82**, (2010) 1539.

[43] H. Wada, K. Yoshimura, G. Kido, M. Shiga, M. Mekata, and Y. Nakamura, *Solid State Commun*. **65**, 23 (1988).

[44] Z. Arnold, *High pressure in basic and material science*, scriptum.

[45] http://kfkl.cz/techlab/cz/

[46] H.M. Rietveld, *J. Appl. Cryst*. **2**, 65 (1969).

[47] J. Rodriguez-Carvajal, FullProf User's Guide manual, CEA-CRNS, France 2000.

[48] J. Rodriguez-Carvajal, *Physica* B **192**, 55 (1992).

[49] V. Valvoda, M. Polcarová, P. Lukáč, *Základy strukturní analýzy*, Karolinum, Praha 1992.

[50] MPMS - Magnetic Property Measurement System User's Manual, Quantum Design, San Diego 2004.

[51] PPMS - Physical Property Measurement System User's Manual, Quantum Design, San Diego 2004

[52] Ladislav Skrbek a kol., *Fyzika nízkých teplot II. část*, Matfyzpress, Praha, 2011.

[53] Quantum Design, www.qdusa.com

[54] http://www.nanomagnetics.org/instrumentation and characterization/ squid magnetometers.php

[55] Quantum Design, https://www.qdusa.com/techsupport/softwareUpgrades.html

[56] PPMS - Physical Property Measurement System User's Manual, Electric Transport Option, Quantum Design, San Diego 2018.

[57] M.Rotter, H.Muller, E. Gratz, M. Doerr, and M. Loewenhaupt, Rev. Sci. Instrum. **69**, 2742 (1998).

[58] Stanford Research Systems, DSP Lock-in amplifier Model SR830, Operating Manual and Programming Reference, USA, Califormia, 2002.

[59] M. Eremets, *High pressure experimental methods*, Oxford University Press, 1996.

[60] P.W. Bridgrman, *The Physics of High Pressure*, G. Bell and Sons Ltd., London, 1949.

[61] J. Kamarád, M. Mihalik, V. Sechovský and Z. Arnold, *High Pressure Research* **28**, 4 (2008).

[62] Developed by Idemitsu Co., Ltd. Tokio, Japan; registrated as Daphne 7373.

[63] K. Murata, et al., *Rev. Sci. Instrum*. **68**, 2490 (1997).

[64] K. Yokogawa, et al., *Jpn. J. Appl. Phys*. **46**, 3636 (2007).

[65] J. Kamarád and Z. Arnold, in Proceedings of the Thirty-second Annual Meeting of the EHPRG, Brno, edited by J. Kamarád, Z. Arnold, and A. Kapička (Prometeus, Praha, 1994), p. 41.

[66] J. Kamarád, K. V. Kamenev, and Z. Arnold, High pressure science and technology – proceedings of the Joint XV AIRAPT and XXXIII EHPRG International Conference, 51-53 (1995).

[67] B. Bireckoven, J. Wittig, *J. Phys. E: Sci. Instrum.* **21**, 841 (1988).

[68] G.L. Squires, *Introduction to the Theory of Thermal Neutron Scattering*, Dover Publications, inc., Mineola, New York, (1978).

[69] I. S. Jacobs and P. E. Lawrence, *Phys. Bev*. **164** (1967) 866.

[70] Y. Haga, T. Honma, T. Yamamoto, H. Ohkuni, Y. Onuky, M. Ito, and N. Kimura, *Japanese Journal of Applied Physics* **37**, 3604 (1998).

[71] N.F. Mott, *Proc. R. Soc.* A **153**, (1936) 699.

[72] H. Jones, *Hdb. Physik* Vol. 2 XIX (Berlin: Springer Verlag 1956), p. 266.

[73] M.E. Fisher, *Philos. Mag.* 7, 1731 (1962).

[74] P.A. Fedders, and P.C. Martin, *Phys. Rev.* **143**, 245 (1966).

[75] A. J. Dirkmaat, T. Endstra, E. A. Knetsch, G. J. Nieuwenhuys, J. A. Mydosh, A. A. Menovsky, F. R. de Boer, and Z. Tarnawski, *Phys. Rev.* B **41**, 2589 (1990).

[76] L. Nordstrom, M.S.S. Brooks, and B. Johansson, *J. Phys. : Condens. Matter* **4**, 3261 (1992).

[77] K. Schwarz, P. Blaha, and G.K.H. Madsen, *Comput. Phys. Commun*. **147**, 71-76 (2002).

[78] A. R. Williams, J. Kübler, and C. D. Gelatt, *Phys. Rev.* B **19**, 6094 (1979)

[79] L. M. Sandratskii, *Adv. Phys*. **47**, 91 (1998).

[80] H. Amitsuka, T. Sakakibara, K Sugiyama, T. Ikeba, Y. Miyako, M. Date, and A. Yamagishi, *Physica* B **177**, 173-176 (1992).

[81] Y. Mnyukh, *Am. J. Condens. Matter Phys*. **3**, 142 (2013).

[82] W. C. Nunes, W. S. D. Folly, J. P. Sinnecker, and M. A. Novak, *Phys. Rev.* B **70**, 014419 (2004).

[83] I. M. Lifshitz, *Zh. Eksp. Teor. Fiz.* **38**, 1569 (1960) [*Sov. Phys.* JETP 11, 1130 (1960)].

[84] J. Pospíšil, Y. Haga, Y. Kohama, A. Miyake, S. Kambe, N. Tateiwa, M. Vališka, P. Proschek, J. Prokleška, V. Sechovský, M. Tokunaga, K. Kindo, A. Matsuo, and E. Yamamoto, *Phys. Rev.* B **98**, 014430 (2018).

[85] S. Yoshii, A. V. Andreev, E. Brück, J. C. P. Klaasse, K. Prokeš, F. R. de Boer, M. Hagiwara, K. Kindo, and V. Sechovský, *J. Phys.: Conf. Ser.* **51**, 151 (2006).

[86] E. Brück, H. Nakotte, F. R. de Boer, P. F. de Châtel, H. P. VanderMeulen, J. J. M. Franse, A. A. Menovsky, N. H. Kim-Ngan, L. Havela, V. Sechovsky, J. A. A. J. Perenboom, N. C. Tuan, and J. Sebek, *Phys. Rev.* B **49**, 8852 (1994).

[87] K. Shrestha, D. Antonio, M. Jaime, N. Harrison, D. S. Mast, D. Safarik, T. Durakiewicz, J.-C. Griveau, and K. Gofryk, *Scientific Reports* 7, 6642 (2017).

[88] R. L. Stillwell, I.-L. Liu, N. Harrison, M. Jaime, J. R. Jeffries, and N. P. Butch, *Phys. Rev.* B **95**, 014414 (2017).

[89] E. Stryjewski and N. Giordano, *Adv. Phys*. **26** (1977) 487.

[90] D. S. Grachtrup, M. Bleckmann, B. Willenberg, S. Süllow, M. Bartkowiak, Y. Skourski, H. Rakoto, I. Sheikin, and J. A. Mydosh, *Phys. Rev*. B **85** (2012) 054410.

[91] D. S. Grachtrup, N. Steinki, S. Sullow, Z. Cakir, G. Zwicknagl, Y. Krupko, I. Sheikin, M. Jaime, and J. A. Mydosh, *Phys. Rev.* B **95** (2017) 134422.

[92] A. Gorgout, Thesis, Communauté d'universités et d'établissements Université Grenoble Alpes, 2017 (https://tel.archives-ouvertes.fr/tel-01563381/document).

[93] R. D. Barnard, *Thermoelectricity in Metals and Alloys* (Taylor, London, 1972).

[94] N. Johannsen, S. Süllow, A. V. Sologubenko, T. Lorenz, and J. A. Mydosh, *Phys. Rev.* B **78**, 121103(R) (2008).

[95] D. R. Noakes and G. M. Kalvius, *Physica* B 289–290, 248 (2000).

[96] B. Janoušová, V. Sechovský, K. Prokeš, and T. Komatsubara, *Physica* B **328**, 145 (2003).

[97] J. Prokleška, B. Detlefs, V. Sechovský, and M. Míšek, *J. Magn. Magn. Mater*. **322**, 1120 (2010).

[98] T. Khmelevska, P. Svoboda, B. Janoušová, V. Sechovský, S. Chang, H. Nakotte, M. S. Torikachvili, *J. Appl. Phys*. **89**, 11 (2001).

[99] D. Staško and J. Prchal, to bee published.

[100] L. Fuentes-Montero, P. Čermak, J. Rodríguez-Carvajal, and A. Filhol, The *Esmeralda suite for Laue diffraction data treatment* (2015) DOI: 10.13140/RG.2.1.4954.1202

[101] S. G. Brush, *Phys. Rev. Mod*. **39**, 4 (1967).

List of Tables

List of Abbreviations

AFM	Antiferromagnetic
AHE	Anomalous Hall effect
ASW	Augmented spherical waves
BAC	Bridgman-anvil type pressure cells
BCC	Body centered cubic crystal structure
CCR	Closed Cycle Refrigerator
CEF	Crystal electric field
CPC	Clamp pressure cell
CYCLOPS	Cylindrical ccd Laue Octagonal Photo Scintillator
DCMP	Department of Condensed Matter Physics
DFT	Density functional theory
EDX	Energy Dispersive X-ray analysis
E_F	Energy on Fermi level
FC	Field-cooled
FCC	Face centered cubic crystal structure
FLPO	Full potential local orbitals
FM	Ferromagnetic
FOMPT	First-order magnetic phase transition
FS	Fermi sueface
ILL	Institute of Laue-Langevin
MPMS	Magnetic Property Measurement System
LSDA	Local spin density approximation
MAE	Magnetocrystalline anisotropy energy
MCW	Modified Curie-Weiss law
MLY	Heinz Maier-Leibnitz Zentrum
MT	Metamagnetic transition
PM	Paramagnetic
PPM	Polarize paramagnetic
PPMS	Physical Property Measurement System
RRR	Resistivity Residual Ration
SEM	Scanning electron microscope
SOMPT	Second-order magnetic phase transition
SQUID	Superconducting Quantum Interference Device
SOC	Spin orbit coupling
TCP	Tricritical point
XRPD	X-ray powder diffraction
ZFC	Zero-field-cooled

List of Publications

1 F. Honda, J. Valenta, J. Prokleška, J. Pospíšil, P. Proschek, J. Prchal, and V. Sechovský, Magnetotransport as a probe of phase transformations in metallic antiferromagnets: The case of $UIrSi_3$, *Physical Review* B **100**, 014401, (2019)

2 J. Valenta, F. Honda, M. Vališka, P. Opletal, J. Kaštil, M. Míšek, M. Diviš, L. Sandratskii, J. Prchal, and V. Sechovský, Antiferromagnetism and phase transitions in non-centrosymmetric $UIrSi_3$, *Physical Review* B **97**, 144423, (2018)

3 M. Vališka, H. Saito, T. Yanagisawa, C. Tabata, H. Amitsuka, K. Uhlířová, J. Prokleška, P. Proschek, J. Valenta, M. Míšek, D. I. Gorbunov, J. Wosnitza, and V. Sechovský, Magnetoelastic phenomena in antiferromagnetic uranium intermetallics: The UAu_2Si_2 case, *Physical Review* B **98**, 174439 (2018)

4 P. Opletal, J. Prokleška, J. Valenta and V. Sechovský, Electrical resistivity across the tricriticality in itinerant ferromagnet, *AIP Advances* **8**, 055710 (2018)

5 F. Honda, K. Okauchi, Y. Sato, A. Nakamura, H. Akamine, Y. Ashitomi, M. Hedo, T. Nakama, Y. Onuki, T. Takeuchi, J. Valenta, J. Prchal, V. Sechovský, D. Aoki. Pressure-induced valence change and moderate heavy fermion state in Eu-compounds, *Physica B: Condensed Matter* **536**, 182-191, (2018)

6 P. Opletal, J. Prokleška, J. Valenta, P. Proschek, V. Tkáč, R. Tarasenko, M. Běhounková, Š. Matoušková, M. M. Abd-Elmeguid and V. Sechovský, Quantum ferromagnet in the proximity of the tricritical point, *npj Quantum Materials*, **2**, 29 (2017)

7 J. Kaštil, M Míšek, J. Kamarád, Z. Arnold, K. Vlášková, J. Prchal, M. Diviš, P. Doležal, J. Prokleška, J. Valenta, J. Fikáček, A. Rudajevová, D. Kriegner, Properties of the divalent-Yb compound $YbAu_2Si_2$ under extreme conditions, *Physica B* **505**, 41-44 (2017)

8 R. Tarasenko, V. Tkáč, A. Orendáčová, M. Orendáč, J. Valenta, V. Sechovský, A. Feher. Experimental study of magnetocaloric effect in the two-level quantum system $KTm(MoO_4)_2$**,** *Physica B: Condensed Matter* **536,** 450-453 (2017)

9 J. Šebesta, J. Prchal, J. Valenta, M. Kratochvílová and V. Sechovský, Magnetism in $TmCo_2$, *Acta Physica Polonica A* **127**, 379-381 (2015)

10 J. Valenta, J. Prchal, R. Khasanov, M. Kratochvílová, M. Míšek, M. Vališka, V. Sechovský, Presence of parimagnetism in $HoCo_2$ under hydrostatic pressure, *Journal of Physics: Conference Series* **500**, 182041 (2014)

11 J. Valenta, J. Prchal, M. Kratochvílová, M. Míšek, V. Sechovský, Presence of parimagnetism in $Ho(Co_{1-x}Si_x)_2$ under hydrostatic pressure, *Acta Physica Polonica A* **126**, 406-408 (2014)

12 J. Prchal, J. Šebesta, J. Valenta, M. Míšek, D. Turčinková, L. Lapčák., J. Prokleška, M. Kratochvílová and V. Sechovský, Magnetism in RCo_2 (R = Dy, Ho, Er, Tm) under hydrostatic pressure, *Acta Physica Polonica A* **126**, 288-289 (2014)

13 L. Havela, J. Prchal, J. Valenta, M. Dopita, M. Diviš, I. Turek, L. Kyvala, D. Legut. Pressure variations of the 5f magnetism in UH_3, *Journal of Magnetism and Magnetic Materials*, accepted

14 M. Kratochvílová, D. Král, M. Dušek, J. Valenta, R. Colman, O. Heczko, M. Veis. Fe_2MnSn - a new magnetic Heusler compound**,** *Journal of Alloys and Compounds*, submitted